論文 / 著書情報
Article / Book Information

題目(和文)	
Title(English)	Development of a site-selective photooxidation method to target genome DNA by biphenyl photosensitizer-PNA conjugates
著者(和文)	DUYaoyao
Author(English)	Yaoyao Du
出典(和文)	学位:博士(理学), 学位授与機関:東京科学大学, 報告番号:甲第243号, 授与年月日:2025年3月26日, 学位の種別:課程博士, 審査員:湯浅 英哉,川井 清彦,清尾 康志,中村 浩之,大窪 章寛
Citation(English)	Degree:Doctor (Science), Conferring organization: Institute of Science Tokyo, Report number:甲第243号, Conferred date:2025/3/26, Degree Type:Course doctor, Examiner:,,,,
学位種別(和文)	博士論文
Type(English)	Doctoral Thesis

Doctoral Dissertation

Development of a site-selective photooxidation method to target genome DNA by biphenyl photosensitizer-PNA conjugates

Academic Supervisor: Prof. Hideya YUASA

Department of Life Science and Technology

Institute of Science Tokyo

(formerly Tokyo Institute of Technology)

Yaoyao DU

January 2025

TABLE OF CONTENTS

List of Abbreviation

$^1O_2$	Singlet oxygen
$^3O_2$	Triplet state molecular oxygen
8-oxoG	8-oxo-7,8-dihydroguanine
B	Nucleobase
Cas9	CRISPR-associated protein 9
CRISPR	Clustered regularly interspaced short palindromic repeats
DSBs	Double-strand breaks
dG	2'-deoxyguanosine
dSp	Spiroiminohydantoin
FA	Furfuryl alcohol
Fpg	Formamidopyrimidine DNA N-glycosylase
IP	Ionization potential
ISC	Intersystem crossing
NA	Nucleic acid
NBP	Nitrobiphenyl photosensitizer
NBP-T-PNA	Nitrobiphenyl photosensitizer-thymine-PNA
ONs	Oligonucleotides
PAGE	Polyacrylamide gel electrophoresis
PICT	Planar intramolecular charge-transfer
PNA	Peptide nucleic acid
PS	Photosensitizer
ROS	Reactive oxygen species
RP-HPLC	Reverse-phase high-performance liquid chromatography
S_1	Singlet state
SOCT	Spin-orbit charge transfer
SPPS	Solid phase peptide synthesis
SSBs	Single-strand breaks
T_1	Triplet excited state
TICT	twisted intramolecular charge-transfer

Chapter 1: Introduction and Background

1.1 ABSTRACT

Gene manipulation has garnered substantial attention due to its potential applications in diverse fields, including biotechnology and biomedical research.[1] To this end, various nuclease-based DNA cleavage technologies, especially CRISPR/Cas9, have been extensively studied to create double-strand breaks (DSBs) in target DNA regions, facilitating precise genetic modifications at pre-designed loci.[2,3] However, CRISPR-Cas9 systems have inherent drawbacks. The large Cas9 protein, crucial to these systems, faces challenges related to efficient delivery and has the risk of eliciting immune responses.[2] Therefore, the development of alternative techniques to achieve precise DNA strand cleavage has become critically important.

In addition to DSBs, single-strand breaks (SSBs) represent another common form of DNA damage, often arising during the repair of oxidized nucleobases, with guanine (G) being particularly susceptible to oxidation.[4,5] Photo-knockout techniques, which leverage the exceptional spatiotemporal resolution of light, have demonstrated the ability to enhance specificity in genome manipulation.[6,7]

To address the immune problem triggered by nuclease Cas9, the aim of this study is to develop an alternative small-molecule photo-knockout approach to produce targeted genome-DNA cleavage via site-selective photooxidation of G. A novel conjugate combining a nitrobiphenyl photosensitizer (NBP) with peptide nucleic acids (PNA) has been designed and analyzed, aiming to explore its potential applications within this impactful research field. **Fig. 1.1** depicts the chemical structure of NBP modified PNA designed in this thesis. NBP, a type II photosensitizer developed by our lab, can produce $^1O_2$ with high quantum efficiency.[8] Prior research has shown that NBP conjugated to dsDNA with a short ethylene linker induces distance-dependent photooxidation of G. Oxidation efficiency varies with the distance between G and NBP, peaking at intervals of 8-10 base pairs in line with the 10.5 base pairs per turn of the B-type DNA duplexes.[9]

Building on the previous studies, this thesis explores the potential of NBP-PNA conjugates for dsDNA invasion and photo-knockout. Being unique to NBP-DNA, the PNA backbone used in this thesis is endowed with strong invasion ability to the DNA double helix,[10,11] which is a useful tool for sequence-specific recognition of DNA. In addition, the relative short diffusion range of $^1O_2$, approximately 125 nm in water at room temperature[12] [13] further ensure localized oxidative damage. **Fig. 1.2** depicts the proposed site-selective photooxidation of NBP-PNA. Then such oxidative damage would result in nicks on one DNA strand during repair processes in cells. This tool, therefore, offers simplicity, programmability in design, and high spatiotemporal specificity.

To begin with, this chapter is the introduction and background of this thesis. The second section briefly summarizes the literature, including nuclease-based DNA cleavage technologies, SSBs in DNA through oxidative damage, development of selective photooxidation methods by oligonucleotides-photosensitizer. The third

section describes the design of this thesis work.

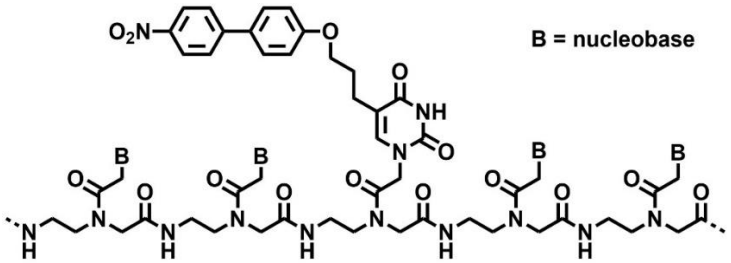

Fig. 1.1 NBP modified PNA designed in this thesis.

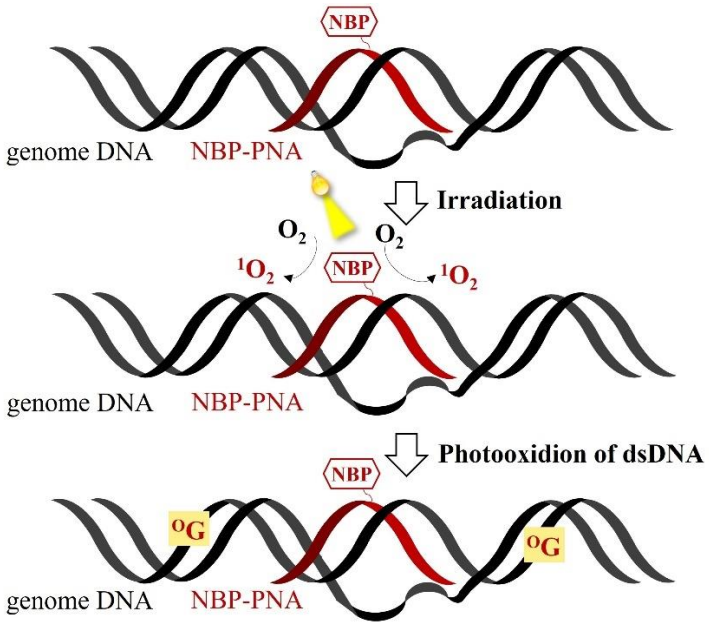

Fig. 1.2 Proposed site-selective photooxidation of NBP-PNA.

1.2 BACKGROUND

1.2.1 DNA Cleavage Techniques for Gene Manipulation

1.2.1.1 Mechanism of gene manipulation and nuclease-based technologies

Nuclease-based DNA cleavage technologies play an important role in gene manipulation, because they make it possible to introduce targeted changes into the DNA sequence at pre-designed genomic loci. **Fig. 1.3** illustrates the basic working principle of currently popular gene manipulation technologies: firstly, a nuclease creates break in the target DNA region and subsequently the repair system is activated to fix that dagame, leading to a required change at this precise site.[2,3] Therefore, accurately produced breaks in the target DNA sequence, namely sequence-specific cleavage, is a critical step for manipulating the genes.

So far, four out of the best known sequence-specific cleavage techniques are meganuclease, zinc finger nuclease (ZFNs), transcription activator-like effector nucleases (TALEN), and clustered regularly interspaced short palindromic repeats (CRISPR) / CRISPR-associated protein 9 (Cas9) (CRISPR-Cas9), which are capable of introducing double-strand breaks (DSBs) at specific genomic loci.[3] These nuclease systems can be broadly categorized into two groups based on their DNA recognition mechanisms. Meganucleases, ZFNs, and TALENs bind to specific DNA sequences through protein-DNA interactions. Meganucleases are endonucleases that target large recognition sites, whereas ZFNs and TALENs are chimeric enzymes combining a DNA binding domain with a sequence-independent FokI nuclease.[14] Consequently, the requirement of protein engineering or molecular cloning for re-targeting limits their application, due to the very difficult, time-consuming, and expensive operations.[15] In contrast, CRISPR-Cas9 system utilizes guide RNA that binds to the target DNA through base-pairing, directing the Cas endonuclease to perform the cleavage. As only the guide RNA needs to be customized, it is more flexible and less labor-intensive, with lower treatment costs and enhanced manipulation capabilities. These benefits have attracted much attention, leading to the extensive study and development for precise, customizable genome manipulation.[16]

In cells, the DSBs in DNA are repaired through either the non-homologous end joining (NHEJ) pathway or the homology-directed repair (HDR) pathway, generating different outcome of the DNA manipulation. NHEJ typically leads to small insertions or deletions near the break, whereas HDR, relying on a repair template, can introduce precise edits that restore the DNA sequence at the break.[17,18]

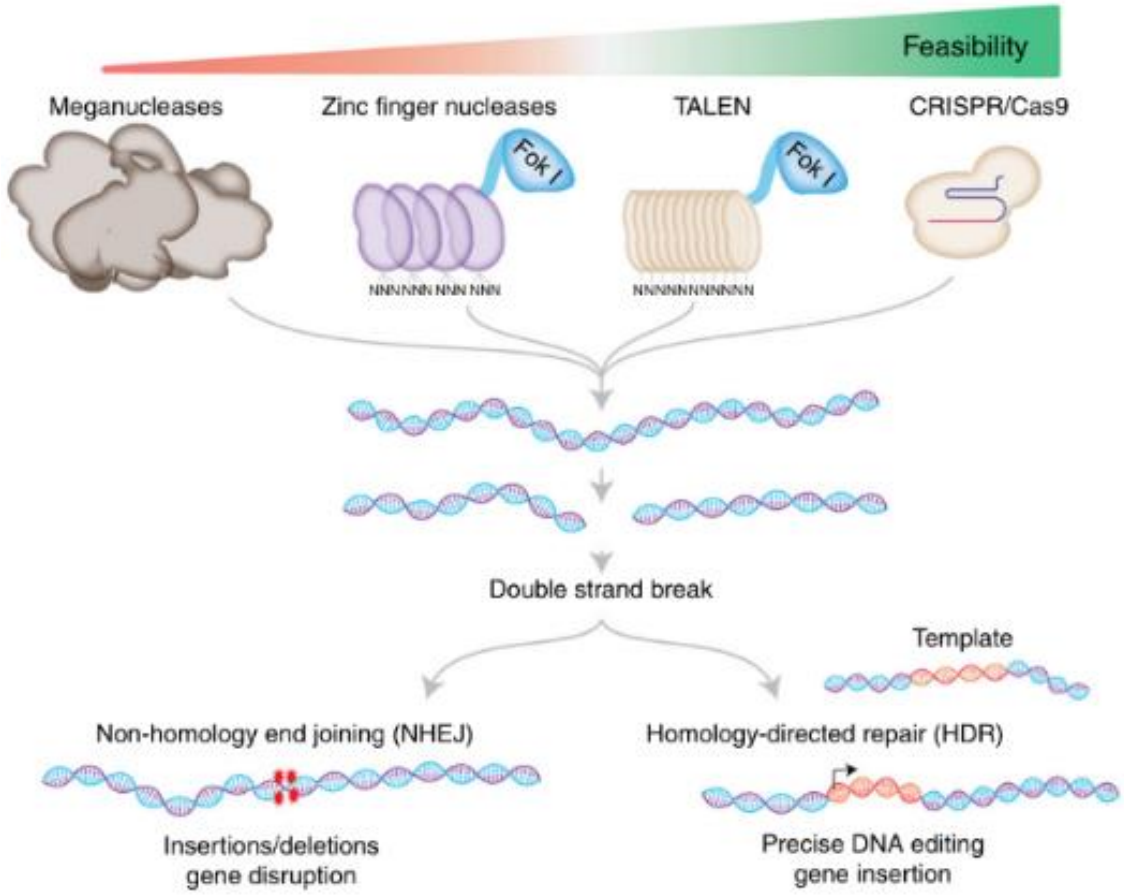

Fig. 1.3 The basic working principle of major genome-manipulation technologies.[14] Adapted with permission from ref 14. Copyright 2018 Springer Nature.

1.2.1.2 CRISPR/Cas9 technique

CRISPR/Cas9 technique is originally derived from the prokaryotic immune system and consists of two key components: a single guide RNA (sgRNA) that directs the system to the target DNA and Cas9 protein, which performs the DNA double-strand cleavage. As illustrated in **Fig. 1.4**, Cas9 protein contains two nuclease domains in charge of the cleavage of each DNA strand: HNH domain cleaves the gRNA-binding strand and RuvC domain cleaves the non-complementary DNA strand. sgRNA is also composed of two main parts: CRISPR RNA (crRNA), which contains a 20-nucleotide protospacer sequence that is complementary to the target DNA, and trans-activating CRISPR RNA (tracrRNA), which binds to Cas9 protein to form Cas9/sgRNA complex. Upon unwinding and binding to one of the DNA strands, Cas9-sgRNA complex cleaves both strands approximately three nucleotides upstream of the protospacer-adjacent motif (PAM) sequence.[17]

However, the lack of spatiotemporal specificity during genome-manipulation process has severely limited the application of CRISPR/Cas9 in more complicated and varied contexts. Thus, a precise regulation of DNA cleavage over various dimensions,

such as time, space, and dose, is highly desirable.[6]

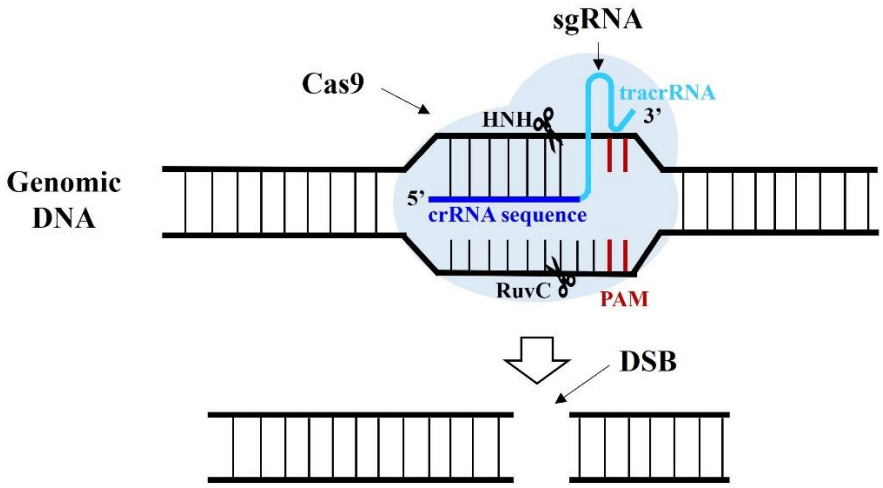

Fig. 1.4 The schematic diagram of the CRISPR-Cas9 system molecular mechanism.[17]

1.2.2 Photo-Knockout by CRISPR-Cas9

Benefiting from its exceptional spatiotemporal resolution, light has been utilized as a very powerful tool in numerous studies for the precise control of some biological processes.[7] Therefore, to enhance the accuracy of genomic manipulation, accumulating efforts have been dedicated to exploring the optical regulation of CRISPR-Cas9. And this so called photo-knockout techniques have proven to greatly impart spatiotemporal specificity and control of genome manipulation.[6]

One of the effective methods is to control the generation of DSB by directly harnessing nuclease activity over light. One typical case is shown in **Fig. 1.5**, two fragments of Cas9 were each fused to photoinducible dimerization domains called positive magnet (pMag) and negative magnet (nMag), respectively, which are separated from each other in dark leading to the inactivation of Cas. Upon blue-light irradiation, these two fragments undergo a dimerization reaction, bringing the Cas9 fragments together, thus reassembling the enzyme and restoring its nuclease activity.[19]

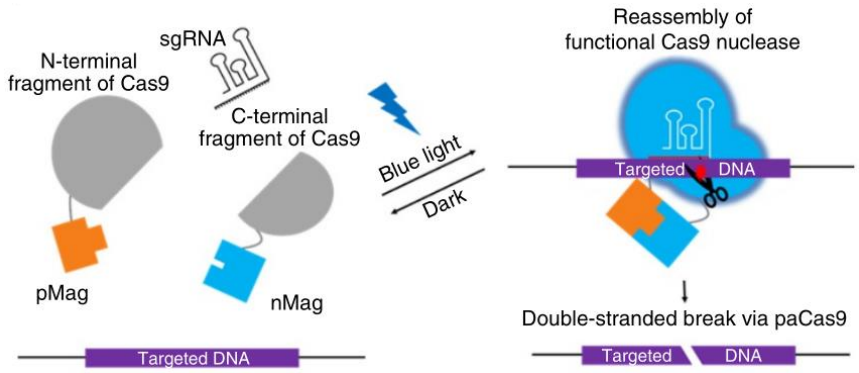

Fig. 1.5 Photoactivatable Cas9.[19]
Adapted with permission from ref 19. Copyright 2015, Springer Nature.

Alternatively, modifying the guide RNA (gRNA) offers another strategy for optically regulating CRISPR-Cas9 function. Such studies include a caged gRNA, which was created by incorporating caged uridine and guanosine nucleotides into the gRNA sequence, resulting in complete inhibition of the hybridization between gRNA and the target DNA (**Fig. 1.6**). Once irradiated by a specific light, the native gRNA can rapidly be released through the photolysis and then bind to a target DNA region, activating the CRISPR-Cas9 function.[20]

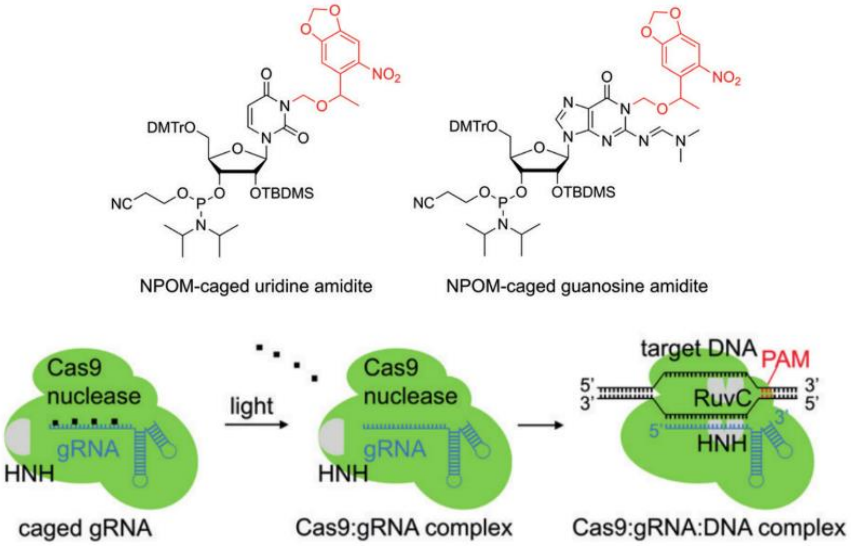

Fig. 1.6 Photoactivatable gRNA.[20]
Adapted with permission from ref 20. Copyright 2020, John Wiley and Sons.

Even though CRISPR-Cas9 and its variants have shown advantages over other DNA cleavage techniques, they also present certain drawbacks and raise increasing concerns. Notably, the pivotal large Cas9 protein in these systems faces challenges related to efficient delivery and may provoke unwanted immune responses.[2]

1.2.3 Single-Strand Breaks (SSBs) in DNA Through Oxidative Damage

1.2.3.1 Formation of SSBs in base excision repair (BER)

Apart from DSBs, the discontinuities occurring in only one strand of the DNA double helix, namely single-strand breaks (SSBs), are another prevalent type of DNA lesions in organisms. Such lesions can arise through the breakdown of oxidized sugars in the backbone or indirectly during the repair of oxidized nucleobases. [21] Particularly, nucleobases are susceptible to oxidation and are attracting widespread interests in studies of ageing, cancer and neurodegeneration.[22],[23] One of the most common sources of oxidative attack is reactive oxygen species (ROS), which originate from both internal metabolic processes and external sources and continuously induce oxidative damage to DNA in living systems.[24,25,26] In the meantime, the oxidative nucleobase lesions are subjected to multiple repair processes that can create a SSB accompanied by loss of a single or several nucleotides.[4,5]

Generally, oxidative damage to DNA bases caused by ROS can lead to the formation of both non-bulky lesions, such as 8-oxo-7,8-dihydroguanine (8-oxoG), a common purine oxidation product, and bulky, helix-distorting lesions, such as cyclopurines and DNA-protein cross-links.[27],[28] These lesions are repaired by two principal DNA excision repair pathways that are relatively independent processes involving different enzymes. The first pathway is base excision repair (BER), which removes individual modified bases using glycosylases and apurinic endonuclease 1 (APE1). The second, more intricate pathway, is nucleotide excision repair (NER), which excises a short oligonucleotide containing the damaged site (**Fig. 1.7**).[4,27]

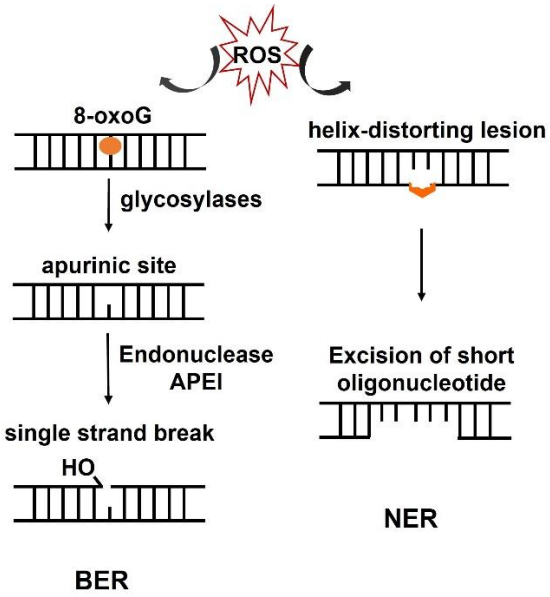

Fig. 1.7 DNA excision repair mechanisms for bulky or non-bulky DNA lesion caused by ROS.[27]

The photo-knockdown method used in this thesis is expected to generate oxidative damages on only Gs. Since such single damages might be more likely processed by BER pathway, the chemistry of SSBs formed in BER should be considered here as depicted in **Fig. 1.8**. To begin with, DNA glycosylases identify and remove the damaged base. Following this, the apurinic/apyrimidinic (AP) site left behind is cleaved at the 5' position by APE1, producing a nick with a 3' hydroxyl group and a 5' sugar phosphate.[29] Likewise, the AP site can also be cleaved by DNA AP lyase via β-elimination reaction, leaving a 3′-α, β-unsaturated aldehyde and a 5'-phosphate.[30,31] In addition, it has been discovered that there are some bi-functional glycosylases in mammalian cells, such as OGG1, NTHL1, and NEIL1,which possess dual activity: they excise the damaged base and cleave the DNA backbone at the 3' side of the AP site.[22]

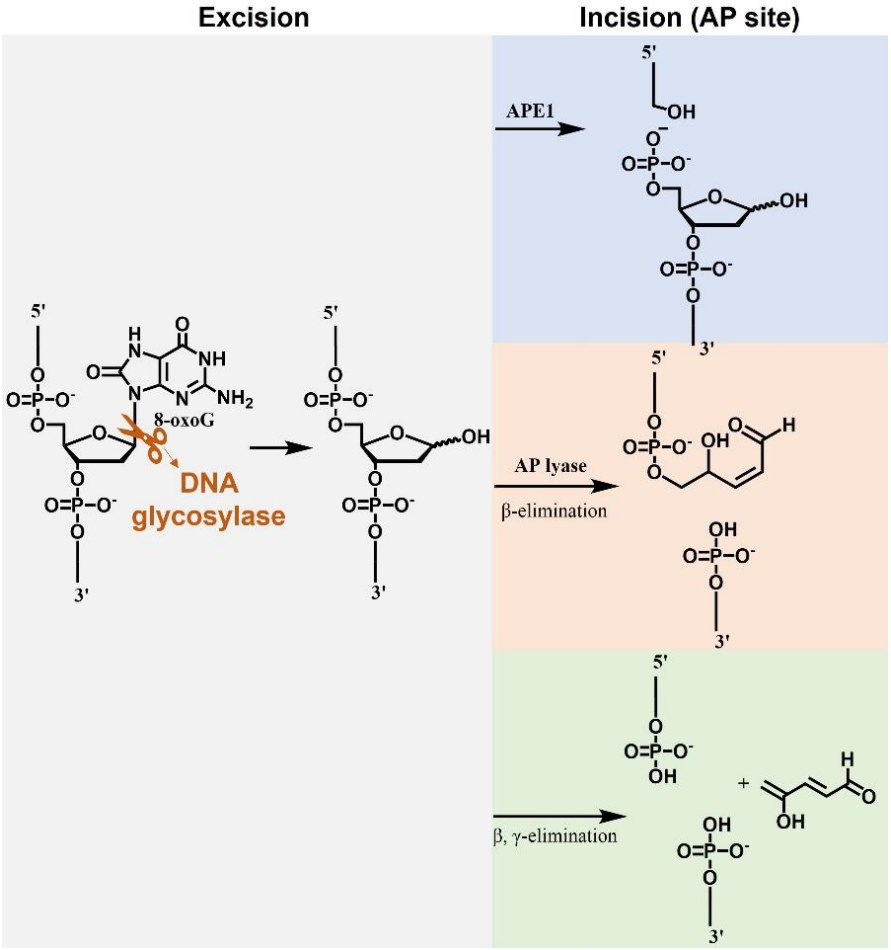

Fig. 1.8 SSBs formation in base excision repair (BER).[32]

Once the damaged base is removed and the abasic site is incised, the DNA strand would be restored through synthesis, during which some flanking sequences can be replaced.[33]

1.2.3.2 Photooxidation reactions of G

Oxidative damage of DNA mediated by oxidants, such as ROS[34] and carbonate radical anion ($CO_3^{\cdot-}$)[35] , is non-random, and Guanine (G) represents a dominant target for oxidation among all native nucleobases due to its high electron density.[36] So far, many studies have reported the calculated as well as experimental ionization potential (IP) of four DNA base monomers and neighbor stacked nucleobases as summarized in **Table 1.1**.[34,37,38] Apparently, G has the lowest IP (7.75 eV) compared to other bases. What's more, two effects can further lower the IP of G: the π stacking with other nucleotides as shown in Table 1, and the formation of base pair, as the computed IP of the pair G:C is 6.92 eV in gas phase.[39]

Table 1.1. Ionization Potential of Nucleobase Monomers and Stacked Nucleobases in a B-form geometry (N-Methylated) (eV). [a] [34] Adapted with permission from ref 34. Copyright 1996, American Chemical Society.

	3'-base			
5'-base	G	A	C	T
	7.75	8.24	8.87	9.14
G	7.28	7.51	7.68	7.69
A	7.51	7.97	8.20	8.19
C	7.24	7.75	8.36	8.69
T	7.67	8.15	8.79	8.97

[a] Ionization potentials were estimated by Koopmans's theorem. The values are the HOMO energies of 6-31G* single-point calculations.

Oxidative damage to G often leads to the formation of a variety of products, including 7,8-dihydro-8-oxoguanine (8-oxoG), spiroiminohydantoin (Sp) and 5-guanidinohydantoin (Gh).[40] These oxidative products arise through various mechanisms, such as photosensitization which is a simple and manageable method for producing singlet oxygen ($^1O_2$).[41]

Photosensitized oxidation reactions are categorized as either type I or type II processes. The identification and mechanistic aspects of photooxidation reactions have been extensively studied during the past decades.[24,42,43] In summary, as depicted in **Fig. 1.9**, a photon absorbed by a photosensitizer (PS) in its ground state is excited to a short-lived (typically nanoseconds) singlet state (S_1), which is rapidly transformed into a more stable, longer lifetime (typically microseconds) triplet excited state (T_1) via intersystem crossing (ISC), though ISC is a forbidden transition. T_1 can initiate two distinct oxidative pathways: type I and type II reactions.[24]

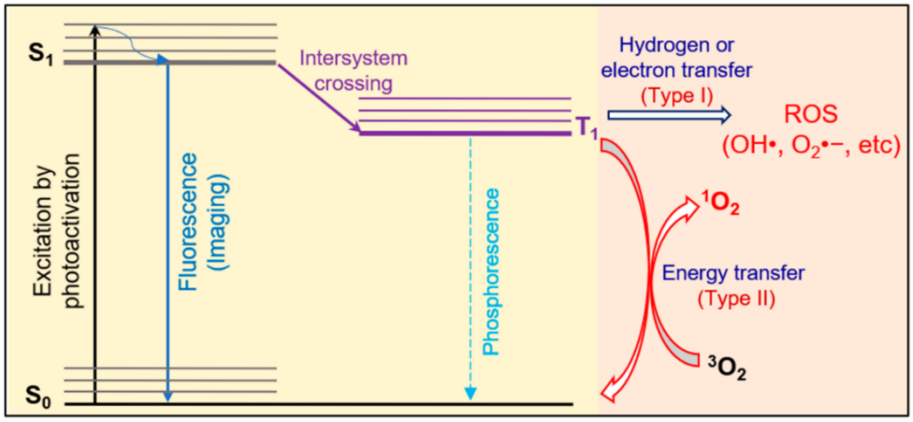

Fig. 1.9 Scheme of the type I and type II photosensitized oxidations.[44] Adapted with permission from ref 44. Copyright 2021, American Chemical Society.

Type I PSs undergo photoinduced electron transfer and generate neutral radicals or radical ions.[45] Additionally, they can interact with O_2 through electron donation or charge transfer to produce ROS such as superoxide anions ($O_2^{\bullet-}$) and hydroxyl radicals ($HO^{\bullet}$).[42] The primary oxidation products of G by highly reactive $HO^{\bullet}$ or one-electron

transfer are outlined in **Scheme 1.1**. Especially, the intermediate, 8-hydroxy-7,8-dihydro-guanyl radical (8-HO-G•), which has reducing properties, is rapidly oxidized by molecular oxygen or weak oxidants to form the 8-oxoG lesion.[46]

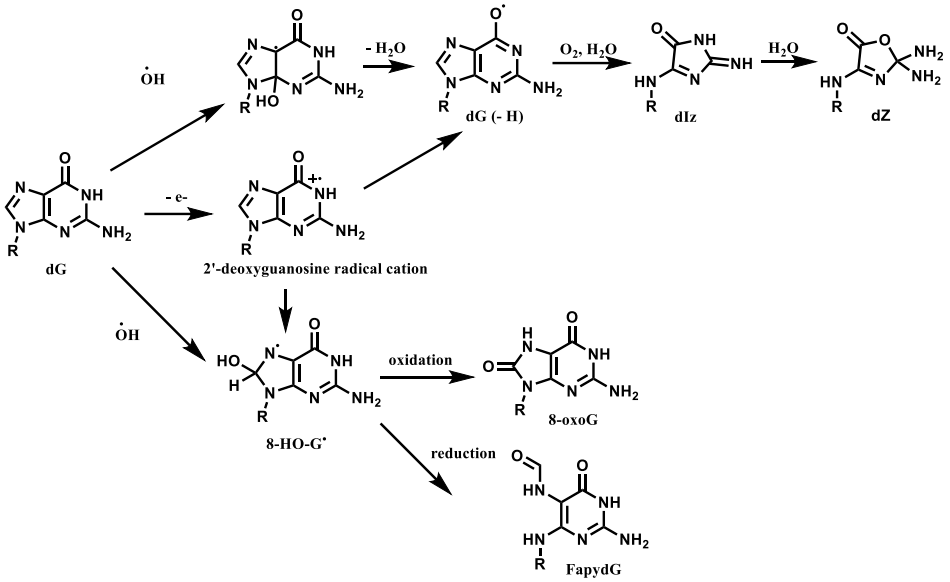

Scheme 1.1 Single oxidized lesions arising from the reaction of G with HO• radical and one-electron oxidants[47]

Adapted with permission from ref 47. Copyright 2003, Elsevier.

Type II is framed as the sensitized formation of singlet oxygen ($^1O_2$). In this pathway, the triplet-state PS transfers excitation energy to triplet state molecular oxygen ($^3O_2$) with subsequent generation of $^1O_2$. It is well documented that $^1O_2$ exclusively adds to G in DNA[48], giving rise to several products including **8-oxoG**, **Gh**, **Sp**, and **dOxa** as shown in **Scheme 1.2** and **1.3**.[49,50] The interaction between $^1O_2$ and G typically begins with a [4 + 2] cycloaddition forming an endoperoxide within the imidazole ring (**Scheme 1.2**). This intermediate rearranges into an 8-hydroperoxy derivative (**1-1**), which is subsequently reduced to an 8-hydroxylated residue, a tautomer of **8-oxoG**. This pathway dominates in the formation of **8-oxoG** through $^1O_2$ in double-strand DNA.[50] Alternatively, in the absence of a reducing agent, **1-1** can yield an oxidized intermediate **1-2** prone to nucleophilic attack, most commonly by water, forming a new transient intermediate **1-3** which serves as a precursor for **Sp** and **Gh**. Their relative formation is influenced by pH: at acidic pH (around 4), **Gh** is favored, whereas **Sp** prevails at neutral pH (around 7).[51] In dsDNA, the rearrangement of intermediate **1-3** into **Sp** is less favorable. Conversely, secondary oxidation of **8-oxoG** by $^1O_2$ results in **dGh** through a [2 + 2] cycloaddition pathway, forming intermediate **1-4**, as illustrated in **Scheme 1.3**. Additionally, **dOxa** is observed in the oxidation of 8-oxoG-containing oligonucleotide.[24,52,53]

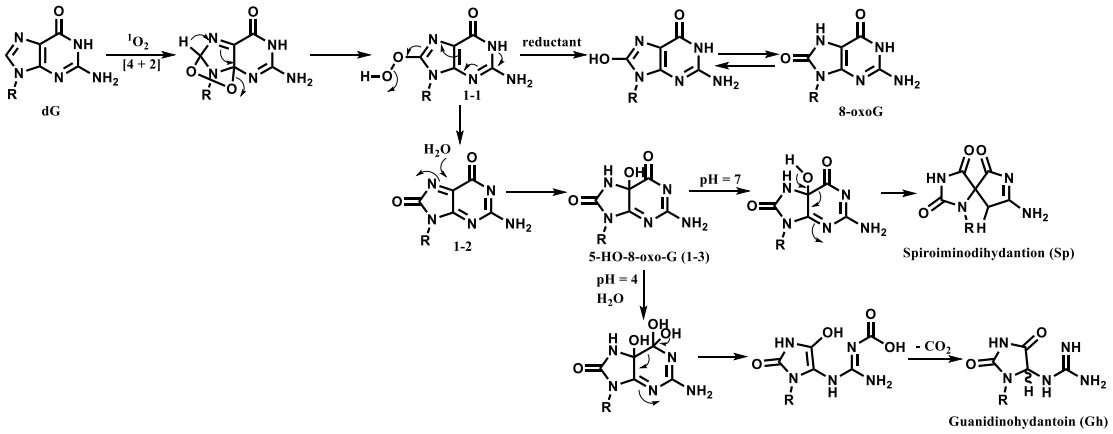

Scheme 1.2 $^1O_2$ oxidation products of the free 2'-deoxyguanosine.[49,50]

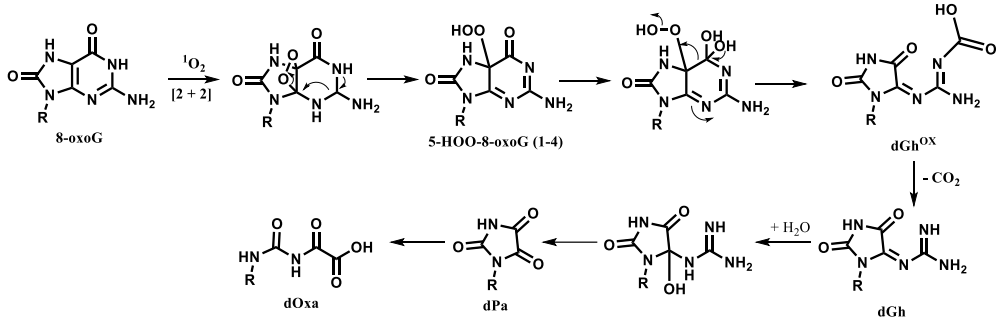

Scheme 1.3. Secondary $^1O_2$ oxidation products of 8-oxoG-containing oligonucleotide.[49,50]

1.2.4 Development of Selective Photooxidation Methods by Oligonucleotides-PS

A comprehensive understanding of how DNA oxidation contributes to the onset and progression of related diseases requires in-depth knowledge of the chemistry behind DNA oxidation, as well as the mechanisms governing repair selectivity and efficiency in cells.[36] To achieve this, various techniques have been employed to induce oxidative damage to DNA within living cells. For example, treating cells with potassium bromate ($KBrO_3$) results in the widespread formation of 8-oxoG lesions.[54] Furthermore, photooxidation using a sensitizer, such as TRF1-FAP system (telomere shelterin protein telomeric repeat-binding factor 1-fluorogen activating peptide), has proven effective for controlling the timing and localization of G oxidation in telomeres.[55] However, a significant challenge remains: achieving precise localization of photooxidative damage within a predetermined genomic region.

1.2.4.1 Selective photooxidation methods by PNA conjugates

An attractive approach for a site-selective photooxidation of DNA is to connect the PS moieties to oligonucleotides. Such conjugates enable targeted DNA damage within a defined area and time frame.[56,57,58] Oligonucleotides can bind to single- and double-strand nucleic acid targets by forming Watson-Crick base-paired duplexes and Hoogsteen base-paired triplexes, respectively. As illustrated in **Fig. 1.10**, in terms of

Watson-Crick base pairs, Adenine (A) connects with Thymine (T) through two hydrogen bonds, whereas G forms three hydrogen bonds with Cytosine (C). Besides DNA duplex assembles via such hydrogen bonds, an extra strand can further bind to it by other types of hydrogen bonding. In Hoogsteen pairing, an additional T binds via hydrogen bonds on the major groove of A in a Watson-Crick A-T base pair arrangement, while a protonated C binds through hydrogen bonds on the major groove of G in a Watson-Crick C-G base pair arrangement.[59] Accumulating studies have shown that the sequence-specific selectivity is feasible through these kinds of base pairing.[60,61,62] For example, research by Boutorine et al. showed the conjugates of 14-mer oligonucleotides with chlorin-type PSs could induce damage selectively in both single-stranded and double-stranded DNA.[60]

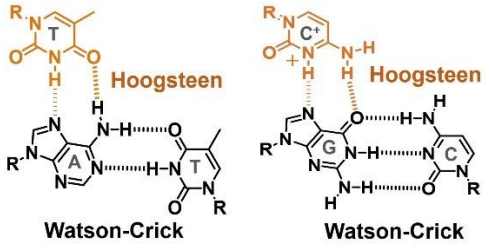

Fig. 1.10 Watson-Crick hydrogen bonds and Hoogsteen hydrogen bonds.[63]
Adapted with permission from ref 63. Copyright 2020, Elsevier.

To address the inherent instability and other limitations of native nucleic acids, several types of artificial oligonuclotides have been developed.[64] Among these, peptide nucleic acids (PNAs) are especially promising due to their exceptional ability to invade dsDNA in a sequence-specific manner.[10,11] PNAs are neutral nucleic acid analogs in which the sugar-phosphate backbone of DNA is replaced by a polyamide structure based on N-aminoethylglycine. (**Fig. 1.11**) Their unique properties, including high affinity and specificity for complementary DNA sequences, low toxicity, and resistance to enzymatic degradation by nucleases and proteases, make them ideal candidates for gene manipulation applications.[11,65] In pursuing this endeavor, some exquisite PNA designs/structures have been developed over two decades to improve its invasion efficiency and solubility. As shown in **Fig. 1.12**, PNA can directly interact with dsDNA through Watson-Crick base pairing, Hoogsteen base pairing, or a combination of both mechanisms.[66,67,63]

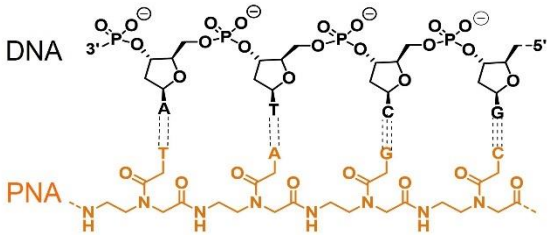

Fig. 1.11 The negative DNA backbone and neutral PNA backbone.[63]
Adapted with permission from ref 63. Copyright 2020, Elsevier.

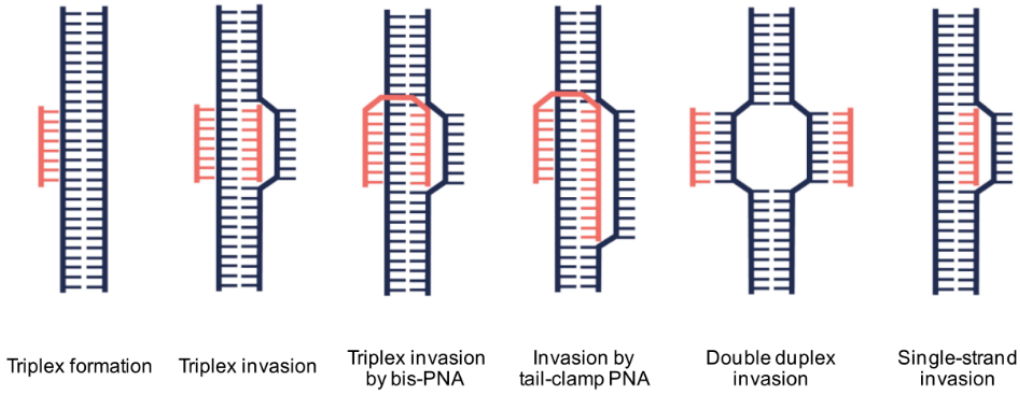

Fig. 1.12 Different modes of targeting DNA duplexes by PNA.[63]
Adapted with permission from ref 63. Copyright 2020, Elsevier.

To date, several studies have explored the use of PNA conjugates as site-specific photooxidation inducers. For instance, a conjugate of thiazole orange with PNA, connected through an extended polyethylene glycol linker, was demonstrated to invade plasmid DNA at specific sites, forming a double-duplex structure and causing photodamage.[68] Similarly, a rose bengal-PNA conjugate caused photodamage to single-strand DNA.[69] Nevertheless, in another interesting study, Saito et al. have highlighted an inhibitory effect of PNA on G photooxidation mediated by adjacent DNA-cyanobenzophenone conjugate.[70] Thus, there are still notable gaps in the literature, especially the regioselectivity of G photooxidation is ambiguous and need to be well investigated.

1.2.4.2 Distance-dependent photooxidation of G in dsDNA by nitrobiphenyl photosensitizer (NBP)

The nitrobiphenyl photosensitizer (NBP) is a type II photosensitizer that generates $^1O_2$ with a high quantum yield of 0.88 via a twist-assisted spin-orbit charge transfer (SOCT) intersystem crossing (ISC) mechanism. As illustrated in **Fig. 1.13**, NBP features a strong electron-withdrawing nitro group (-NO_2) on one phenyl (Ph) ring, and an electron-donating methoxy group (-OMe) on the opposite Ph ring. The ground state NBP with the Ph-NO_2 dihedral angle at 37° (S0 (37°)) absorbs a photon and yields an excited state ^{1}CT (37°) (with the Ph-NO_2 dihedral angle still at 37°), which is so-called planar intramolecular charge-transfer state (PICT). Subsequently, the ^{1}CT (37°) is transferred into a more stable twisted intramolecular charge-transfer (TICT) state, namely ^{1}CT (⊥). Following this, ^{1}CT (⊥) is readily converted to T_1 via spin-orbit charge transfer (SOCT). Then the T_1 state quickly undergoes further twisting to T_1 (//), which can react with ground-state oxygen ($^3O_2$) to produce singlet oxygen ($^1O_2$).[8]

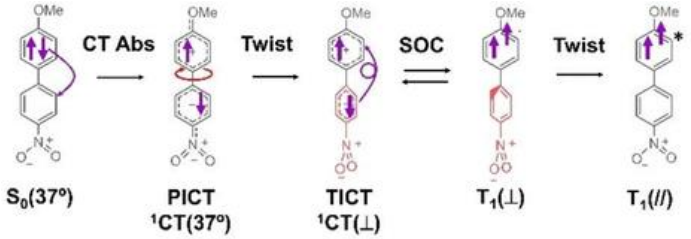

Fig. 1.13 The twist-assisted spin-orbit charge transfer intersystem crossing mechanism of NBP[8]
Adapted with permission from ref 8. Copyright 2019, John Wiley and Sons.

Notably, NBP is significantly smaller in size compared to earlier photosensitizers, such as porphyrins.[8] This compact size allows NBP to pass through channel proteins in the cell membrane, such as GLUT1, and to fit within the major groove of the DNA double helix. Thus, NBP offers a unique approach to study the regioselectivity of DNA oxidation by $^1O_2$, owing to its small size and photo-activation capabilities. Previous research conducted in our laboratory provided valuable insights into the distance-dependent photooxidation of G in dsDNA using a conjugated NBP. As depicted in **Fig. 1.14**, NBP was covalently attached to a DNA oligonucleotide, inducing the oxidation of G in the complementary strand upon irradiation. The efficiency of G oxidation as a function of the distance between G and NBP exhibited distinct patterns, with peaks occurring at 8-10 base pair intervals, which is consistent with the 10.5 base pairs per helical turn of B-form DNA.[9] However, the above NBP-DNA is inherently unsuitable for the direct photo-knockout of dsDNA.

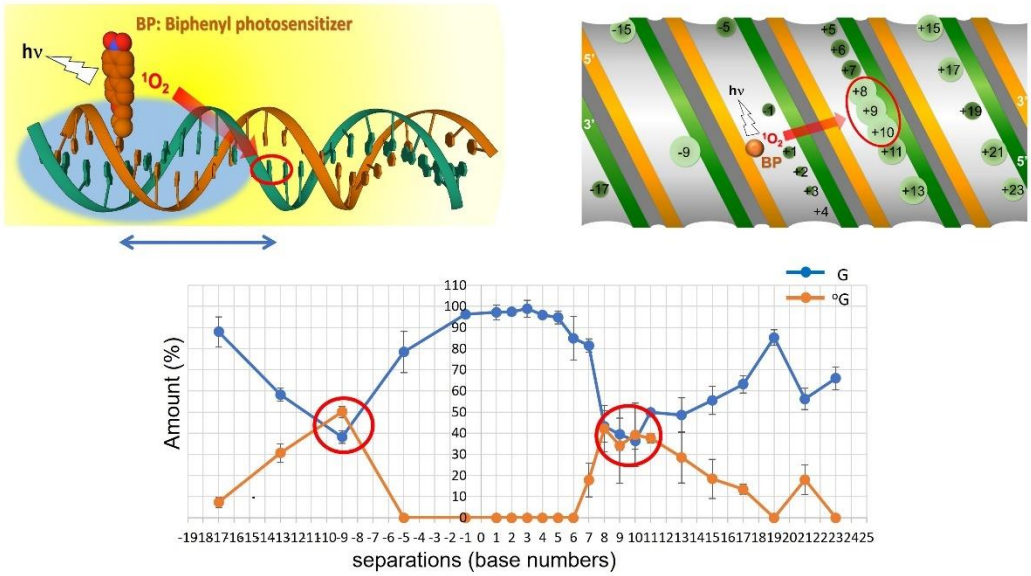

Fig. 1.14 Distance-dependent photooxidation of G by NBP-DNA conjugates.[9]
Adapted with permission from ref 9. Copyright 2023, Springer Nature.

1.3 DESIGN OF THE THESIS WORK

The aim of this study is to develop an alternative photo-knockout approach to overcome the limitations of CRISPR-Cas9, namely the unnecessary immune responses due to the large nuclease protein. To address this problem, a small-molecule method is proposed to act as genetic scissors by conjugating the small-sized nitrobiphenyl photosensitizer (NBP) with peptide nucleic acids (PNAs) through a short ethylene linker.

PNAs with a pseudo-peptide backbone have excellent binding affinity with DNA and are capable of invading into DNA double helix. It is hypothesized that once bound to the target DNA sequence and irradiated, the singlet oxygen generated from NBP could attack G to introduce oxidative damage in relatively small and specific areas. Such oxidative damage of G would lead to the formation of nick in one strand of the DNA double helix during the DNA repair processes in cells. This tool offers simplicity, programmability in design, and high spatiotemporal specificity. Hence, we decided to explore the possibility of dsDNA photo-knockout by NBP-PNA conjugates.

This doctoral thesis comprises five chapters.

In Chapter 1, the general introduction of this thesis is presented, and the background information is reviewed. The first section is the abstract of the whole thesis. The second section summarizes the related literature, including: 1. major DNA cleavage techniques used for gene manipulation, especially the CRISPR-Cas9 system and recently proposed photo-knockout techniques, 2. formation of single-strand breaks (SSBs) in DNA through oxidative damage mechanism, 3. examples of selective photooxidation of DNA by oligonucleotides-photosensetizer conjugates. The third section describes the design of this thesis work.

In Chapter 2, the synthesis of NBP-PNA conjugates and their binding affinities are demonstrated. The first introduction section briefly summarizes the findings about NBP-DNA photoxidation and explains the design of NBP-PNA conjugate. The second section shows the synthesis routine of NBP-thymine-PNA monomer consisting of 8 steps, including the electrophilic substitution of *tert*-butylbromoacetate, Sonogashira coupling, hydrogenation with Pd/C, Mitsunobu coupling, and amidation of carboxylic acid. The third section depicts the optimization of the solid-phase synthesis and HPLC purification of PNA oligomers. Then the fourth section shows the characterization of the binding affinities of NBP-PNAs to target ssDNA, including melting temperature (T_m) and CD spectra. The fifth section summarizes this chapter.

In Chapter 3, the photooxidation properties of NBP-PNA conjugate to ssDNA and dsDNA with a sticky end is investigated. Section 1 is the introduction of this chapter, describing several examples of oligonucleotide conjugates for induing oxidative damage to DNA and the oxidation chemistry of G by $^1O_2$. In section 2, the $^1O_2$ production ability of NBP-PNA is confirmed by monitoring $^1O_2$ probe furfuryl alcohol via HPLC. In section 3, the photooxidation efficiency of NBP-PNA conjugate hybridizing with ssDNA is investigated by HPLC quantitatively, and compared with

NBP-DNA and external xylitol-NBP. In section 4, the photooxidation of NBP-PNA binding to the sticky end of a dsDNA is investigated via gel electrophoresis experiments. The DNA strand break occurs at oxidative damage site with two cleavage treatment methods, allowing to assess regioselectivity of NBP-PNA to dsDNA. Section 5 is the summary of this chapter.

In Chapter 4, the invasion of NBP-PNA to dsDNA termini and the photooxidation of PNA/dsDNA invasion complex. Section 1 is the introduction of this chapter, describing some studies about the modification of PNA for improving invasion efficiency. Section 2 investigates the invasion of NBP-PNA conjugate to dsDNA by non-denaturing gel, two DNA models are used, one containing mixed-AT sequence, and the other is mixed-ATCG sequence. Section 3 tested the photooxidation of dsDNA in PNA invasion solution. And the PNA's self-aggregation is discussed. Section 4 demonstrates the presence of PNA self-assembly tends to affect DNA oxidation by $^1O_2$.

Finally, Chapter 5 summaries of this thesis work and discusses the further development of NBP-PNA conjugates.

Chapter 2: Synthesis and Characterization of NBP-PNA Oligomers

2.1 INTRODUCTION

In this chapter, the design and synthesis of a novel nitrobiphenyl photosensitizer-thymine-PNA (NBP-T-PNA) monomer (**Fig. 2.1**) and the oligomerization of its PNA conjugates are described. Additionally, the hybridization duplexes of NBP-PNAs with their complementary DNA are characterized by their melting behavior, as monitored by UV spectroscopy, and their CD spectra.

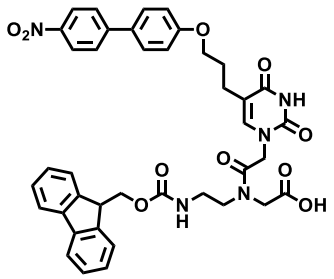

Fig. 2.1 Structure of NBP-T-PNA monomer.

As detailed in Chapter 1, the NBP developed in our lab is a small-size type II photosensitizer capable of generating $^1O_2$,[8] which selectively oxidizes guanine (G) in dsDNA.[24] The short lifetime of $^1O_2$ limits its active distance to about 100 nm in H_2O at room temperature.[12, 13] Thus, by anchoring the small-volume NBP at a specific site using a short linker, oxidative damage to DNA can be localized. What's more, our previous research has extensively studied the relationship between G oxidation and distance from the tethered NBP in double-stranded DNA (dsDNA). Given the optimal distance for photooxidation between NBP and G in dsDNA is 8-10 base pairs,[16] in this study, NBP is positioned 9 nucleobases from the target G. And PNA oligomers consisting of 15 bases with a hydrophilic lysine attached at the N-terminus are planned to be synthesized using reported Fmoc-based solid-phase synthesis.[71,72,73]

This chapter is organized as follows: Section 1 is the introduction of this chapter. Section 2 outlines the 8-step synthesis routine of the NBP-T-PNA monomer. Section 3 is the optimization of solid-phase peptide synthesis and the purification of 15-mer PNA oligomers. Section 4 discusses the characterization of the binding of NBP-PNAs to target single-stranded DNA (ssDNA), including T_m and CD spectra. Finally, Section 5 summarizes this chapter.

2.2 SYNTHESIS OF NBP-T-PNA MONOMER

The design of synthesis routine of NBP-thymine-PNA (NBP-T-PNA) monomer as outlined in **Scheme 2.1** is adapted from that of NBP-DNA conjugate. NBP is engineered to link with PNA using a short ethylene linker attached at the α-methyl position of thymine. Starting with the electrophilic substitution of 5-iodouracil (**2-1)** by *tert*-butyl bromoacetate to introduce the linker between nucleobase and PNA backbone. Secondly, the -NH group in pyrimidine ring is protected by *tert*-butyloxycarbonyl (Boc). Thirdly, a short alkyl linker replaces the iodo group in compound **2-3** via Sonogashira[74] coupling, and the subsequent reduction of the alkynyl group yields compound **5**. In the fourth step, the two protecting groups—Boc group and *tert*-butyl (*t*-Bu) group —are removed together by TFA. Next, the NBP group is attached to the nucleobase using Mitsunobu coupling,[75] resulting in compound **2-6**. Finally, the NBP-T-PNA monomer is synthesized by coupling NBP-T (**2-7**) with the fluorenylmethyloxycarbonyl (Fmoc)-protected PNA backbone followed by deprotection to expose carboxylic acid group.[76]

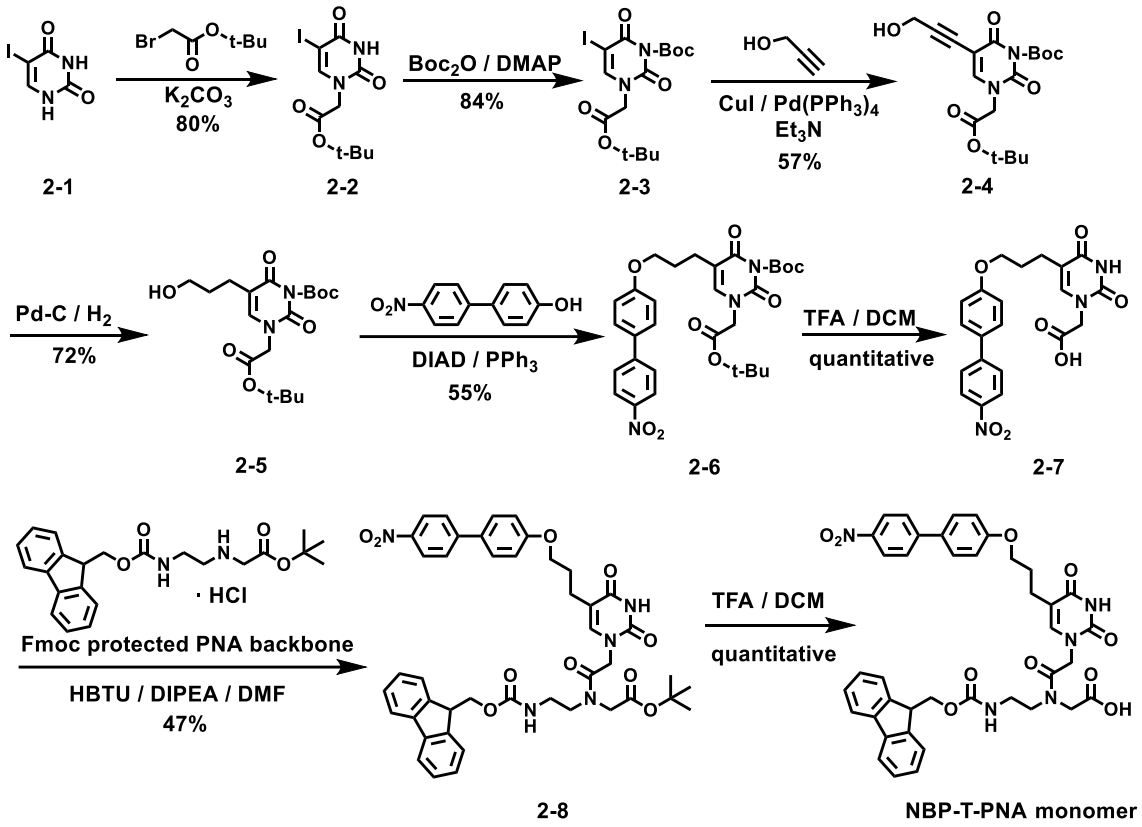

Scheme 2.1 Synthesis of the NBP-T- PNA monomer.[76]

In addition, the Fmoc-protected PNA backbone is synthesized according to reported literature protocols. (**Scheme 2.2**)[77]

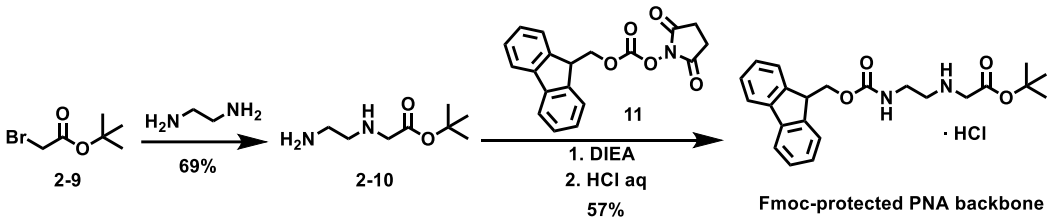

Scheme 2.2 Synthesis of the Fmoc protected PNA backbone.

What's more, the synthesis of the **abasic PNA monomer** is achieved through the acetylation of the PNA backbone using hexafluorophosphate benzotriazole tetramethyl uronium (HBTU) as an activator as illustrated in **Scheme 2.3**. This modification is expected to create a gap in the strand, resulting in increased space around target G.

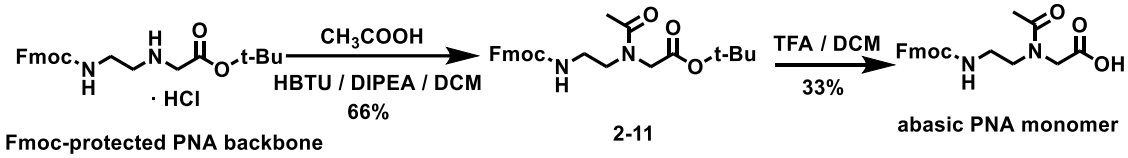

Scheme 2.3 Synthesis of the Fmoc protected PNA backbone.

Besides the above **NBP-T-PNA monomer**, the NBP group was designed to be covalently linked to T through a triazole ring via click chemistry (**Fig. 2.2**).[78] As shown in **Scheme 2.4**, the synthesis began with diazo transfer reaction of 5-amines-uracil derivatives (**2-12**) to introduce an azide group to nucleobase **2-13**. Then the substitution reaction introduced the linker connecting PNA and nucleobase. Next, the NBP portion was introduced by alkyne-azide cycloaddition reaction, also known as click chemistry that generally has high yield. Subsequent reactions were supposed to be hydrolysis and incorporation with PNA backbone. However, the NBP-triazole-T building blocks **2-17** and **2-18** were not stable under either acidic or basic conditions (**Scheme 2.5**). Due to this base/acid instability and extremely low water solubility of the intermediates (**2-17** and **2-18**), we ultimately selected the NBP-T-PNA monomer (**Fig. 2.1**) described above for subsequent studies, despite the high yield of click chemistry.

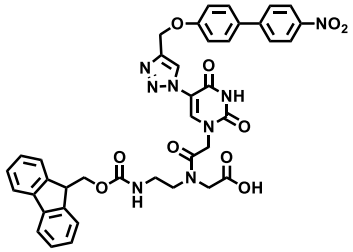

Fig. 2.2 The designed NBP-triazole-T monomer.

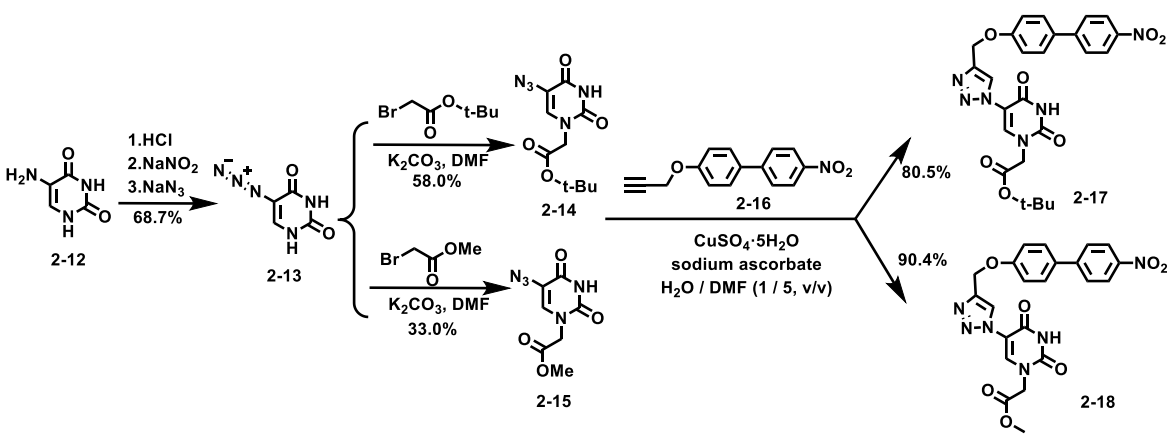

Scheme 2.4 The synthesis of NBP-triazole-T building blocks.

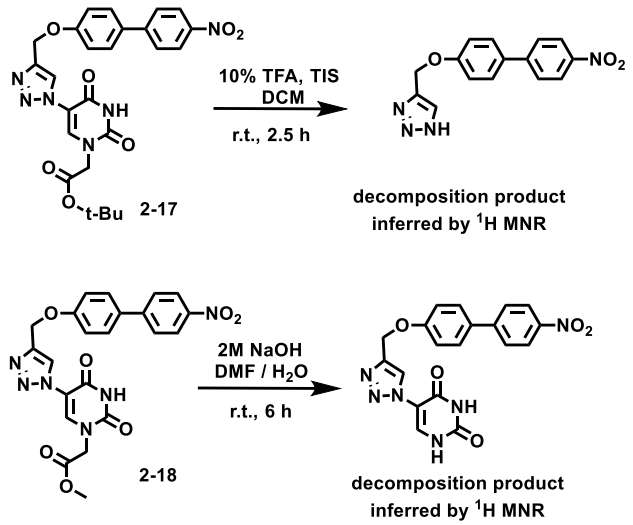

Scheme 2.5 The decomposition of **2-17** and **2-18** in acidic and basic condition respectively.

2.3 SOLID-PHASE-SYNTHESISS OF PNA OLIGOMER

PNA oligomer synthesis occurs by coupling the carboxyl group of the incoming amino acid to the N-terminus of the growing PNA chain. Oligomerization of PNA originates from the solid-phase peptide synthesis (SPPS) of polypeptides which employs a selective protecting group strategy on either the primary amine or carboxylic acid groups. Typically, there are two methods for selective protecting strategies in SPPS: the Boc protecting strategy, which uses monomers with Boc-protected backbone-NH_2 and benzyloxycarbonyl (Cbz)-protected or benzyl (Bn)-protected nucleobases; and the Fmoc protecting strategy, which employs an orthogonal protecting method which uses PNA monomers prepared with the terminal amine protected by the Fmoc group and nucleobases protected by the acid-labile Boc or benzhydryloxycarbonyl (Bhoc) groups.[79,80,81] The Fmoc strategy is favored over Boc because it features a milder deprotection step that avoids the dangers of hydrofluoric acid (HF) and has proven to be more efficient.[82] Nowadays, many types of Fmoc/Bhoc monomers are commercially available.

The SPPS cycle for PNA oligomerization using the Fmoc protecting strategy is illustrated in **Scheme 2.6**.[71] Initially, the first PNA monomer at C terminus is covalently bound to a solid polymeric support and synthesized step-by-step in a single reaction vessel. Next is capping of unreacted amine by acetic anhydride, leading to better separation of target sequence and impurity sequence. Then, in the deprotection step the N-terminal Fmoc is removed by the secondary amine of piperidine. Subsequently, another new circle begins with coupling step. Finally, after several circles the synthesized sequence can be cut from solid support by trifluoromethanesulphonic acid (TFA), and the temporary protecting group Bhoc of nucleobase is removed concomitantly.

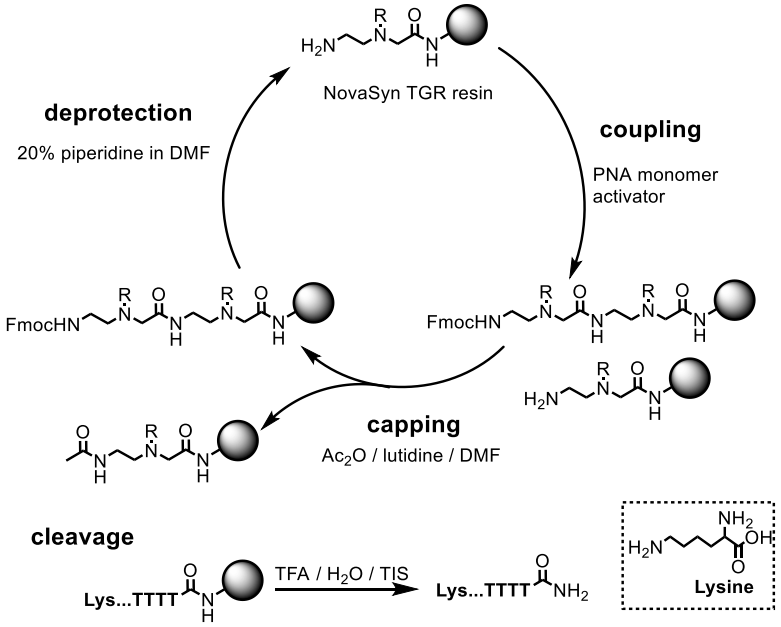

Scheme 2.6 Workflow of solid-phase peptide synthesis (SPPS).

2.3.1 Optimization of Coupling Conditions

Despite following the published standard protocol,[83,84] the yield of the 15mer PNA was less than 5%, resulting in very poor-quality raw products. To develop an efficient synthetic protocol for our target 15mer NBP-PNAs, the coupling reaction conditions were optimized based on published procedures.[71, 72, 73]

The construction of PNA oligomers is greatly affected by the excess of reagents, the duration of reactions, the sequence and length of the oligomers, and the temperature at which the reactions are carried out.[85,9] In particular, the growth of the purine-rich sequences is seriously hindered by the stacking of the Fmoc group with the nucleobases and the aggregation of PNA chains on resin.[86] According to release of Fmoc, it was found that coupling yield of Fmoc-A(Bhoc)-OH monomer with resin-TTPT-NH_2 was only 61% under the standard condition (No.1 reaction in **Table 2.1**). Thus the on-resin coupling efficiency of Fmoc-A(Bhoc)-OH monomer with resin-TTPT-NH_2 (**Scheme 2.7**) were investigated under different reaction conditions by monitoring Fmoc deprotection with UV spectrometer. PyBOP is chosen as the coupling reagents because it can provide high coupling efficiency and is economic.[87]

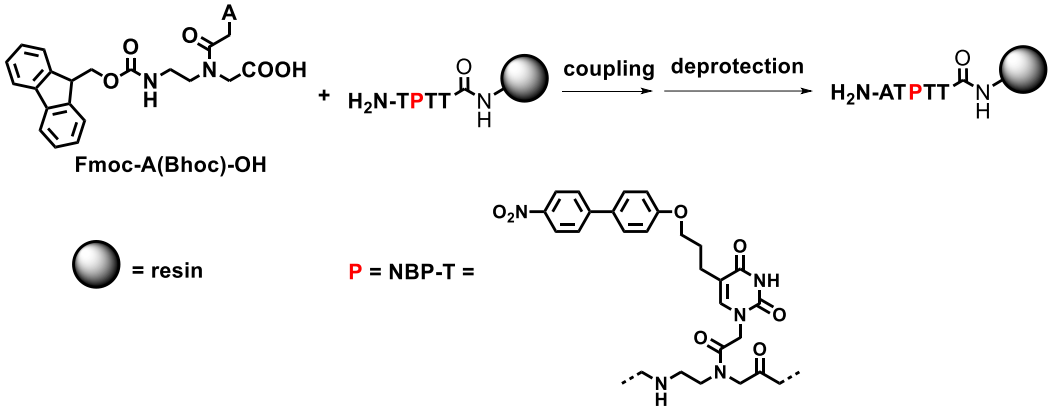

Scheme 2.7 On-resin coupling of Fmoc-A(Bhoc)-OH monomer with resin-TTPT-NH_2.

In **Table 2.1**, the first condition (No.1) is the standard situation. Compared to No.1, extended pre-swell time (No.2) did not increase coupling yield. 40 °C is the most proper reaction temperature. Further, anhydrous NMP is found to be a better solvent. Therefore, the optimal coupling condition was confirmed to be 4 molar equivalents of the PNA monomer (relative to resin loading), 4 molar equivalents of PyBOP, and 8 molar equivalents of NMM in anhydrous NMP, at 40 °C for 1 hour. For Fmoc-A(Bhoc)-OH, both the concentration of all reactants and the duration of reaction were doubled. As a result, the total yields of 15-mer PNA oligomers could reach 25%. It is crucial to emphasize that reagents used for PNA oligomerization must be kept as anhydrous as possible, as any contamination with water can lead to incomplete monomer coupling during synthesis.[71] In spite of the establishment of an optimal protocol, maintaining vigilant oversight throughout the synthesis steps is paramount. Careful observation using the Kaiser test and Fmoc monitoring ensures that each cycle reacts completely.

Table 2.1 Screening of coupling conditions of H_2N-ATPTT-resin (**P** = NBP-T).

No.	Solvent	Pre-swell time (h)	Temperature (°C)	Yield (%)
1	DMF	1	15	61
2	DMF	12	15	52
3	DMF	1	40	82
4	DMF	1	70	85
5	anhydrous DMF	1	15	65
6	anhydrous NMP	1	15	83
7	anhydrous NMP	1	40	94

What's more, two NBP-DNA conjugates studied in this thesis were prepared according to the published procedures,[16] and the sequecnce is shown in **Table 2.3**.

2.3.2 Purification and Confirmation of NBP-PNA Oligomers

The crude PNA oligomer products cleaved from the resin were precipitated with cold diethyl ether at 0 °C and purified by RP-HPLC according to published methods. [71] HPLC chromatograms of crude products at 30 °C are shown on the following figures (**Fig. 2.3**–**Fig.2.8**). In addition, heating is very helpful to reduce aggregation and sharpen peaks.

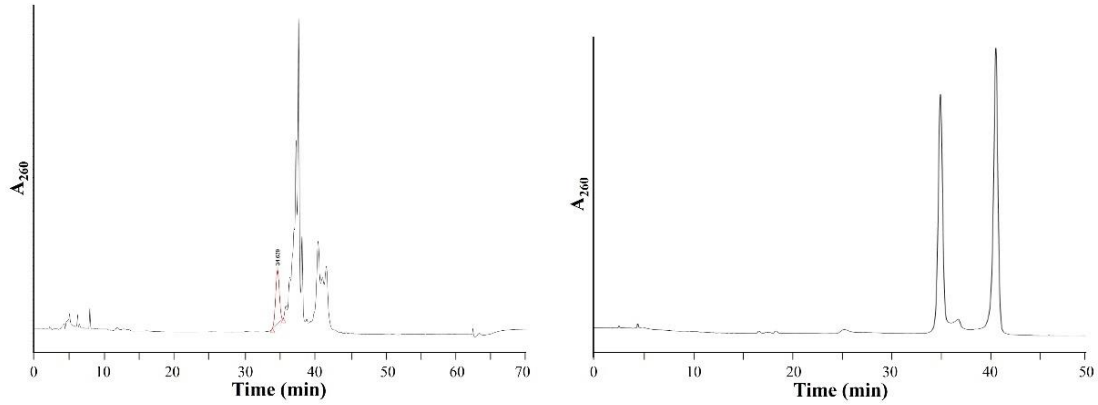

Fig. 2.3 HPLC chromatogram of crude (left, the red peak is target oligomer) and purified (right) products of **PNA01**.

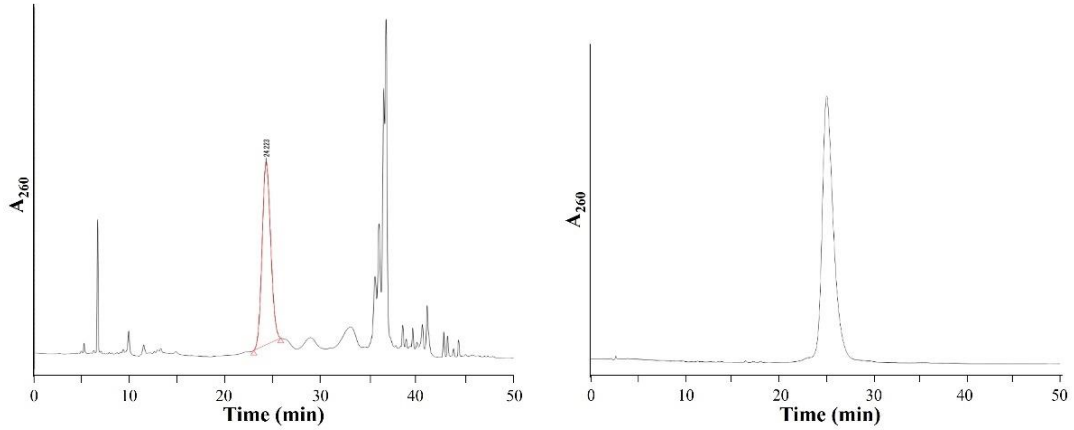

Fig. 2.4 HPLC chromatogram of crude (left, the red peak is target oligomer) and

purified (right) products of **PNA02**.

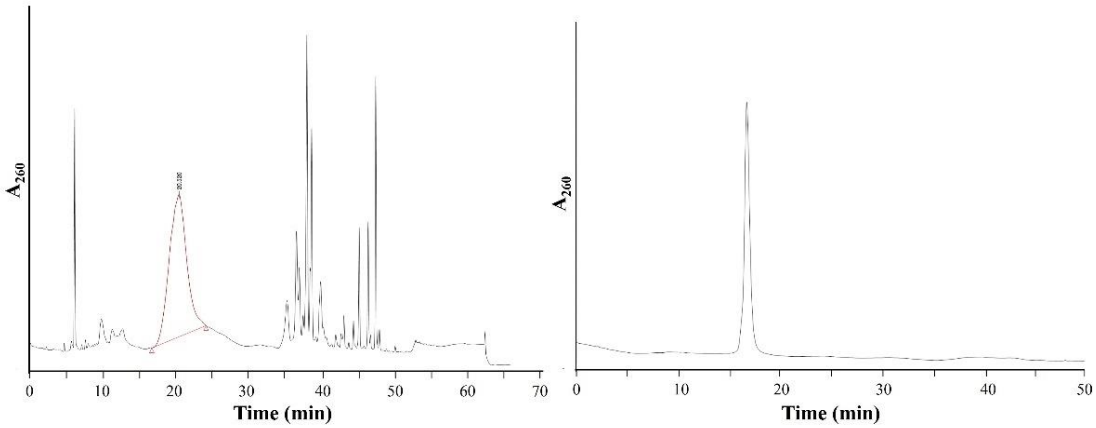

Fig. 2.5 HPLC chromatogram of crude (left, the red peak is target oligomer) and purified (right) products of **PNA03**.

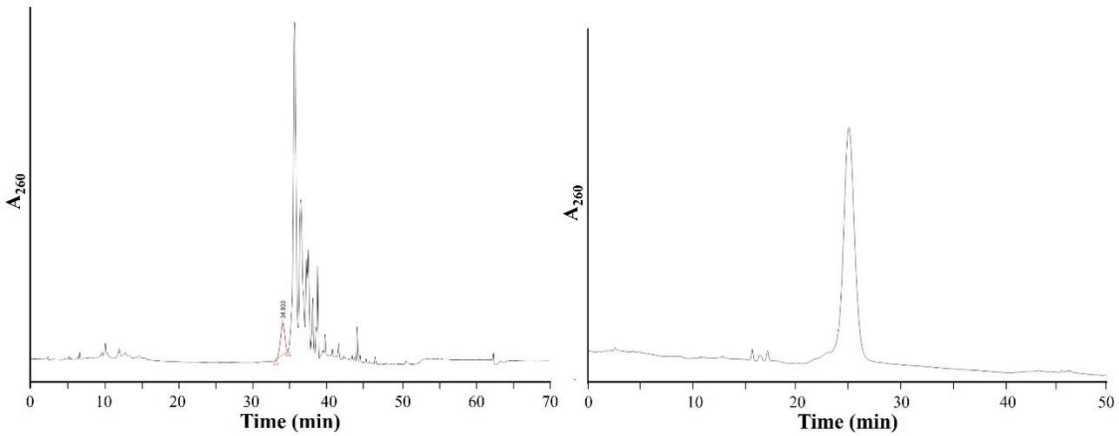

Fig. 2.6 HPLC chromatogram of crude (left, the red peak is target oligomer) and purified (right) products of **PNA04**.

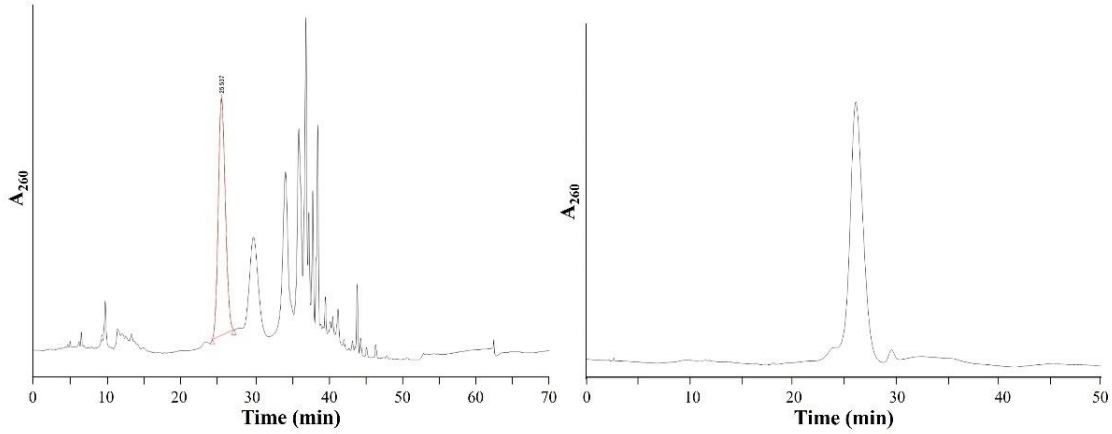

Fig. 2.7 HPLC chromatogram of crude (left, the red peak is target oligomer) and purified (right) products of **PNA05**.

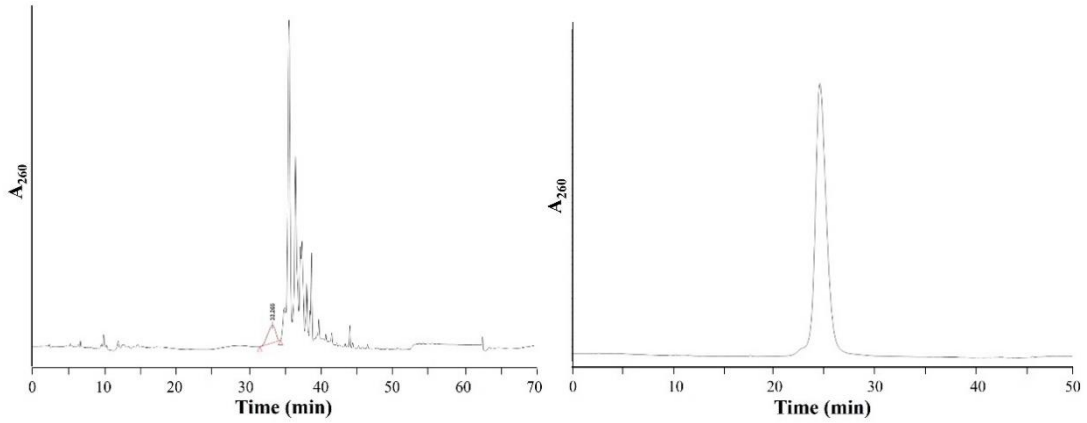

Fig. 2.8 HPLC chromatogram of crude (left, the red peak is target oligomer) and purified (right) products of **PNA06**.

All of the synthesized PNA (**Table 2.2**) and DNA (**Table 2.3**) strands were confirmed by ESI-MS analysis. All measured values agree well with calculated values.

Table 2.2 The sequences of PNA oligomers synthesized and their mass analysis data.[a]

PNA	Sequence[b c]	Molecular formula	*m/z* $[M + 3H]^{3+}$ Calcd.	*m/z* $[M + 3H]^{3+}$ Found
PNA01	H-Lys-TTTCTTTTTTTTPTT-NH_2	$C_{184}H_{236}N_{65}O_{63}$	1455.6	1455.9
PNA02	H-Lys-ATTCTTATTTATPTT-NH_2	$C_{184}H_{232}N_{74}O_{57}$	1464.6	1464.9
PNA03	H-Lys-ATTCTTAAAATTPTT-NH_2	$C_{184}H_{230}N_{80}O_{53}$	1470.6	1470.9
PNA04	H-Lys-ATT_TTATTTATPTT-NH_2	$C_{180}H_{229}N_{71}O_{56}$	1428.3	1428.6
PNA05	H-Lys-AT_CTTATTTATPTT-NH_2	$C_{179}H_{228}N_{72}O_{55}$	1423.3	1423.6
PNA06	H-Lys-ATTC_TATTTATPTT-NH_2	$C_{179}H_{228}N_{72}O_{55}$	1423.3	1423.6

[a]Obtained by ESI-TOF mass spectrometry. [b]**P** = NBP-T unit. [c] _ = abasic PNA unit

Table 2.3 The sequences of DNA oligomer synthesized in this study and their mass analysis data.[a]

DNA	Sequence[b]	Molecular formula	m/z calcd. for $[M + 4e]^{4-}$	Found
DNA04	5'-ATTATTATATTCTTATTTATPTTTT-3'	$C_{263}H_{330}N_{70}O_{163}P_{24}$	1955.3	1954.6
DNA07	5'-ATTCTTAAAATTPTT-3'	$C_{163}H_{201}N_{47}O_{95}P_{14}$	1192.7	1192.0

[a]Obtained by ESI-TOF mass spectrometry. [b]**P** = NBP-T unit.

2.4 CHARACTERIZATION OF NBP-PNA/DNA HYBRIDS

To investigate the effects of NBP group on the global helix stability, we measured the thermodynamic parameter, T_m, of the NBP-PNA/DNA and compared it to that obtained for the perfectly matched unmodified-PNA/DNA duplex. Sample preparation and the machine setup are described in Experimental. The melting curves obtained for the **PNA02**/**DNA06** as well as **PNA07**/**DNA06** are shown in **Fig 2.9**. Analysis of the melting curves determines the T_m for **PNA02**/**DNA06** with NBP attached to be 44.4 °C, which is similar to the corresponding NBP-unmodified **PNA04**/**DNA06** duplex (46.1 °C). This finding verifies that the addition of NBP hardly affects hybridization.

The T_m values for other oligonucleotides are summarized in **Table 2.4** and the corresponding melting curves are shown in Experimental **Fig. S11**. As expected, duplex **PNA04**–**06**/**DNA06**, which has an abasic residue at positions around G in DNA, have T_m ca. 13 °C below that of **PNA02**/**DNA06**. This reflects the loss of hydrogen bond stabilization at the abasic site.

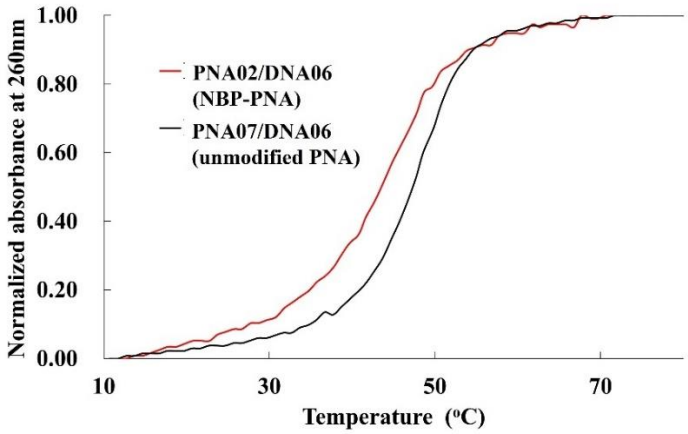

Fig. 2.9 Melting curves for the **PNA02**/**DNA06** (red) and **PNA07**/**DNA06** (black).[76]

Table 2.4 The T_m values for PNA/DNA and DNA/DNA duplexes.

Entry	Double strand structure[a, b]	T_m (°C)
1	DNA01: 5'-TTTTTTTTTTTCTTTTTTTTPTTTT-3' DNA02: 3'-AAAAAAAAAAAGAAAAAAAAAAAAA-5'	54.3[9]
2	PNA01: H-Lys-TTTCTTTTTTTTPTT-NH_2 DNA03: 3'-AAAGAAAAAAAAAAA-5'	55.9
3	DNA04: 5'-ATTATTATATTCTTATTTATPTTTT-3' DNA05: 3'-TAATAATATAAGAATAAATAAAAAA-5'	49.9
4	PNA02: H-Lys-ATTCTTATTTATPTT-NH_2 DNA06: 3'-TAAGAATAAATAAAA-5'	44.4
5	DNA07: 5'-ATTCTTAAAATTPTT-3' DNA08: 3'-TAAGAATTTTAAAAA-5'	37.6
6	PNA03: H-Lys-ATTCTTAAAATTPTT-NH_2 DNA08: 3'-TAAGAATTTTAAAAA-5'	52.9
7	PNA04: H-Lys-ATT_TTATTTATPTT-NH_2 DNA06: 3'-TAAGAATAAATAAAA-5'	31.2
8	PNA05: H-Lys-AT_CTTATTTATPTT-NH_2 DNA06: 3'-TAAGAATAAATAAAA-5'	31.6
9	PNA06: H-Lys-ATTC_TATTTATPTT-NH_2 DNA06: 3'-TAAGAATAAATAAAA-5'	27.1
10	PNA07: H-Lys-ATTCTTATTTATTTT-NH_2 DNA06: 3'-TAAGAATAAATAAAA-5'	46.1

[a] **P** = NBP-T unit. [b] _ = abasic PNA unit

The handedness of NBP-PNA/DNA helices was investigated according to circular dicroism (CD). As depicted in **Fig. 2.10**, the CD spectra of the NBP-PNA/DNA duplexes exhibits a pattern similar to that described in the literature for PNA/DNA duplexes with different sequences.[22] Specifically, two positive bands are observed near 220 nm and in the range of 260–270 nm. These M-shaped CD spectra suggest NBP-PNA/DNA duplexes are conformationally similar to the unmodified PNA/DNA, all of which adopt a right-handed helix.[76]

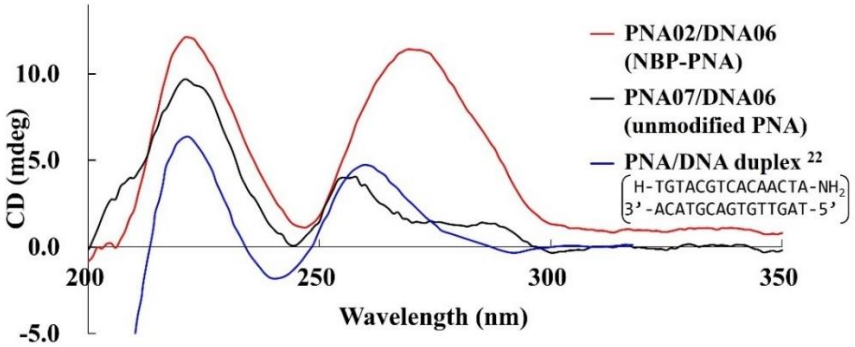

Fig. 2.10 CD spectroscopy for the **PNA02/DNA06** (red), **PNA07/DNA06** (black) and reported PNA/DNA duplex[22] (blue).[76]

Overall, a comparison between the NBP-PNA/DNA duplex and its unmodified counterpart PNA/DNA based on T_m and CD demonstrated that incorporating NBP into the PNA did not induce any notable structural deviations from the right-handed helical conformation.

2.5 SUMMARY

This chapter began with an introduction detailing the design of NBP-PNA conjugates—the NBP group is covalently attached to T in PNA via a short linker and positioned nine nucleobases away from the target G in complementary DNA. The second section then described a novel synthetic pathway for the NBP-T-PNA monomer, where the NBP group is linked to α-methyl position of T via an ethylene linker. Afterwards, the third section established the protocol for solid-phase synthesis of PNA oligomers, and the 6 strands of NBP-PNA with 15mer and a lysine at the N-terminus were prepared. Finally, in order to establish the influence of NBP group on the PNA/DNA helical structure, NBP-PNA/DNA hybrids were studied by means of thermal denaturation measurements (T_m) and CD spectroscopy. The modest differences between NBP-conjugated-**PNA02**/**DNA06** duplex and unmodified **PNA07**/**DNA06** duplex suggest that incorporation of NBP in PNA does not cause any significant structural deviations from the right-handed helix.

Chapter 3: Photooxidation of ssDNA and dsDNA by NBP-PNAs

3.1 INTRODUCTION

This chapter investigates photooxidation properties of NBP-PNA targeted to single-strand DNA (ssDNA) as well as double-strand DNA (dsDNA) models, because understanding the selectivity and efficiency of photoinduced DNA modification is crucial for evaluating the potential application of NBP-PNA in gene manipulation.

Given DNA derivatives can bind nucleic acid (NA) target regions through base pairing with high specificity, numerous efforts have been made to attach reactive groups to oligonucleotides (ONs) to induce DNA damage. For example, a oligonucleotide conjugates with Fe(II)-phthalocyanine complex is able to react as a catalyst to effectively induce DNA damage in the presence of hydrogen peroxide.[89] However, this approach necessitates the presence of hydrogen peroxide. A more straightforward and efficient method for inducing spatially and temporally selective DNA damage involves covalently linking a photosensitizer (PS) to a carrier NA that contains a complementary sequence to the target. Kelly and coworkers, for example, synthesized Ruthenium polypyridyl-ON conjugate to target a ssDNA representing the *bcr-abl* chimeric gene and caused photooxidative damage at Gs.[90] This approach has also been employed to enhance photodynamic therapy (PDT) efficiency. Ming et al. demonstrated the use of a chlorin e6-aptamer ON conjugate for cancer-cell destruction through photoirradiation.[91] What's more, due to the strong affinity to DNA and RNA, along with chemical and biological stability,[92] some DNA mimics, such as peptide nucleic acid (PNA) and locked nucleic acid (LNA), are considered ideal candidates for PDT applications. Yavin et al. has showed that irradiation of rose bengal-PNA conjugates resulted in DNA-PNA photo-cross-linking adducts probably through the Lysine.[69] Another study reported the photocleavage of the Mdm2 oncogene via a series of thiazole orange-LNA triplex forming oligonucleotides.[93]

Unlike the previously mentioned metal complex-ON conjugates, this study uses NBP, a small-volume type II photosensitizer. It is hypothesized that, when bound to DNA in a sequence-dependent manner and subjected to irradiation, the singlet oxygen ($^1O_2$) produced by NBP can selectively oxidize nearby Gs, creating localized oxidative damage.

In parallel, extensive mechanistic studies have contributed valuable insights into the oxidative degradation of DNA, especially G, the most vulnerable unit, in different contexts. G oxidation generates a variety of products that depend on the specific oxidant involved.[46] The main reaction products of 2'-deoxyguanosine (dG), including 7,8-dihydro-8-oxoguanine (8-oxo-dG), 5-guanidinohydantoin (dGh), 2-amino-5-[(2-deoxy-β-D-erythro-pentofuranosyl)amino]-4H-imidazol-4-one (dIz) 2,2-diamino-4-[2-deoxy-β-D-erythro-pentofuranosyl)amino]-5-(2H)-oxazo-lone (dOz), spiroiminohydantoin (dSp), and oxaluric acid (dOxa), and the intermediates are summarized in **Scheme 3.1**.

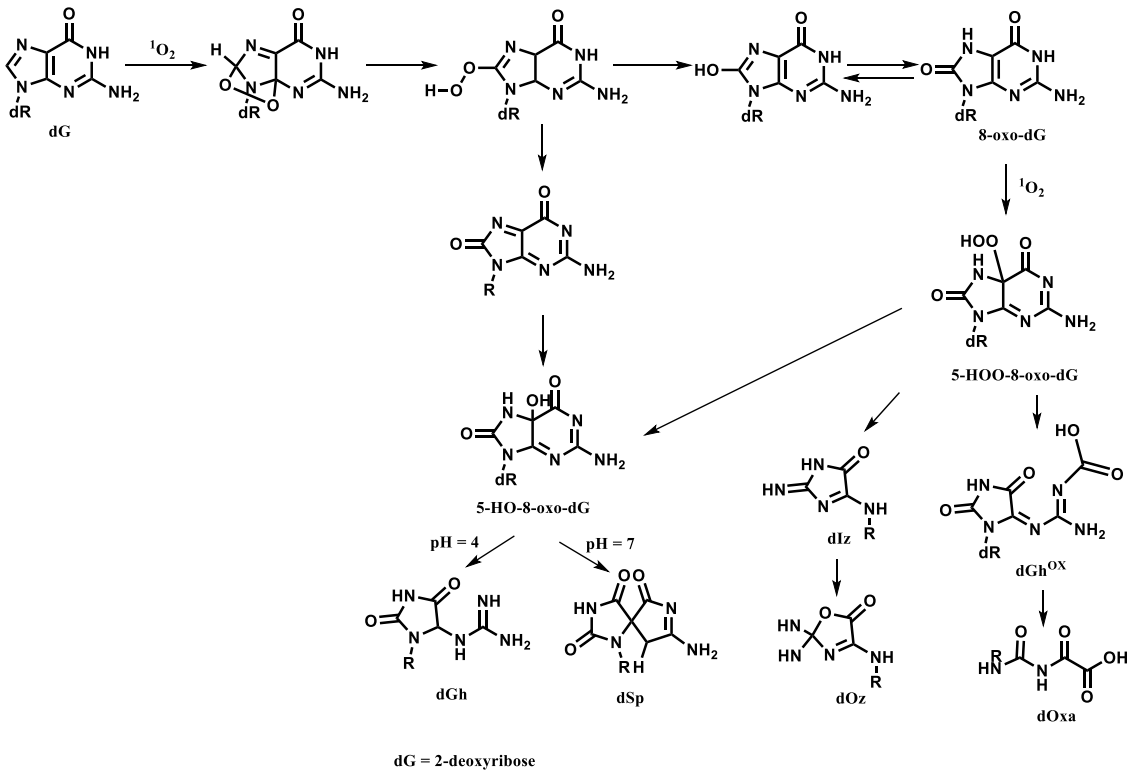

Scheme 3.1 The main $^1O_2$ -mediated oxidation paths and products of dG.[46,47]

Meanwhile, various analytical methods have been developed to identify the G oxidation products and quantify them within DNA. One widely used method involves the hydrolysis of DNA either enzymatically or chemically[94] followed by a reverse-phase HPLC (RP-HPLC) separation based on polarities.[95,96]

In this chapter, section 2 describes the testament of $^1O_2$ production by NBP-PNA/DNA. Then section 3 investigates the photooxidation of ssDNA by NBP-PNAs and external Xylitol-NBP. Section 4 proposes two hypotheses to explain the obtained photooxidation efficiency. Section 5 investigates the site selective photooxidation of dsDNA by NBP-PNAs. Section 6 is the summary of this chapter.

3.2 $^1O_2$ GENERATION ALIBITY OF NBP-PNA/DNA DUPLEX

Recognizing the critical role of $^1O_2$ generation in determining photooxidation efficiency, this study examined $^1O_2$ production in the context of NBP-PNA/DNA systems. Various techniques for detecting $^1O_2$ have been developed, including direct observation of its radiative relaxation to the triplet ground state via near-infrared phosphorescence spectroscopy at 1270 nm and indirect methods that measure the scavenging activity of specific trapping agents.[97,98] Furfuryl alcohol (FA), a simple cyclic diene with a broad absorbance range between 210–230 nm,[99] is a well-established probe molecule for detecting $^1O_2$.[100] The reaction between $^1O_2$ and FA under neutral pH and room temperature conditions is illustrated in **Scheme 3.2**.[101]

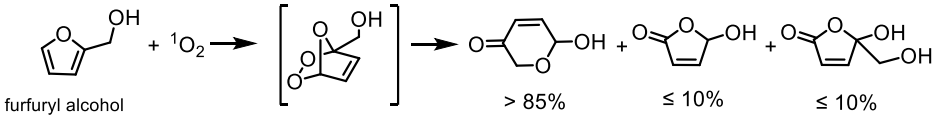

Scheme 3.2 The reaction of $^1O_2$ with FA.

To ensure efficient interception of nearly all $^1O_2$, a high concentration of FA (100 μM) was added to a solution containing NBP-PNA/DNA duplexes (2 μM). Following irradiation, the decrease of FA was monitored using reversed-phase HPLC with UV detection at 216 nm, as shown in **Fig. 3.1** and **3.2**.

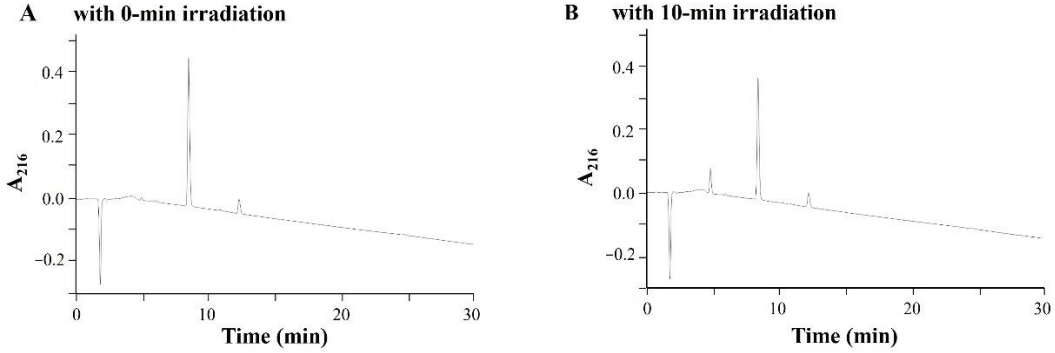

Fig. 3.1 HPLC analysis of furfuryl alcohol degradation by **PNA01**/**DNA03**.

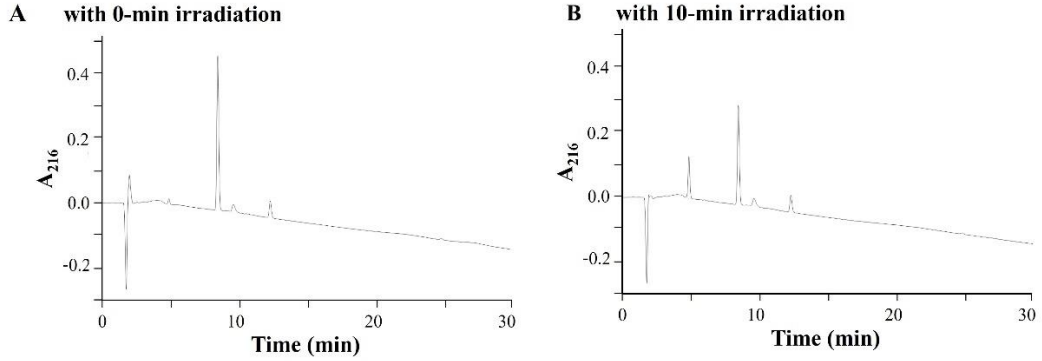

Fig. 3.2 HPLC analysis of furfuryl alcohol photo-oxygenation by **PNA02**/**DNA06**.

The results of HPLC analysis, presented in **Table 3.1**, summarize the outcomes of sensitized photo-oxygenation of FA by tethered NBP. The consumptions of FA after 10 minutes of irradiation with NBP-PNA/DNA duplexes are 19.0% (entry 2) and 35.1% (entry 3), respectively. Comparable to that observed with dsDNA (entry 1, 22%),[9] these similar consumptions of FA suggest that the $^1O_2$ quantum yield of NBP-PNA is analogous to that of NBP-DNA.[76]

Table 3.1. The consumption of furfuryl alcohol (FA) following irradiation with NBP-conjugated duplexes.[a] [76]

Entry	Sequences of double strands[b]	Consumption of FA
1	DNA01: 5'-TTTTTTTTTTTCTTTTTTTTPTTTT-3' DNA02: 3'-AAAAAAAAAAAGAAAAAAAAAAAAA-5'	22%[9]
2	*PNA01: H-Lys-TTTCTTTTTTTTPTT-NH$_2$* DNA03: 3'-AAAGAAAAAAAAAAA-5'	19.0 ± 0.5%
3	*PNA02: H-Lys-ATTCTTATTTATPTT-NH$_2$* DNA06: 3'-TAAGAATAAATAAAA-5'	35.1 ± 1.0%

[a]Conditions: 2-μM duplex, 100-μM FA, 10-mM sodium phosphate buffer with 100-mM NaCl, pH 7.2. Irradiated with 365-nm LED for 10 min at 20 °C. [b] Sequences shown in italics correspond to PNAs. **P**: NBP-T unit.

3.3 PHOTOOXIDATION OF ssDNA BY NBP-PNAs AND EXTERNAL XYLITOL-NBP

3.3.1 Photooxidation Efficiencies of NBP-PNA Conjugates

To assess the photooxidation efficiency of NBP-PNAs, a quantitative HPLC assay was utilized. To emphasize intramolecular photooxidation, the concentration of NBP-PNA/DNA duplexes was maintained at 2 μM, effectively reducing the possibility of intermolecular crosstalk oxidation as demonstrated in previous study.[9] In brief, the duplex solutions were exposed to 365-nm LED irradiation for 10 minutes. Following this step, DNA strands were incubated with a combination of phosphodiesterase I and alkaline phosphatase at 47 ºC to ensure completely enzymatically digestion to mononucleotides.[102] Finally, the separation of the digested products was carried out through reversed-phase HPLC according to a published method.[96] Each experiment was conducted three times, and representative HPLC chromatograms are presented in **Figures 3.3**–**3.7**.[76]

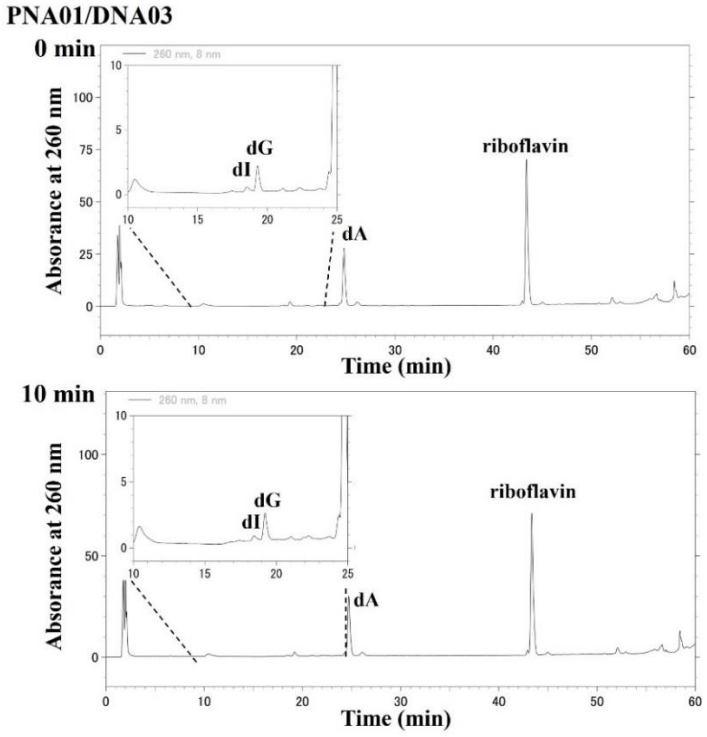

Fig 3.3 HPLC analysis of **PNA01**/**DNA03**: upper (0-min irradiation) and lower (10-min irradiation).

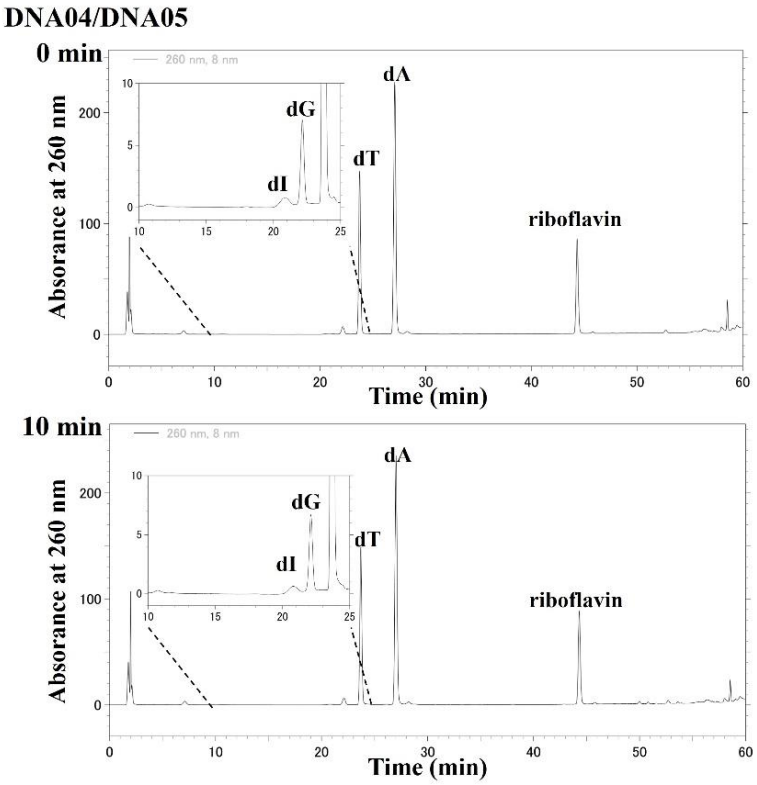

Fig 3.4 HPLC analysis of **DNA04/DNA05**: upper (0-min irradiation) and lower (10-min irradiation).

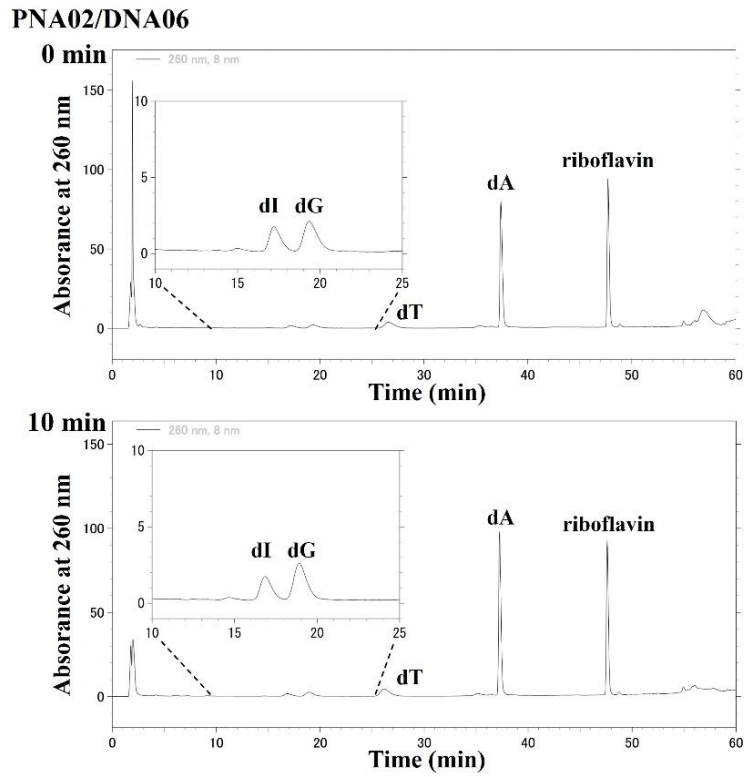

Fig 3.5 HPLC analysis of **PNA02/DNA06**: upper (0-min irradiation) and lower (10-min irradiation).

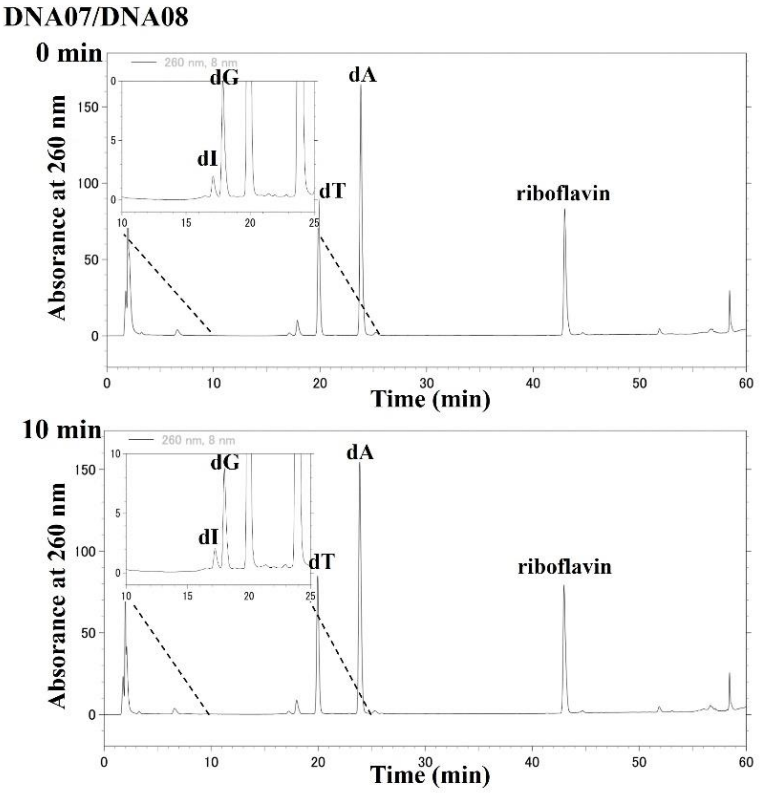

Fig 3.6 HPLC analysis of **DNA07**/**DNA08**: upper (0-min irradiation) and lower (10-min irradiation).

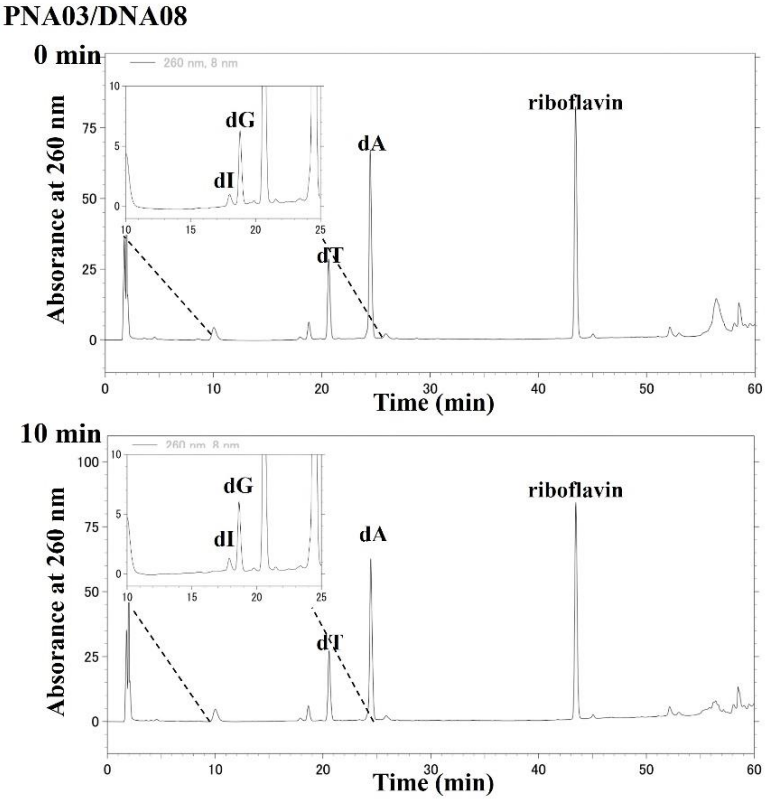

Fig 3.7 HPLC analysis of **PNA03**/**DNA08**: upper (0-min irradiation) and lower (10-min irradiation).

To quantitatively evaluate the reduction of G, the consumption of G was measured relative to adenine (A). The reason for using relative consumption as photoxidation efficiency of G is because the G oxidation products typically include multiple compounds, as shown in section 1, they have various absorption wavelengths and are difficult to be precisely detected. In addition, as the commercial phosphodiesterase may contain an impurity deaminase, deoxyinosine (dI) was generated from dA during digestion. Thus, the relative amount of dG after 10 minutes of photoirradiation was calculated using the following equation:

$$dG = \{[dG]_{10}/([dA]_{10} + [dI]_{10})\}/\{[dG]_0/([dA]_0 + [dI]_0)\} \times 100$$

where $[X]_n$ is the concentration of X after n-min photoirradiation.

The photooxidation efficiencies of NBP-conjugates are summarized in **Table 3.2**. NBP-DNAs (**DNA04** and **DNA07**) with same ethylene linker between NBP and nucleobase T were synthesized according to the published procedures. The data clearly demonstrate that, although the gap sequences between the target G and NBP-T (P) were identical (as indicated by underlines), the photooxidation efficiencies in NBP-PNA/DNA duplexes (entries 2, 4, 6) were markedly lower compared to those in NBP-DNA/DNA duplexes (entries 1, 3, 5). Given that $^1O_2$ generation was confirmed through the FA consumption experiment conducted in section 3.2, it appears that PNA/DNA duplexes may hinder the oxidative effect of $^1O_2$ on G. This inhibitory influence of PNA on DNA oxidation was first reported by Saito et al., although the mechanism have not been elucidated.[70] The underlying reasons are explored further in Section 3.4. Briefly, two hypothesis are discussed in this thesis to explain the reduced oxidation of G in PNA/DNA duplexes: the limited accessibility of $^1O_2$ to G due to extensive base-to-base stacking overlap,[103] and the quenching of $^1O_2$ by the PNA backbone.[76]

Table 3.2. The sequence of NBP-PNA/DNA and DNA/DNA duplexes and their photooxidation efficiencies.[a] [76]

Entry	Double strand structure[b]	Consumption of G
1	DNA01: 5'-TTTTTTTTTTTCTTTTTTTTPTTTT-3' DNA02: 3'-AAAAAAAAAAAGAAAAAAAAAAAAA-5'	62% ± 3%[9]
2	PNA01: H-Lys-TTCTTTTTTTTPTT-NH_2 DNA03: 3'-AAAGAAAAAAAAAAA-5'	4.2 ± 1.5%
3	DNA04: 5'-ATTATTATATTCTTATTTATPTTTT-3' DNA05: 3'-TAATAATATAAGAATAAATAAAAAA-5'	6.7 ± 0.3%
4	PNA02: H-Lys-ATTCTTATTTATPTT-NH_2 DNA06: 3'-TAAGAATAAATAAAA-5'	2.5 ± 0.7%
5	DNA07: 5'-ATTCTTAAAATTPTT-3' DNA08: 3'-TAAGAATTTTAAAAA-5'	9.4 ± 0.7%
6	PNA03: H-Lys-ATTCTTAAAATTPTT-NH_2 DNA08: 3'-TAAGAATTTTAAAAA-5'	2.4% ± 0.2%

[a]Conditions: 2-μM duplex, 10-mM sodium phosphate buffer with 100-mM NaCl, pH 7.2. Irradiated

with 365-nm LED for 10 min at 20 °C. [b]Sequences shown in italics correspond to PNAs. **P**: NBP-T unit. Underlined sequences show the gaps between the target G and NBP-T.

It is important to highlight the influence of sequence-context effects on G oxidation by tethered NBP. Compared with polyA/polyT sequence (entries 1 and 2), interconverting AT base pairs within the gap sequences significantly reduced photooxidation efficiencies in both dsDNA and PNA/DNA duplexes (entries 3, 4, 5, 6). These sequence-dependent effects can be attributed to structural variations in the DNA double helix. DNA stretches composed of poly(dA)/poly(dT) adopt a distinct conformation known as B'-DNA, which is closely related to but notably different from standard B-form DNA.[104] This A-tract structure is generally straighter in solution and features a narrower minor groove and a wider major groove compared to the B-form helix.[105,106] As illustrated in **Fig. 3.8**, the molecular electrostatic potential surface of the major groove in a B-form DNA fiber model (range: -0.1 to 0.1, constructed using w3DNA 2.0) appears uneven, while the surface of the A-tract is comparatively smooth (molecular electrostatic potential (range -0.1 0.1), built by w3DNA 2.0) of B-form DNA fiber model is bumpy, whereas the A-tract is smooth.[107] It could be assumed that on a bumpy surface created by alternating bases $^1O_2$ may collide with irregularities, slowing its diffusion and increasing the likelihood of quenching through interactions with nitrogen atoms. In contrast, on a smooth surface, $^1O_2$ can flow from NBP to G without hindrance.

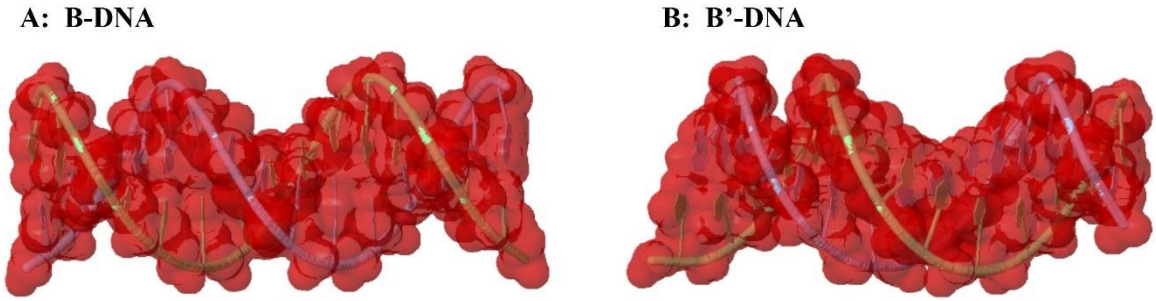

Fig 3.8 Surface of dsDNA fiber models (molecular electrostatic potential (range -0.1 0.1)), A: bumpy surface of major groove in B-DNA d(TAAGAATATATATAA) / d(ATTCTTATATATATT), B: smooth surface of major groove in B'-DNA beta1, poly d(A)/poly d(T).

Furthermore, the formation of a characteristic poly-T/poly-A/poly-T triplex structure[108] has enhanced photooxidation efficiency in certain instances. This occurs when the third strand positions the additional NBP on the 3'-side of G (entry 1 and 3). Such an arrangement increases the likelihood of $^1O_2$ successfully interacting with the target guanine.[9]

3.3.2 Photooxidation Efficiencies of External Xylitol-NBP

To further determine whether the formation of a PNA/DNA duplex inhibits guanine (G) oxidation by $^1O_2$, the photooxidation of G in both PNA/DNA duplexes, dsDNA and ssDNA was investigated using an external water-soluble type II photosensitizer, **xylitol-**

NBP (**Fig. 3.9**). The $^1O_2$-producing quantum yield of **xylitol-NBP** when excited at 337 nm is 0.58 in acetonitrile (CH_3CN).[8]

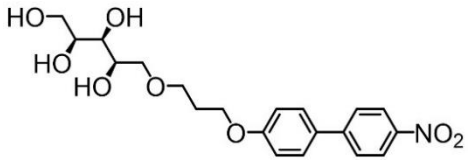

Fig 3.9 Structure of Xylitol-NBP.[76]

The corresponding HPLC charts are displayed in the Experimental **Fig. S16–S18**, and the summarized photooxidation efficiencies are provided in **Table 3.4**. Oxidation of 28% of G was observed in the PNA/DNA duplex (entry 1), which is lower than the oxidation levels in the DNA/DNA duplex (entry 2, 72%) and ssDNA (entry 3, 41%). Such diminished oxidation efficiency in the PNA/DNA duplex suggests that hybridization of PNA to DNA partially inhibits the impact of $^1O_2$ on G oxidation. In addition, the reduced photooxidation reactivity of ssDNA compared to dsDNA is attributed to the lower reduction potential of the GC base pair relative to isolated G.[39,37]

Table 3.4. The sequences of PNA/DNA and DNA/DNA duplexes and DNA oligomer used in the photooxidation study with an external photosensitizer, xylitol-NBP.[a] [76]

Entry	Double strands structure[b]	Consumption of G
1	*PNA04:* *H-Lys-ATTCTTATTTATTTT-NH_2* DNA06: 3'-TAAGAATAAATAAAA-5'	28.9 ± 0.5%
2	DNA09: 5'-ATTATTATATTCTTATTTATTTTTT-3' DNA05: 3'-TAATAATATAAGAATAAATAAAAAA-5'	72.5 ± 4.9%
3	DNA06: 3'-TAAGAATAAATAAAA-5'	41.8 ± 0.6%

[a]Conditions: 2-μM duplex, 10-mM sodium phosphate buffer with 100-mM NaCl, pH 7.2. Irradiated with 365-nm LED for 10 min at 20 °C. [b]Sequences shown in italics correspond to PNAs.

3.4 DISCUSSION AND HYPOTHESIS

3.4.1 Base Stacking in PNA/DNA Duplex Caused Poor Accessibility to G

The difficulty in accessing C8 of G is likely to inhibit the photooxidation because the feasibility of endoperoxide thermal formation is most crucial to the G oxidation process. The widely accepted mechanism of $^1O_2$-induced oxidation of G involves initial [4+2] cycloaddition of $^1O_2$ across the purine ring and the subsequent fast production of 8-oxoG.[109,110,111] It is reported that this nucleophilic attack occurs on the C8 position, which is the most electrophilic position for G, yielding an open zwitterionic intermediate followed by a transient endoperoxide intermediate.[112] (**Fig. 3.10**) This transition from the {G + $^1O_2$} adduct to the endoperoxide is energetically favorable, driven by significant thermodynamic stability of the endoperoxide relative to the initial adduct in its equilibrium configuration. Consequently, the addition onto C8 clearly emerges as the limiting step.[113] However, C8 atoms are not readily accessible when the G is embedded within a helix, further complicating the oxidation process.[49]

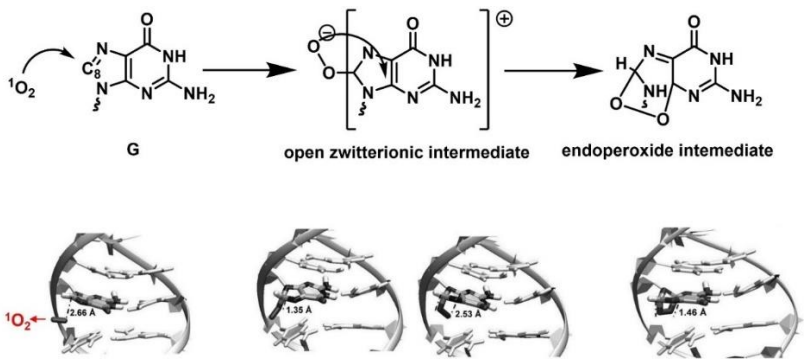

Fig 3.10 Two-step addition of $^1O_2$ to guanine leading to endoperoxide intermediate.[112] Adapted with permission from ref 112. Copyright 2016, John Wiley and Sons.

The notable geometric distinctions between PNA/DNA duplex and dsDNA could contribute to variations in photooxidation efficiency.[114] Such differences include a reduced helical twist in PNA duplexes and greater π-overlap between adjacent bases in PNA[103] Basically, there are three families of DNA helices: B-DNA (represents an average conformation, right-handed orientation), A-DNA (right-handed orientation) and Z-DNA (rare and left-handed orientation).[115] Nevertheless, PNA/DNA hybrid helix adopts a structure different from the above three-dimensional structure, as can be seen in **Fig. 3.11,** and **Table 3.5** pinpoint the exact difference in some parameters for helical structure.[116] In PNA/DNA helices, the base pairs are perpendicular to the helix axis,[117,118] and the average twist of base step is only 28.0°, smaller than that of B-DNA (36.0°) and A-DNA (32.7°).[119] Therefore the resulting overlap may cause the poor accessibility of G within the PNA/DNA duplex.

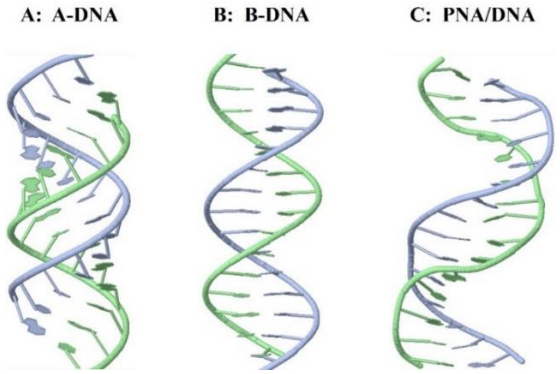

Fig 3.11 Illustrations of different helical structures: A, A-form DNA, B, B-from DNA, C, PNA/DNA duplex, built by w3DNA 2.0.

Table 3.5. Comparison of Helical Parameters (Averaged).[120] Adapted with permission from ref 120. Copyright 2010, American Chemical Society.

Helical parameters (average)			
	Helix type		
	A-DNA duplex	**B-DNA duplex**	**PNA/DNA**
twist (deg)	32.7	36.0	28.0
vertical rise (Å)	2.6	3.4	3.3
bases per turn	11	10	13

An additional observation strengthened this hypothesis that the placement of the abasic site (**Fig. 3.12**) in PNA strand around G (entry 10, 11 and 12 in **Table 3.6**), resulting in much space around G, yield higher photooxidation efficiencies than the fully matched NBP-PNA/DNA (2.5%, entry 4 in **Table 3.2**). The represented HPLC charts are shown in Experimental **Fig. S12–14**, and the photooxidation efficiencies are summarized in **Table 3.6**.

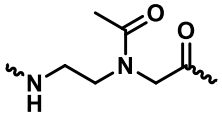

Fig 3.12 Structure of abasic PNA unit.

Table 3.6. abasic NBP-PNA/DNA duplexes and their photooxidation efficiencies.[a]

Entry	**Sequence[b]**	**Consumption of G**
10	***PNA05:*** ***H-Lys-ATT_TTATTTATPTT-NH₂*** **DNA06:** **3'-TAAGAATAAATAAAA-5'**	4.5 ± 1.0%
11	***PNA06:*** ***H-Lys-AT_CTTATTTATPTT-NH₂*** **DNA06:** **3'-TAAGAATAAATAAAA-5'**	9.2 ± 0.3%
12	***PNA07:*** ***H-Lys-ATTC_TATTTATPTT-NH₂*** **DNA06:** **3'-TAAGAATAAATAAAA-5'**	3.2 ± 0.4%

[a]Conditions: 2-μM duplex, 10-mM sodium phosphate buffer with 100-mM NaCl, pH 7.2. Irradiated with 365-nm LED for 10 min at 20 °C. [b]Sequences shown in italics correspond to PNAs. **P**: NBP-T unit. _: abasic PNA unit.

Together, these findings implicate that the base stacking in PNA/DNA duplex caused poor accessibility to G, attributing to the hindrance of the photooxidation by $^1O_2$.

3.4.2 $^1O_2$ Is Quenched Physically by The PNA Backbone

The second hypothesis to explain the low photooxidation efficiency in PNA/DNA is that the diffusion of $^1O_2$ generated by NBP-PNA along the PNA/DNA backbone leads to quenching, because amide solvents typically exhibit faster first-order quenching rates for $^1O_2$ than water,[121] as **Table 3.7** shows some examples. Therefore, it seems that $^1O_2$ diffusion on the PNA surface, coupled with frequent interactions with nitrogen atoms, likely results in a higher quenching rate than when $^1O_2$ diffuses along dsDNA.[103] In contrast, quenching is less likely when $^1O_2$ approaches from above of G.[76]

Table 3.7. The rate constant for physical quenching of $^1O_2$ in different solvents.

Quenching group	Solvent	Rate constant for physical quenching (k_q) (s^{-1})
amide	DMF	1.23×10^7
	DMA	1.36×10^7
H_2O	water	2.4×10^5

Tests in external **xylitol-NBP** are in agreement with this hypothesis. As shown above (Section 3.3.2), the photooxidation efficiency by external NBP is much higher than that by conjugated NBP. This difference may stem from the effect of the diffusion route of $^1O_2$ (along helix surface or in random orientation) on the photooxidation efficiency. As illustrated by **Fig. 3.13**, $^1O_2$ generated from a linked NBP may diffuse one-dimensionally through the major groove and thereby is frequently quenched by nitrogen atoms, resulting in substantial less oxidation to G than that generated from external NBP.

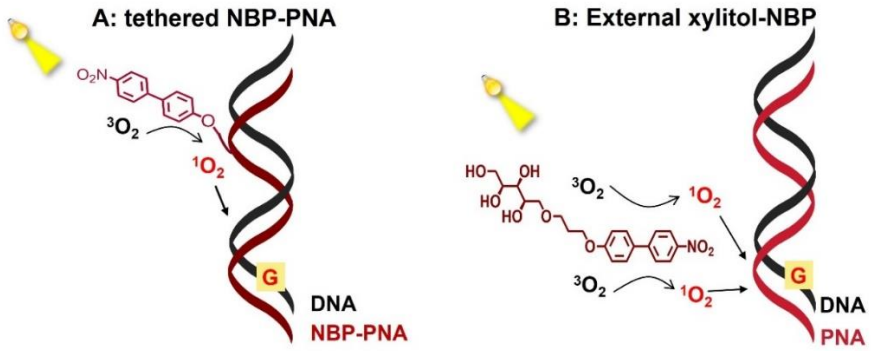

Fig 3.13 Illustration of the diffusion route of $^1O_2$, A: the $^1O_2$ generated from tethered NBP diffuse along duplex surface, A: the $^1O_2$ generated from external **xylitol-NBP** diffuse in random orientation.

3.5 SITE SELECTIVE PHOTOOXIDATION OF dsDNA BY NBP-PNA

Building on the above finding that PNA complexed with DNA inhibit the G photooxidation, particularly when NBP is conjugated to PNA, we hypothesized that irradiating an NBP-PNA complex attached to the sticky end of dsDNA would enable selective photooxidation of G residues within the dsDNA region. Sticky ends are unpaired nucleotides at termini of dsDNA, formed when certain restriction enzymes, such as EcoRI,[122] cut the DNA at slightly offset positions on the two strands. The overhanging part can readily hybridize with a complementary sequence, thus earning the name "sticky ends".[123]

To pinpoint the damage caused by G oxidation, DNA photocleavage experiments were performed. In brief, as illustrated in **Fig. 3.14**, the dsDNA with a sticky end consists of two strands: the shorter AT-mixed sequence has 45 nucleotides (nt), and the G-containing strand possessing 60nt is labeled with fluorescein (Fluorescein amidites, FAM) at 5' and the 3' end overhanging. With NBP-PNA binding to the sticky end of a dsDNA, two target Gs in such complex are positioned at the same distance (9 bases) from NBP-T (**P**), one within the PNA/DNA duplex region and the other in the DNA duplex region. Upon irradiation with 365nm light for 10 min or 1 h, the $^1O_2$ produced from the NBP can react with Gs yielding oxidative modification. Subsequently, the photoirradiated samples were subjected to cleavage treatment, Fpg or hot piperidine, which specially causes strand break at the oxidized G site, resulting in the cleavage with specific length. Finally, regioselectivity in G oxidation can be reflected by analyzing the cleavage products via denaturing polyacrylamide gel electrophoresis (PAGE).

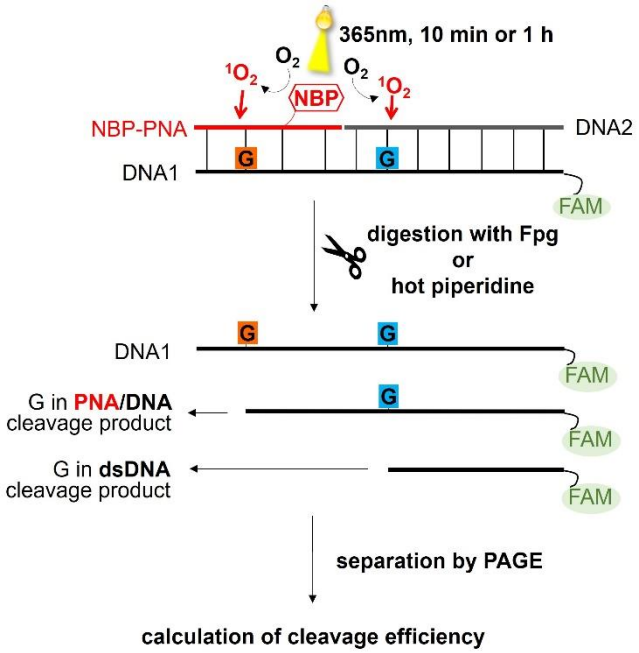

Fig 3.14 Illustration of photooxidation and cleavage experiments to assess the regioselectivity of NBP-PNA.

To digest all oxidized G products, the cleavage treatment of the photoirradiated samples involves two methods due to the complexity of G oxidation chemistry which is briefly summarized in Section 1. One method is bacterial formamidopyrimidine DNA N-glycosylase (Fpg), whose preferential substrate is 8-oxoG which is the primary product of G oxidation with $^1O_2$.[124, 125] (**Scheme 3.3**) The other method is hot piperidine as 8-oxodG is reported to have lower redox potential than G and readily undergoes oxidation to secondary oxidation products, such as dGh and dOxa (**Scheme 3.4**),[126] which are highly labile to hot piperidine treatment (incubation 1M piperidine in water at 95 °C for 45 min), whereas 8-oxodG remains stable under these conditions.[127,128,47] The quantification of each band enables the determination of the yields from each Fpg or piperidine cleavage event.[129]

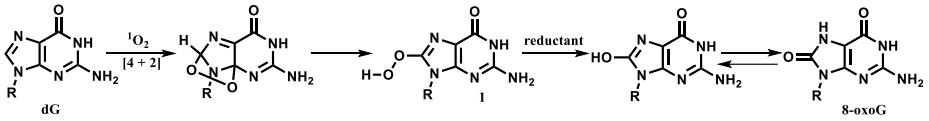

Scheme 3.3 8-oxodG generated from the reaction of $^1O_2$ with G.

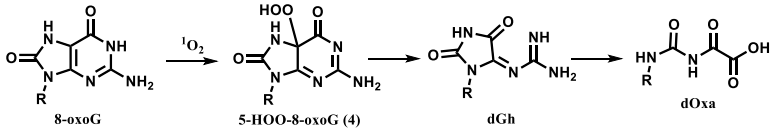

Scheme 3.4 Main oxidation products generated by the reaction of $^1O_2$ with 8-oxoG in DNA strands.

As demonstrated in **Fig. 3.15**, **PNA02** was bound to **DNA10/DNA11**, where the gap sequence within dsDNA region consisted of polyT. Following either 10-min or 1-h irradiation, combined with sufficient Fpg cleavage (4U-12U), only the 38-nt cleavage product was distinctly observed, as confirmed by DNA marker. This result indicates that G in the dsDNA region underwent oxidation to form 8-oxoG. In the case of hot piperidine treatment, the 38-nt cleavage product remained the sole observed fragment. These results suggest that although the oxidation of G in the dsDNA region yield secondary oxidation products, G in the PNA/DNA duplex was intact. Furthermore, the cleavage yield increased with the irradiation extended from 10 min to 1 h in both cases: from 10% to 16% with Fpg treatment, from 4% to 8% with hot-piperidine. This indicates that 10-min irradiation was insufficient for complete photooxidation.[76]

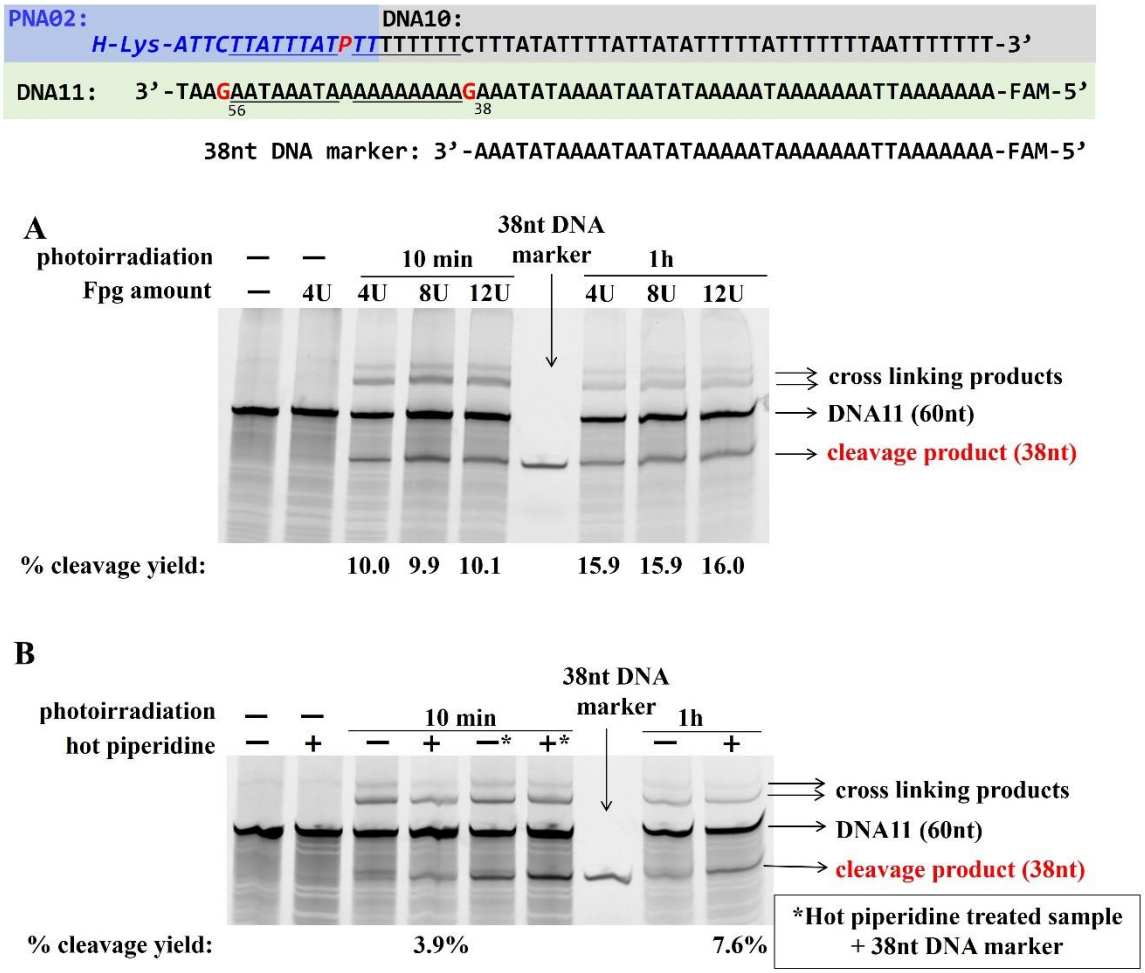

Fig 3.15 Denaturing PAGE for the photooxidation and following cleavage of **PNA02**/sticky-end-dsDNA (**DNA10/DNA11**). The pictures containing the whole gel image are presented in Experimental **Fig S19** and **S20**.[76]

To determine whether the above photooxidation results are unique to the polyA/polyT sequence, then this NBP-PNA conjugate (**PNA02**) was employed to bind and photooxidize a different dsDNA model, **DNA12/DNA13**, where the gap sequence within dsDNA region altered to interconverting AT base pairs (AATTTTAA from A(:**P**) to G in DNA13). As shown in **Fig. 3.16**, similar results were obtained, with only the 38-nt cleavage product detected following both cleavage treatments. Notably, the cleavage yields are 7% (10 min) and 13% (1 h), slightly smaller than above **DNA10/DNA11** (with polyA/polyT gap sequence), 10% and 16%, respectively. The difference in cleavage yields between the two gap sequences aligns with the detrimental effect of interconverting AT sequences on photooxidation efficiency, as discussed in section 3.3.1.[76]

These two gel electrophoresis results confirm that photoirradiation of the complex NBP-PNA/sticky-end-dsDNA selectively oxidizes only the G in the dsDNA region.

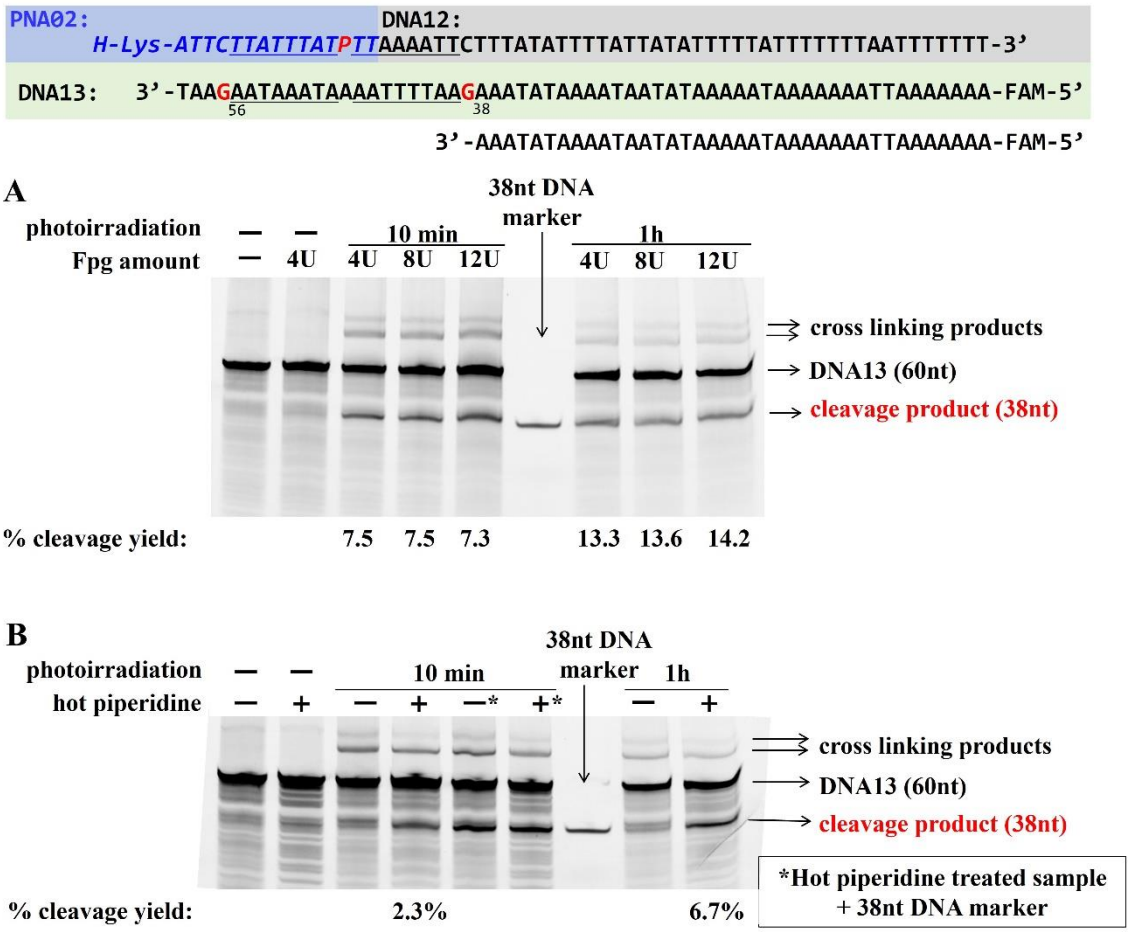

Fig 3.16 Denaturing PAGE for the photooxidation and following cleavage of **PNA02**/sticky-end-dsDNA (**DNA12/DNA13**). The pictures containing the whole gel image are presented in Experimental **Fig S19** and **S20**.[76]

To verify that it is PNA complexed with DNA inhibit the photooxidation, the same photocleavage experiments were then conducted using an 15mer NBP-DNA conjugate. A 15mer NBP-DNA (**DNA07**) was bound to the sticky end of **DNA14**/**DNA15** duplex, in which two target Gs were positioned at an identical distance (9 bases) from NBP. As shown in **Fig. 3.17**, two distinct cleavage products with different lengths were detected after Fpg and hot piperidine cleavage. According to the DNA markers, product 1 was 56nt long and product 2 was 38nt long, corresponding exactly to the two G oxidation and cleavage products. These results show that NBP-DNA can induce photooxidation of G at both the positions.[76]

Altogether, these findings suggest that NBP-PNA has significant potential as a site-selective photooxidation agent, capable of inducing selective oxidation in dsDNA.

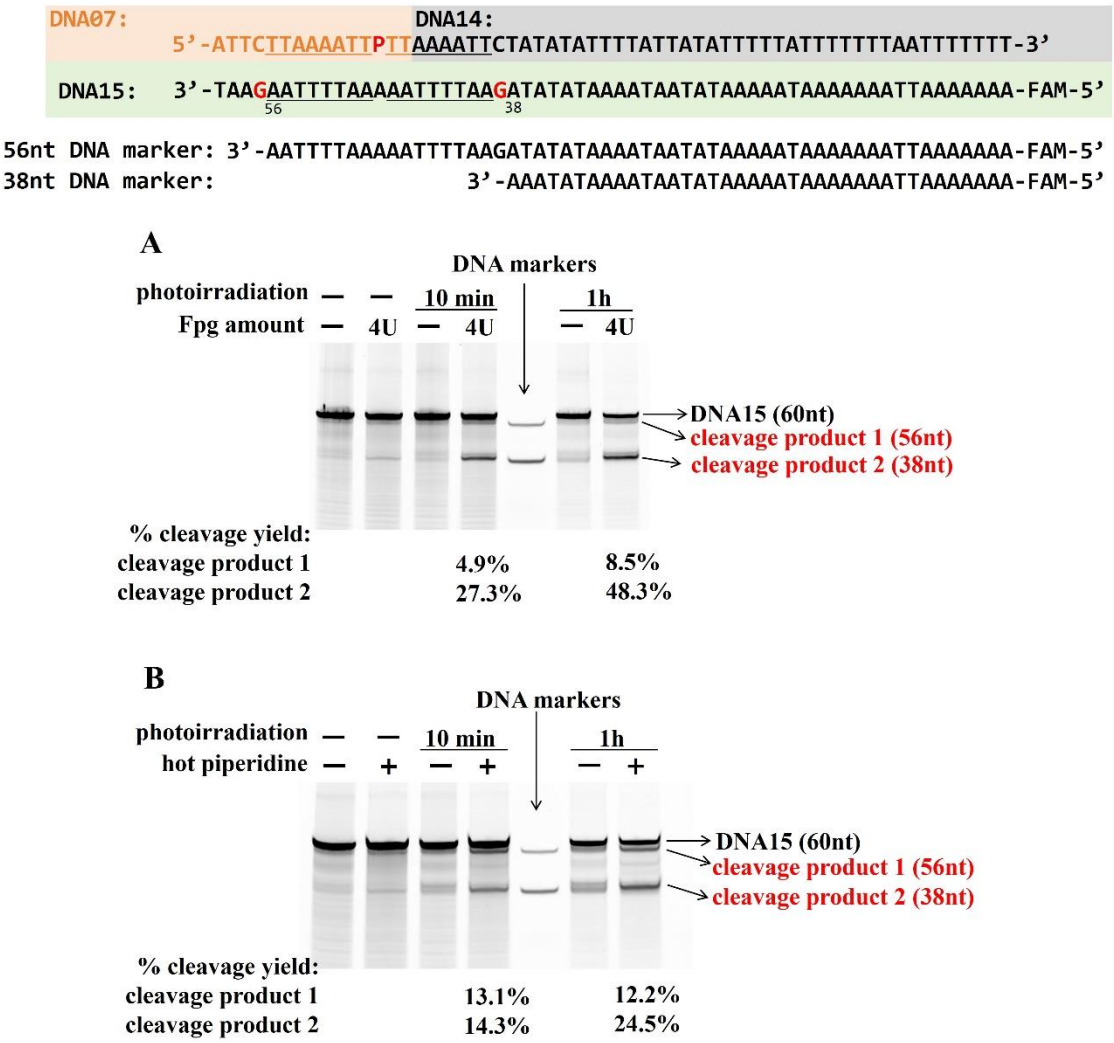

Fig 3.17 Denaturing PAGE for the photooxidation and following cleavage of **DNA07**/sticky-end-dsDNA (**DNA14/DNA15**). The pictures containing the whole gel image are presented in Experimental **Fig S19** and **S20**.[76]

What's more, data in **Fig. 3.17** shows the cleavage yield for 38nt products are generally higher than 56nt products. After 10-min photoirradiation and Fpg treatment, cleavage yield of 38nt products is 27%, clearly higher than that of 56nt (4.9%); with hot-piperidine treatment cleavage yield for 38nt product is 14.3%, slightly higher than 56nt (13.1%). However, after 1-h irradiation, the difference sharply increases: cleavage yield of 38nt products with Fpg is 48.3%, and with hot-piperidine is 24.5%, extremely higher than that of 56nt product, 8.5% and 12.2%, respectively. This indicats that the nucleophilic attack to the C8 position of G by $^1O_2$ is easier when $^1O_2$ comes from 3' of that strand. That also agree with the results that absic **PNA11**/**DNA06** (abasic site is placed at the 3' side of G) possess higher photooxidation efficiency than **PNA12**/**DNA06** (abasic site is placed at the 5' side of G). There seems to be a tendency that the relative orientation of NBP to G, namely the direction of diffusion of $^1O_2$, has an effect on the photooxidation efficiency.

3.6 SUMMARY

To conclude, the present chapter investigates photooxidation properties of NBP-PNA conjugate to ssDNA and dsDNA with a sticky end.

Section 1 is the introduction of this chapter, including some examples of oligonucleotide conjugates for inducing oxidative damage to DNA and the oxidation of G by $^1O_2$. In section 2, the $^1O_2$ production ability of NBP-PNA is confirmed by monitoring furfuryl alcohol via HPLC. Two NBP-PNA/DNA duplexes are able to generate $^1O_2$ at the same level as NBP-DNA/DNA. In section 3, the photooxidation efficiency of conjugated NBP and external xylitol-NBP in the context of PNA/DNA duplex and dsDNA are quantitatively investigated by RP-HPLC. The results reveal that the efficiencies of G photooxidation in PNA/DNA duplexes were significantly lower than those in corresponding dsDNA duplexes, either by conjugated or external NBP. It is reasonable to assume that the PNA complexed with DNA suppresses G oxidation. What's more, the external NBP has much better photooxidation efficiency than NBP-PNA conjugates. And it is also found that the placements of the abasic site in PNA strand around G, resulting in much space around G, yield higher photooxidation efficiencies than the fully matched NBP-PNA/DNA. Finally, two hypotheses were presented to explain the observations: 1. the base stacking within PNA/DNA duplex reduces accessibility to G, therefore preventing the $^1O_2$ oxidation, 2. $^1O_2$ produced from NBP-PNA is likely quenched by amide bond during diffusion along the PNA/DNA backbone. In section 4, the photooxidation of NBP-PNA binding to the sticky end of a dsDNA is investigated via gel electrophoresis experiments. The results demonstrate the site-selective photooxidation of NBP-PNA conjugates as it is able to photooxidize G only in the dsDNA region whereas the G in sticky end is intact due to formation of duplex with PNA. (**Fig. 3.18**)

Our findings in this chapter that the oxidation of G by $^1O_2$ is extremely inhibited by PNA binding and the regio-selective photooxidation of NBP-PNA conjugate complexed with sticky end of a dsDNA indicates the NBP-PNA conjugate is a potential tool to site-specifically induce oxidation into dsDNA.

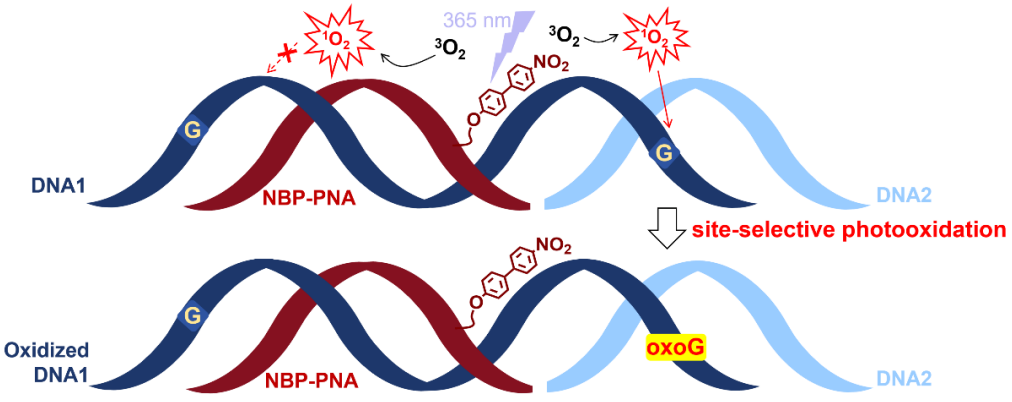

Fig 3.18 Illustration of the site-selective photooxidation of NBP-PNA.

Chapter 4: End-invasion and Photooxidation of dsDNA by NBP-PNA

4.1 INTRODUCTION

This chapter is concerned with the invasion of NBP-PNA into dsDNA and the photooxidation of PNA/dsDNA invasion complex. In Chapter 3, it was observed that the NBP-PNA complexed with the sticky end of dsDNA can site-selectively photooxidize Gs in dsDNA region. The purpose of this small-size photooxidation method is to invade and induce oxidative damage to genome DNA, in view of this, a more meaningful investigation would be conducted in terms of dsDNA invasion into complex by NBP-PNA.

The unique ability of PNA to unwind and insert itself into a DNA helix makes it an excellent tool for gene editing.[65] This invasion occurs when the energy required to dissociate the DNA duplex is offset by the formation of a more stable PNA/DNA duplex.[10] However, initially designed PNAs with a poly(N-(2-aminoethyl)glycine) backbone achieve efficient invasion only under specific conditions. Besides homopurine and homopyrimidine targets,[130] mixed-sequence PNAs can invade supercoiled plasmid DNA.[131,132] As to linear dsDNA, it is reported the mixed-base PNAs without special modification are able to invade into dsDNA termini, and it is end-invasion.[133] To enhance invasion efficiency, researchers have focused on modifying PNA backbones and nucleobases.

An elegant example of backbone modification is gamma (γ)-substituents. Several studies reported that enhanced hybridization properties of PNA are achieved by introducing (*S*)-Me[134,135] or (*R*)-mini diethylene glycol (PEG)[136] stereogenic center at the γ-position. (**Fig. 4.1**) Such modification allows the PNA oligomer pre-organizes into a right-handed helix, resulting in rapid interception to the dsDNA target and stable invasion complex.

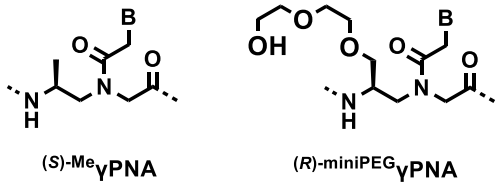

Fig. 4.1 Chemical structures of (*S*)-Me[134] or (*R*)-miniPEG[136] modified γPNA.

In parallel, nucleobase modification can also enhance invasion efficiency. One notable strategy is double duplex invasion. Invasion is facilitated by substituting the standard adenine (A) and thymine (T) in pseudo-complementary PNAs (pcPNAs) with 2,6-diaminopurine (D) and 2-thiouracil (Us), (**Fig. 4.2**) enabling simultaneous binding to both strands of the target dsDNA and the repulsion between the two PNA strands. pcPNAs are unable to pair with each other due to steric hindrance caused by the interaction between the 2-NH_2 group of D and the 2-S group of Us.[137]

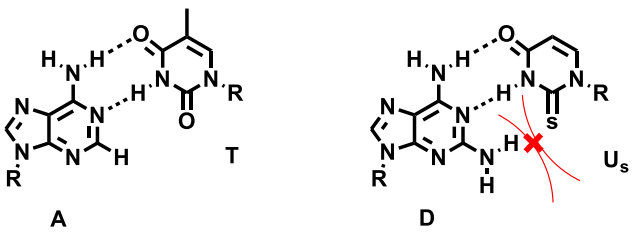

Fig. 4.2 Chemical structures of conventional AT base pair, and the steric repulsion between 6-diaminopurine (D) and 2-thiouracil (U_s).[137]

Similarly, pseudoisocytosine (J) (**Fig. 4.3**) has been developed to improve strand invasion through triplex formation by tail-clamp PNA (tcPNA). A tcPNA molecule consists of two pyrimidine-PNA strands with mirror-symmetric sequences connected by a flexible linker. This design allows the tcPNA to bind to the complementary DNA strand, with one PNA strand establishing Watson–Crick hydrogen bonds and the other forming Hoogsteen hydrogen bonds.[138]

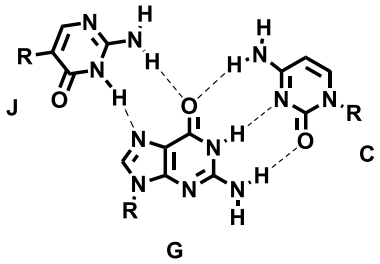

Fig. 4.3 Chemical structures of CG base pair with Watson–Crick hydrogen bonds, and J binding to G with Hoogsteen hydrogen bonds.[138]

At the initial stage of the NBP-PNA conjugate study, we did not modify the PNA backbone in order to minimize the effect of the specific modification components on the photooxidation. Therefore, in present study the NBP-PNA end-invasion mode is used to investigate the invasion and photooxidation properties.

In this chapter, section 2 describes the end-invasion of NBP-PNA to dsDNA models. Section 3 is about the photoxidation of PNA/dsDNA invasion complex. Section 4 discusses the effect of PNA self-assembly on DNA photooxidation. Section 5 is the summary of this chapter.

4.2 END-INVASION OF NBP-PNA TO dsDNA MODELS

4.2.1 dsDNA with Mixed-AT Sequence

To investigate whether this new NBP-PNA conjugate is capable of inserting into dsDNA, the invasion of NBP-PNA into dsDNA termini was examined by non-denaturing PAGE, which reflects the secondary structure of DNA. As discussed in section 1, without specific modification the invasion efficiency of mixed-base PNA is limited due to energy barrier. However, the end-invasion can bypass this limitation of common PNAs.

To precisely analyze the regio-selectivity of G oxidation by NBP-PNA, derived from sticky-end-dsDNA in Chapter 3, a mixed-AT dsDNA sequence with two Gs (**DNA13**/**DNA16**, **Fig. 4.4**) was used as model, where one is in the PNA binding region and the other is assumed to be in dsDNA region after invasion. 20 equivalent (eq.) and 50 eq. NBP-PNA was incubated with 1 eq. dsDNA at 37 ºC overnight in two kinds of low-salt buffer (10 mM sodium phosphate buffer, with 0 mM or 20mM NaCl, pH 7.2), as presently in most cases the PNA invading is limited to relatively low ionic strengths.[136] Then the mixture was separated by non-denaturing PAGE. Notably, as the only **DNA13** containing the PNA binding region is labeled by fluorescein FAM at 5', SYBR Gold staining was used to monitor **DNA16**. SYBR Gold is a widely-used nucleic acids intercalator, which is able to detect dsDNA and ssDNA.[139] The result of non-denaturing PAGE is shown in **Fig. 4.4**, the upper gel image is the detection of FAM, besides the **DNA13**/**DNA16** duplex and **DNA13** single strand, new and wide bands, emphasized by red rectangle, were observed in samples incubated in 10 mM sodium phosphate buffer with 0 mM NaCl. However, after stained by SYBR Gold (lower gel image), the ss**DNA16** appeared, circled by orange rectangle, suggesting the dissociation of **DNA13**/**DNA16** duplex.

The observed retarded wide band is probably because the polyT PNA sequence formed clip structure, PNA/DNA/PNA triplex, with A-tracts in **DNA13**. (**Fig. 4.5**)[140]

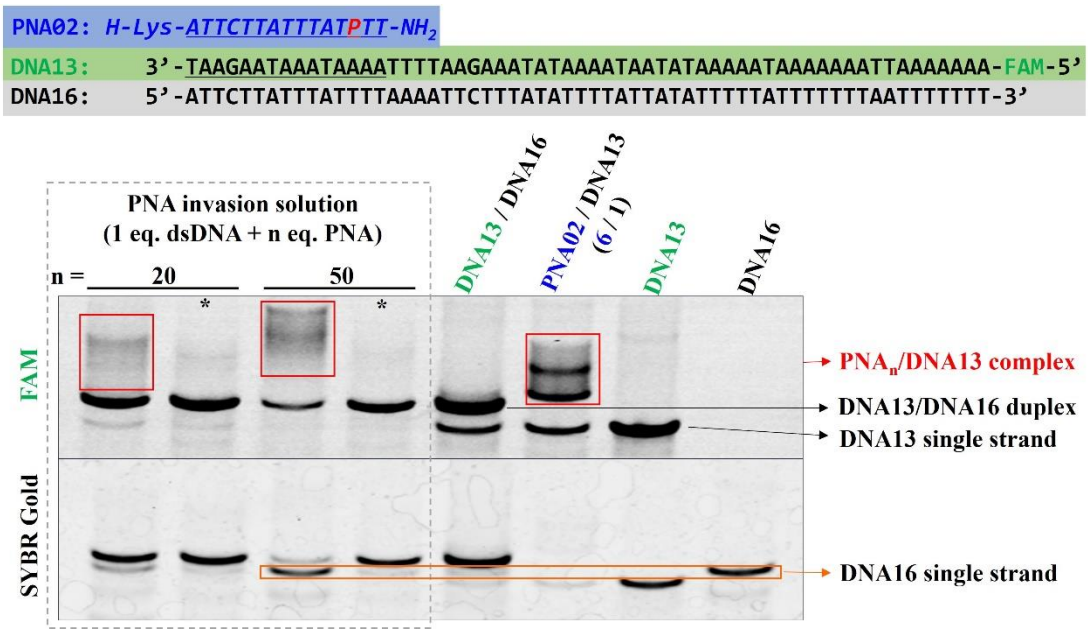

Fig. 4.4 The sequence of NBP-PNA conjugate (**PNA02**) and mixed-AT sequence dsDNA (**DNA13**/**DNA16**), and the non-denaturing PAGE of incubation solutions of NBP-PNA and dsDNA. Condition: (from left to right) lane 1: 40-nM dsDNA, 800-nM NBP-PNA (20 eq.) in buffer 1; lane 2: 40-nM dsDNA, 800-nM NBP-PNA (20 eq.) in buffer 2; lane 3: 40-nM dsDNA, 2-μM NBP-PNA (50 eq.) in buffer 1; lane 4: 40-nM dsDNA, 2-μM NBP-PNA (50 eq.) in buffer 2, lane 5: 40-nM dsDNA (**DNA13**: **DNA16** = 1:1.2) in buffer 1, lane 6: **PNA02** (240-nM) / **DNA13** (40-nM) complex (after annealing) in buffer 1, lane 7: 40-nM **DNA13** in buffer 1, lane 8: 40-nM **DNA16** in buffer 1. Buffer 1: 10 mM sodium phosphate buffer, with 0 mM NaCl, pH 7.0.
*Buffer 2: 10 mM sodium phosphate buffer, with 20 mM NaCl, pH 7.0.
The pictures containing the whole gel image are presented in Experimental **Fig S21**.

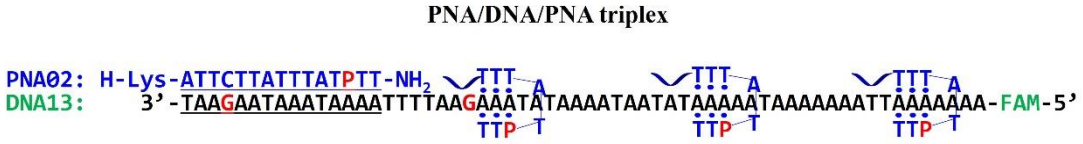

Fig. 4.5 Possible PNA/DNA/PNA triplex structure formed by **PNA02** and **DNA13**.

4.2.1 dsDNA with Mixed-ATCG Sequence

To avoid the clip PNA/DNA/PNA triplex forming, a mixed-ATCG dsDNA (**DNA17**/**DNA18**, shown in **Fig. 4.6**) was used to test the invasion ability of NBP-PNA. **DNA17** contains the PNA binding-region and is labeled with FAM. 20–100 eq. NBP-PNA was incubated with 1 eq. dsDNA at 37 ºC overnight in 10 mM sodium phosphate buffer (with 0 mM or 20 mM NaCl, pH 7.2). Then the incubation samples were analyzed by non-denaturing PAGE with FAM detection and following SYBR Gold-staining detection. The result is shown on **Fig. 4.6**. In the upper gel image of FAM, with

80 and 100 eq. NBP-PNA, a new band (emphasized by red rectangle) was observed. In addition, the result of SYBR Gold staining showed the amount of ssDNA (circled by orange rectangle) did not increase, indicating the maintaining of DNA duplex. Therefore, it can be inferred that the retard band is NBP-PNA end-invasion complex.

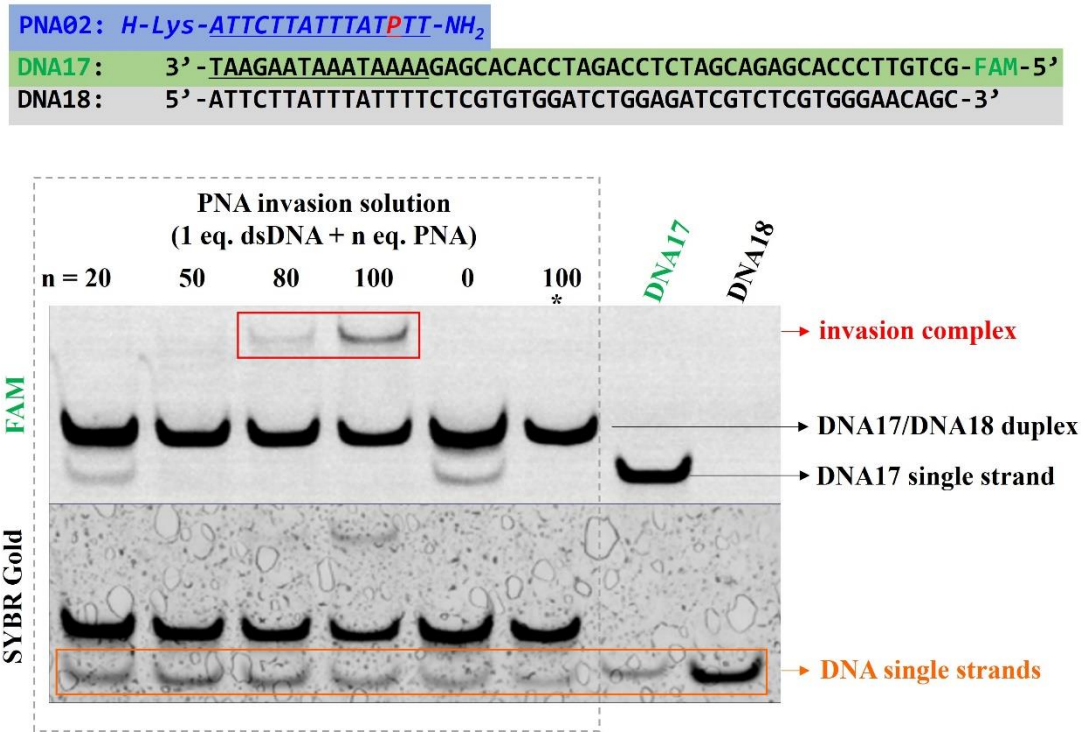

Fig. 4.6 The sequence of NBP-PNA conjugate (**PNA02**) and mixed-ATCG sequence dsDNA (**DNA17**/**DNA18**), and the non-denaturing PAGE of incubation solutions of NBP-PNA and dsDNA. Condition: (from left to right) lane 1: 40-nM dsDNA, 800-nM NBP-PNA (20 eq.) in buffer 1; lane 2: 40-nM dsDNA, 2-μM NBP-PNA (50 eq.) in buffer 1; lane 3: 40-nM dsDNA, 3.2-μM NBP-PNA (80 eq.) in buffer 1; lane 4: 40-nM dsDNA, 4-μM NBP-PNA (100 eq.) in buffer 2, lane 5: 40-nM dsDNA (**DNA17**: **DNA18** = 1:1.2) in buffer 1, lane 6: 40-nM dsDNA, 4-μM NBP-PNA (100 eq.) in buffer 2, lane 7: 40-nM **DNA17** in buffer 1, lane 8: 40-nM **DNA18** in buffer 1.
Buffer 1: 10 mM sodium phosphate buffer, with 0 mM NaCl, pH 7.0.
*Buffer 2: 10 mM sodium phosphate buffer, with 20 mM NaCl, pH 7.0.
The pictures containing the whole gel image are presented in Experimental **Fig S22**.

To conclude, in this section, two kinds of dsDNA model were used to test the invasion ability of NBP-PNA. In the case of mixed-AT dsDNA with several A-tract within **DNA13**, the polyT sequence in PNA readily bounded to **DNA13** and dissociate DNA duplex. In terms of mixed-ATCG sequence, the formation of end-invasion complex of NBP-PNA/dsDNA was confirmed, verifying the addition of NBP did not hamper the invasion of PNA.

4.3 PHOTOOXIDATION OF NBP-PNA/dsDNA INVASION COMPLEX

It is hypothesized that the exposure of NBP-PNA/dsDNA to 365-nm light would produce $^1O_2$, yielding G oxidation products in DNA. To test such lesion, the invasion solution of 100eq. NBP-PNA and 1 eq. dsDNA (**DNA17**/**DNA18**) was subjected to photoirradiation and cleavage treatment with Fpg and hot piperidine. (**Fig. 4.7**) As explained in Chapter 3, the Fpg and hot piperidine treatment can cleavage DNA strand at the position of G oxidation products. And the subsequent denaturing PAGE can separate DNA strands according to their length. After detecting the FAM fluorescence, SYBR Gold-staining detection was conducted to demonstrate the cleavage DNA products without FAM. The results of non-denaturing gel are shown in **Fig. 4.8**. The most left lane in each gel is the control which shows the migration of intact **DNA17** and **DNA18** (51nt). As can be seen clearly in the gel, no cleavage products can be observed.

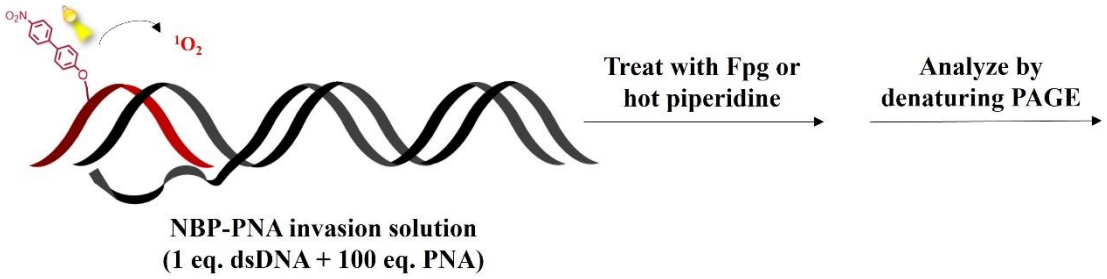

Fig. 4.7 Illustration of photoirradiation and cleavage treatment to invasion solution containing 100 eq. NBP-PNA and 1 eq. dsDNA.

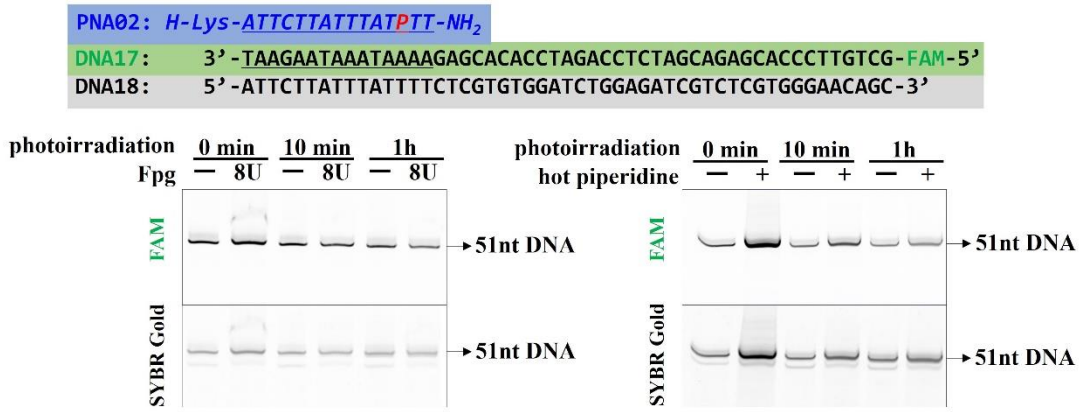

Fig. 4.8 Denaturing PAGE of photoirradiation and cleavage treatment to invasion solution containing 100 eq. PNA and 1 eq. dsDNA. Condition: 40-nM dsDNA, 4-μM NBP-PNA (100 eq.) in 10 mM sodium phosphate buffer with 0 mM NaCl, pH 7.2, incubated at 37 ºC overnight. 365-nm light, at 37 ºC for 0 min, 10 min or 1 h. Cleavage with Fpg, 8U, 37 ºC for 3 h, or 1-M piperidine in H_2O, 37 ºC for 3 h. 20% denaturing

PAGE (7-M urea) and electrophoresed at 200 V. The pictures containing the whole gel image are presented in Experimental **Fig S24 and S25**.

One possible reason is that the non-specific interaction between PNA aggregator and DNA inhibit the photooxidation. Several studies reported that PNAs tend to self-aggregate and adhere to hydrophobic surfaces and other macromolecules, such as DNA in a nonspecific manner.[141,142,136]

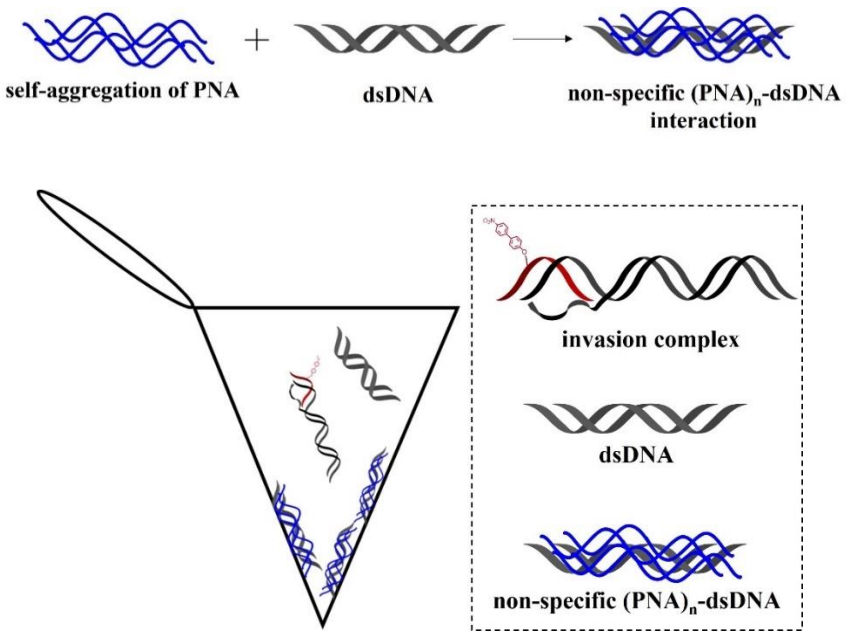

Fig. 4.9 Illustration of self-aggregation: upper, PNA's self-aggregation and non-specific interaction with dsDNA; lower, $(PNA)_n$-DNA aggregation is adsorbed onto hydrophobic surface of microtube, and invasion complex and dsDNA are in solution.

There is evidence for this assumption. After the incubation of large amount NBP-PNA (100–200 eq.) with dsDNA (**DNA17**/**DNA18**, 1 eq., 40nM) at 37 ºC overnight in 10 mM sodium phosphate buffer (with 0 mM NaCl, pH 7.2), certain portion of solution (18 μL) was taken and loaded into gel, then these samples were analyzed by non-denaturing PAGE. Th result is shown in **Fig. 4.10**, in the cases of both FAM image (upper) and SYBR Gold staining image (lower), fluorescence intensity of each band in the 200 eq. NBP-PNA incubation sample (third lane from the left), including invasion complex, **DNA17**/**DNA18** duplex and ssDNA, obviously lower than that of 100 and 150 eq. incubation sample. The decrease of fluorescence intensity of band in gels suggests that the amount of DNA, including invasion complex, **DNA17**/**DNA18** duplex and ssDNA in solutions clearly decrease, probably because the $(PNA)_n$-DNA aggregation was adsorbed onto hydrophobic surface.[142]

PNA02: H-Lys-ATTCTTATTTATPTT-NH_2

DNA17: 3'-TAAGAATAAATAAAAGAGCACACCTAGACCTCTAGCAGAGCACCCTTGTCG-FAM-5'

DNA18: 5'-ATTCTTATTTATTTTCTCGTGTGGATCTGGAGATCGTCTCGTGGGAACAGC-3'

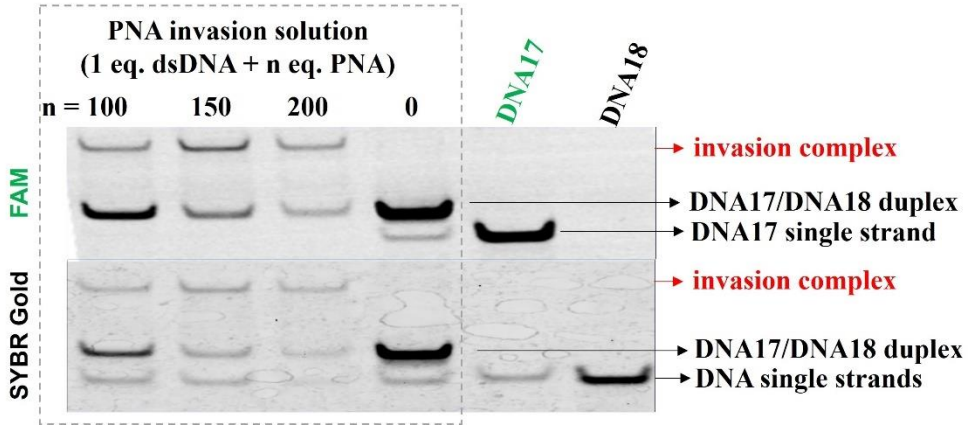

Fig. 4.10 The sequence of NBP-PNA conjugate (**PNA02**) and mixed-ATCG sequence dsDNA (**DNA17**/**DNA18**), and the non-denaturing PAGE of incubation solutions of NBP-PNA and dsDNA. Condition: (from left to right) lane 1: 40-nM dsDNA, 4-μM NBP-PNA (100 eq.) in buffer; lane 2: 40-nM dsDNA, 6-μM NBP-PNA (150 eq.) in buffer; lane 3: 40-nM dsDNA, 8-μM NBP-PNA (200 eq.) in buffer; lane 4: 40-nM dsDNA (**DNA17**: **DNA18** = 1:1.2) in buffer, lane 5: 40-nM DNA17 in buffer, lane 6: 40-nM DNA18 in buffer.
Buffer: 10 mM sodium phosphate buffer, with 0 mM NaCl, pH 7.0.
The pictures containing the whole gel image are presented in Experimental **Fig S23**.

4.4 THE EFFECT OF PNA SELF-ASSEMBLY ON PHOTOOXIDATION

To test whether the PNA self-aggregation and nonspecific interaction with dsDNA has effect on the photooxidation of DNA by NBP, as depicted in **Fig. 4.11,** the photooxidation by external **xylitol-NBP** (100 eq., 4μM) and cleavage with hot-piperidine were conducted using a serious of invasion solution of unmodified-PNA (**PNA04**, 1–100 eq., the sequence can be found in **Fig. 4.12**) and dsDNA (**DNA17**/**DNA18**).

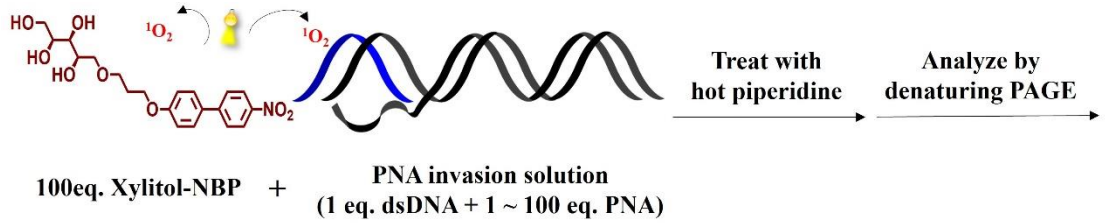

Fig. 4.11 Illustration of photoirradiation and cleavage treatment to invasion solution containing 100 eq. unmodified-PNA and 1 eq. dsDNA.

To the invasion solutions of PNA (1–100 eq.) and dsDNA (1 eq.) was added **xylitol-NBP** (100 eq.), a water-soluble type II photosensitizer. Then the mixtures were irradiated with 365-nm light for 1h and treated by 1-M piperidine (95 °C, 45 min) to cause chain breaks of the oxidative modification. Subsequently, the denaturing PAGE can separate DNA strands based on their lengths, and finally the SYBR Gold staining makes the stands visible in gel. The results are shown in **Fig. 4.12**. Compared with the control (most right lane), showing the position of full-length **DNA17** and **DNA18** (51 nt), two cleavage-product bands are observed, suggesting external **xylitol-NBP** can induce oxidation damage to dsDNA with the irradiation. The cleavage yield was calculated by analyzing fluorescent intensity of each band. As can be seen, in the case of 1 eq. PNA invasion solution, the cleavage yield of product 1 and 2 are 12.9% and 8.6%, respectively. However, when 100 eq. PNA is present in the invasion solution, the cleavage yield of product 1 and 2 sharply decrease to 0.9% and 1.2%. This result indicates the PNA's self-aggregation and nonspecific interaction with dsDNA hamper the photooxidation by **xylitol-NBP** as Gs in DNA are inaccessible for $^1O_2$.

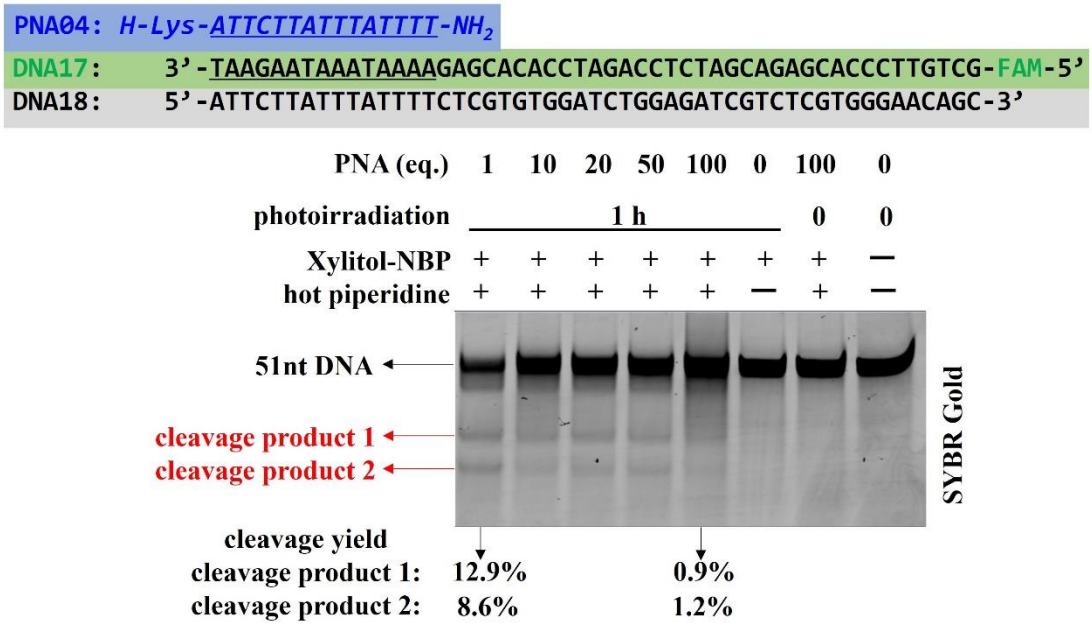

Fig. 4.12 Effect of PNA self-aggregation on **xylitol-NBP**-induced dsDNA photodamage. Condition: 40-nM dsDNA (1 eq.), unmodifeied-PNA (0–100 eq.), 4-μM **xylitol-NBP** in 10 mM sodium phosphate buffer with 0 mM NaCl pH 7.0, incubated at 37 ºC overnight. 365-nm light, at 37 ºC for 0 min or 1 h. Cleavage with 1-M piperidine in H_2O, 95 ºC for 45 min. 20% denaturing PAGE (7-M urea) and electrophoresed at 200 V. The pictures containing the whole gel image are presented in Experimental **Fig S26**.

4.5 SUMMARY

This chapter investigates the end-invasion of NBP-PNA conjugate into dsDNA and effect of PNA's self-aggregation and nonspecific interaction with dsDNA on photooxidation. Section 1 is the introduction of this chapter, including several attempts to enhance the invasion efficiency of PNA. Then Section 2 tested the end-invasion of NBP-PNA in dsDNA using two types of dsDNA models. The mixed-AT dsDNA (**DNA13**/**DNA16**) contained several A-tract in FAM-labeled strand **DNA13**. The polyT sequence in NBP-PNA readily bound to **DNA13** and dissociated DNA duplex as the new and wide bands appeared in FAM image assigned to $(PNA)_n$-**DNA13** complex and single-strand **DNA16** was detected by SYBR Gold staining. The other dsDNA model is mixed-ATCG sequence, the formation of end-invasion complex of NBP-PNA/dsDNA was inferred from two observations: a new retard band, and the amount of ssDNA did not increase. This data verifies the addition of NBP did not hamper the invasion of PNA. Section 3 discussed the photooxidation of NBP-PNA/dsDNA invasion complex. No cleavage product was observed after 1-h irradiation and hot-piperidine treatment. It seemed that the NBP-PNA tended to self-aggregate and bound to DNA non-specifically. Section 4 investigated the effect of PNA self-assembly and interaction with DNA on photooxidation. The photoxidation experiments of unmodified-PNA/dsDNA invasion complex with different PNA amount by external **xylitol-NBP** suggested the PNA's self-aggregation and nonspecific interaction with dsDNA hamper the photooxidation.

The results presented in this chapter show that the corporation of NBP would not block the invasion of PNA oligomer. However, the photooxidation of NBP was severely hampered. This inhibition probably is related to self-aggregation of PNA and non-specifically binding to dsDNA. Other factors would also affect the photooxidation as the PNA invasion has not been completely understood. Based on the findings obtained in this chapter, further work is required to ensure that NBP-PNA conjugates can effectively insert into dsDNA at low concentration.

Chapter 5: Summary

The aim of this study is to develop an alternative photo-knockout approach to overcome the limitations of unnecessary immune response caused by large nuclease in CRISPR-Cas9 system. To achieve this goal, a small-molecule method is proposed to produce targeted genome DNA cleavage via site-selective photooxidation of guanine (G). This lesion is mediated by nitrobiphenyl photosensitizer (NBP)-peptide nucleic acids (PNA) conjugates. The specificity of this photo-induced DNA cleavage method relies on two factors: the site-specific invasion of PNA into dsDNA and limited-range oxidation of G by singlet oxygen ($^1O_2$) generated from NBP.

Chapter 1 is the introduction of this thesis, including the abstract, the background information and the purpose. Section 1 is the abstract of this thesis. Then section 2 summarizes the related literature, including: 1. major DNA cleavage techniques used for gene editing, especially the CRISPR-Cas9 system as well as recently proposed photo-knockout techniques, and the drawbacks of proteins in these systems, 2. formation of single-strand breaks (SSBs) in DNA through oxidative damage mechanism, 3. examples of selective photooxidation of DNA by oligonucleotides-photosensitizer conjugates, in particular NBP-DNA which induces distance-dependent photooxidation of G by $^1O_2$. Section 3 describes the design of this thesis work. To prevent the immune system attacking nucleases, this thesis explores the potential of a small molecule DNA scissor, NBP-PNA conjugate for dsDNA photo-knockout.

Chapter 2 is concerned with the synthesis of NBP-modified PNAs and their binding characteristics to ssDNA. Section 1 is the introduction of this chapter, including the previous study of distance-dependent photooxidation of NBP-DNA conjugate. In section 2, the novel **NBP-thymine-PNA** (**NBP-T-PNA**, **Fig. 5.1**) monomer is designed and synthesized through an 8-step synthesis routine, including Sonogashira coupling and Mitsunobu coupling to attach the NBP group to the α-methyl position of T. In section 3, the conditions of coupling reaction in Fmoc-based solid-phase synthesis are carefully screened for the synthesis of designed 15mer PNA. Then six PNA oligomers with a hydrophilic lysine at the N-terminus, are synthesized using the optimized protocol. In section 4, thermal denaturation measurements (T_m) and CD spectroscopy of the NBP-conjugated-PNA/DNA and unmodified PNA/DNA duplexes are measured and compared. The T_m values show modest differences between NBP-conjugated-PNA/DNA (44.4 °C) and unmodified PNA/DNA duplexes (46.1 °C), and their CD spectra have two similar absorption bands (220 and 260-270 nm), suggesting that incorporation of NBP in PNA did not cause any significant structural deviations from the right-handed helix.

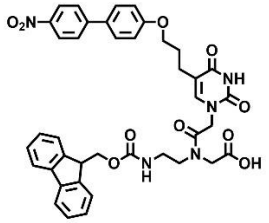

Fig. 5.1 NBP-thymine-PNA (NBP-T-PNA) monomer.

Chapter 3 describes the photooxidation characteristics of NBP-PNA in ssDNA and dsDNA. Section 1 is the introduction of this chapter, including some examples of oligonucleotide conjugates for inducing oxidative damage to DNA and the oxidation of G by $^1O_2$. In section 2, the $^1O_2$ production ability of NBP-PNA is confirmed by monitoring furfuryl alcohol via HPLC. The consumption of this typical $^1O_2$-probe molecule after 10-min irradiation with two NBP-PNA/DNA duplexes are both as large as that in the case of dsDNA. In section 3, an experimental system is constructed to quantitatively investigate the photooxidation efficiency of conjugated NBP and external **xylitol-NBP**, in the context of PNA/DNA duplex and dsDNA. Quantitative analysis by RP-HPLC revealed that the efficiencies of G photooxidation in three NBP-PNA/DNA duplexes were 4.2%, 2.5% and 2.4%, significantly lower than those in corresponding NBP-DNA/DNA duplexes (62%, 6.7% and 9.4%). This suppression effect is also observed with external **xylitol-NBP** and the G photooxidation efficiency in unmodified-PNA/DNA was 28.9%, obviously lower than that of dsDNA 72.5%. What's more, the external NBP has much better photooxidation efficiency than NBP-PNA conjugates. And it is also found that the placements of the abasic site in PNA strand around G, resulting in much space around G, yield higher photooxidation efficiencies (4.5%, 9.2%, 3.2%) than the fully matched NBP-PNA/DNA (2.5%). Finally, two hypotheses were presented in this section to explain the observations: 1. the base stacking within PNA/DNA duplex reduces accessibility to G, therefore preventing the $^1O_2$ oxidation, 2. $^1O_2$ produced from NBP-PNA is likely quenched by amide bond during diffusion along the PNA/DNA backbone. In section 4, gel electrophoresis experiments demonstrated that when complexed with the sticky end of a dsDNA, NBP-PNA conjugate was able to photooxidize G only in the dsDNA region, (illustrated by **Fig. 5.2**) while the NBP-DNA can also photooxidize G in the sticky end region. NBP-PNA binds to the sticky end of a dsDNA, where two Gs are designed to be under different context: one hybridizes with PNA, while the other in the DNA duplex region. In short words, the results obtained from this chapter illustrate that NBP-PNA conjugates is a potential tool for site-selective photooxidation of dsDNA as it is able to photooxidize G only in the dsDNA region when complexed with the sticky end of a dsDNA.

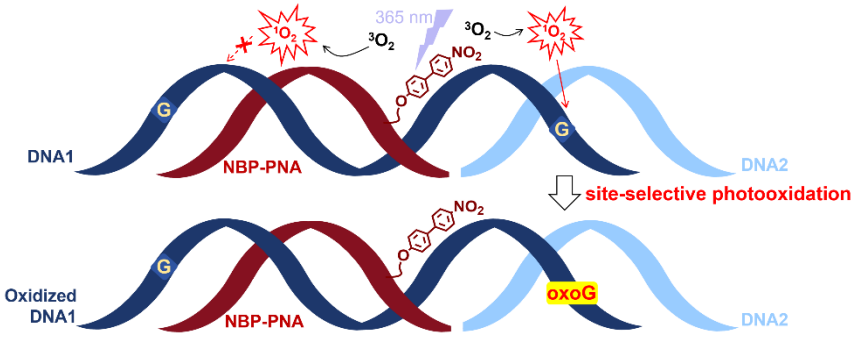

Fig 5.2 Illustration of site-selective photooxidation of NBP-PNA conjugate.

Chapter 4 investigates the invasion of NBP-PNA into dsDNA and the effect of PNA self-aggregation on photooxidation. Section 1 is the introduction of this chapter, including some strategies for enhancement of the PNA invasion. Section 2 describes

the end-invasion of NBP-PNA into two dsDNA models, mixed-AT or mixed-ATCG sequences analyzed by non-denaturing gel electrophoresis. The mixed-AT dsDNA (**DNA13**/**DNA16**) contained several A-tract in FAM-labeled strand **DNA13**. The polyT sequence in NBP-PNA readily bound to **DNA13** and dissociated DNA duplex as the new and wide bands appeared in FAM image assigned to PNA-**DNA13**-PNA complex and single-strand **DNA16** was detected by SYBR Gold staining. The other dsDNA model is mixed-ATCG sequence, the formation of end-invasion complex of NBP-PNA/dsDNA was inferred from two observations: a new retard band, and the amount of ssNDA did not increase. That data verifies that the addition of NBP did not hamper the invasion of PNA. Section 3 discussed the photooxidation of NBP-PNA/dsDNA invasion complex. No cleavage product was observed after 1-h irradiation and hot-piperidine treatment. It seemed that the NBP-PNA tended to be self-aggregate and bound to DNA non-specifically. Section 4 investigated the effect of PNA self-assembly and interaction with DNA on photooxidation. The photoxidation experiments of unmodified-PNA/dsDNA invasion complex with different PNA amount by external xylitol-NBP suggested the PNA's self-aggregation and nonspecific interaction with dsDNA hamper the photooxidation.

Overall, the theme of this thesis was the design and synthesis of NBP-modified PNAs and the investigation of their photooxidation characteristics in ssDNA and dsDNA. The type II photosensitizer NBP is attached to nucleobase T via a short ethylene linker at the α-methyl position, and the incorporation of NBP in PNA does not cause any significant structural deviations from the right-handed PNA/DNA helix nor hinder PNA invasion into dsDNA. As the PNA complexed with DNA suppressed G oxidation, NBP-PNA bounded with the sticky end of a dsDNA can exclusively induce oxidative damage to G only in the dsDNA region. It is also found that the self-aggregator of PNA non-specifically interacts with dsDNA and considerably inhibits the oxidation of DNA. It is hoped that this thesis will pave the way for next-generation NBP-PNA conjugates with enhanced invasion efficiency at low concentrations and exceptional specificity in targeting G oxidation. Ultimately, this site-specific photooxidation approach using NBP-PNA conjugates could advance the exploration of oxo-G's biological roles and expand the toolkit for precise gene editing.

Experimental part

Synthesis

General methods

All chemicals and reagents were commercially available and used without further purification. Water used for the organic synthesis was purified by Milli-Q, Merck Millipore. Thin-layer chromatography (TLC) was performed on pre-coated silica gel Merck 60-F 254 plates and visualized by the UV light (AS ONE SLUV-6, 254 or 365 nm) or charring after immersing in a solution of 1% $Ce(SO_4)_2$·1.5% $(NH_4)_6Mo_7O_{24}$·$4H_2O$ in 10% H_2SO_4. Column chromatography was performed on Wako gel C-200, Kanto silica gel 60N (spherical, neutral) or Biotage Sfär HC D, or Fuji Silysia NH silica gel (NH-DM1020) with the solvent system specified. ^{1}H NMR spectra were recorded at 400 MHz (JEOL JNM-ECZL400S) or 500 MHz (Varian Unity INOVA 500 or Bruker AVANCEIII HD 500). The tetramethylsilane peak (δ = 0.00 ppm) or a solvent peak was used as a standard in $CDCl_3$ (δ = 7.26 ppm) or $(CD_3)_2SO$ (δ = 2.50 ppm). Chemical shifts are expressed in ppm referenced to the standards. The multiplicity of the signals is abbreviated as follows: s = singlet, d = doublet, dd = doublet of doublets, t = triplet, q = quartet, br = broad signal and m = multiplet. ^{13}C NMR spectra were recorded at 101 MHz (JNM-ECZL400S) and a solvent peak of $CDCl_3$ (δ = 77.16 ppm) or $(CD_3)_2SO$ (δ = 39.52 ppm) was used as a standard. High-resolution mass spectra (HRMS) were recorded on a Bruker micrOTOF II ESI-TOF MS.

PNA04 was purchased from HLB Panagene, DNA02, DNA03, DNA05, DNA06, DNA08- DNA18 oligomers, 38nt and 56nt DNA marker (3'-phosphorylation) were purchased from Integrated DNA Technologies. These oligomers were directly dissolved in water without further purification and stored at 4 °C. Electrophoresis grade acrylamide solution was purchased from Nacalai Tesque.

Synthetic protocols

Synthesis of 2-3[143]

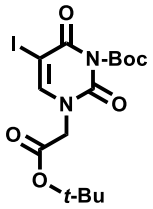

2-3

To a suspension of iodouracil (**2-1**, 7.00 g, 29.4 mmol) and K_2CO_3 (4.47 g, 32.4 mmol) in anhydrous DMF (58 mL), tert-butylbromoacetate (4.34 mL, 29.4 mmol) in anhydrous DMF (5 mL) was added dropwise at 0 °C. The resulting reaction mixture was warmed to r.t. and vigorously stirred under N_2 overnight. The precipitate was filtered and washed with methanol. The filtrate was collected and solvent was removed off in vacuo and the residue was subjected to short column (60N gel, hexane-EtOAc= 1:1, R_f =0.43) to give compound **2-2** (8.16 g, 80%) as white solid. ^{1}H NMR (500 MHz, DMSO-d_6) δ 11.77 (s, 1H), 8.19 (s, 1H), 4.38 (s, 2H), 1.42 (s, 9H). The obtained compound **2-2** was identical with the reported compound in regard to the analytical data.[144] To a suspension of compound **2-2** (5.50 g, 15.6 mmol) and 4-dimethylaminopyridine (DMAP) (0.19 g, 1.56 mmol) in anhydrous pyridine (50 mL), di-*tert*-butyl Pyrocarbonate (Boc_2O) (8.97 mL, 39.1 mmol) was added at r.t.. The resulting reaction mixture was stirred under N_2 for 2-h. 10-mL water was added to quench Boc_2O. The solvent was removed off in vacuo and the residue was subjected to short column (60N gel, hexane-EtOAc = 4:1, R_f = 0.23) to give compound **2-3** (5.88 g, 84%) as yellow solid. ^{1}H NMR (400 MHz, $CDCl_3$) δ 7.56 (s, 1H), 4.37 (s, 2H), 1.59 (s, 9H), 1.48 (s, 9H). ^{13}C NMR (101 MHz, $CDCl_3$) δ 165.90, 157.96, 148.71, 148.28, 146.85, 87.62, 84.17, 67.51, 49.52, 28.12, 27.49. ESI-TOF-MS calcd. for $C_{15}H_{21}IN_2O_6Na^+$ $[M+Na]^+$ 475.0337; found 475.0333.

Synthesis of 2-4[74]

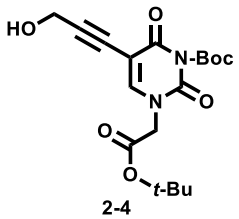

2-4

Compound **2-3** (1.84 g, 4.07 mmol), propargyl alcohol (0.72 mL, 12.2 mmol), $Pd[P(Ph)_3)_4$ (0.47 g, 0.41 mmol) and CuI (0.23 g, 1.22 mmol) were added to a deoxygenated solution of Et_3N (1.13 mL, 8.13 mmol) and THF (20 mL). The resulting reaction mixture was stirred under N_2 for 4 h. To the mixture was added 300-mL water and it was then extracted with EtOAc (3×300 mL). The organic layer was washed with

saturated aqueous water (300 mL) and brine (300 mL). After the organic layer was dried over anhydrous Na_2SO_4, the mixture was evaporated and purified by column chromatography (60N gel, hexane-EtOAc = 1:1, R_f =0.30) to give compound **2-4** (0.88 g, 57%) as pale yellow solid. ^{1}H NMR (400 MHz, $CDCl_3$) δ 7.39 (s, 1H), 4.43 (d, J = 5.3 Hz, 2H), 4.38 (s, 2H), 1.59 (s, 9H), 1.48 (s, 9H). ^{13}C NMR (101 MHz, $CDCl_3$) δ 165.80, 159.59, 148.04, 146.90, 146.74, 99.59, 92.97, 87.62, 84.20, 75.67, 51.60, 49.73, 28.12, 27.52. ESI-TOF-MS calcd. for $C_{18}H_{24}N_2O_7Na^+$ $[M+Na]^+$ 403.1476; found 403.1476.

Synthesis of 2-5

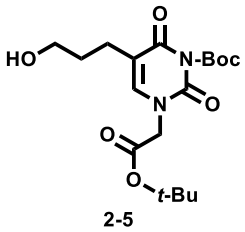

2-5

To a 500-mL round-bottom flask was added compound **4** (800 mg), the air in the flask was replaced with N_2, and then EtOAc (30 mL) and 10% Pd/C (336 mg) were added. The N_2 gas in the flask was replaced with H_2 and the hydrogenation reaction was carried out for overnight at room temperature. After replacing the H_2 gas in the flask with N_2, the mixture was filtered to remove Pd/C. The solvent was removed in vacuo and the residue was purified by column chromatography (60N gel, CH_2Cl_2-MeOH = 20:1, R_f = 0.35) to give compound **5** (0.58 g, 72%) as pale-yellow solid. ^{1}H (400 MHz, $CDCl_3$) δ 6.99 (s, 1H), 4.32 (s, 2H), 3.58 (t, J = 6.1 Hz, 2H), 2.41 (t, J = 7.1 Hz, 2H), 1.75–1.68 (m, 2H), 1.55 (s, 9H), 1.43 (s, 9H). ^{13}C NMR (101 MHz, $CDCl_3$) δ 166.40, 161.80, 148.88, 147.80, 140.90, 113.84, 86.93, 83.60, 61.04, 49.30, 31.42, 28.02, 27.44, 23.01. ESI-TOF-MS calcd. for $C_{18}H_{28}N_2O_7Na^+$ $[M+Na]^+$ 407.1789; found 407.1781.

Synthesis of 2-6[75]

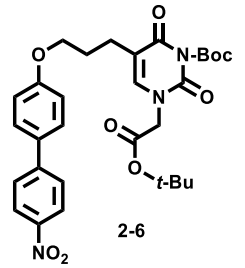

2-6

To a 100-mL flask was added **2-5** (358 mg, 0.93 mmol), 4'-nitro-[1,1'-biphenyl]-4-ol (301 mg, 1.39 mmol), PPh_3 (366 mg, 1.39mmol) and dry THF (12 mL), and then the mixture was heated to 50 ºC under N_2 atmosphere. To the mixture was dropped diisopropyl azodicarboxylate (DIAD) (0.274 mL, 1.39 mmol). The resulting reaction mixture was stirred at 50 ºC under N_2 for 3 h. To the reaction mixture was added 100-

mL water, and the mixture was extracted with CH_2Cl_2 (3×100 mL). The organic layer was washed with saturated $NaHCO_3$ aqueous solution (100 mL) and brine (100 mL). After the organic layer was dried over anhydrous Na_2SO_4, the mixture was evaporated and purified by column chromatography (NH-DM 1020 gel, hexane-EtOAc = 2:1, R_f = 0.30) to give compound **2-6** (295 mg, 55%) as yellow solid. ^{1}H NMR (400 MHz, $CDCl_3$) δ 8.27 (t, J = 2.5 Hz, 1H), 8.24 (t, J = 2.1 Hz, 1H), 7.68 (t, J = 2.5 Hz, 1H), 7.66 (t, J = 2.2 Hz, 1H), 7.56 (t, J = 3.0 Hz, 1H), 7.54 (t, J = 2.2 Hz, 1H), 7.00 (t, J = 3.1 Hz, 1H), 6.98 (t, J = 2.3 Hz, 1H), 6.96 (s, 1H), 4.33 (s, 2H), 4.04 (t, J = 6.0 Hz, 2H), 2.57 (t, J = 6.5 Hz, 2H), 2.10–2.03 (m, 2H), 1.61 (s, 9H), 1.44 (s, 9H). ^{13}C NMR (101 MHz, $CDCl_3$) δ 166.39, 161.32, 159.86, 148.98, 147.86, 147.28, 146.60, 140.55, 131.13, 128.68, 127.14, 124.27, 115.22, 113.58, 87.01, 83.69, 66.87, 49.18, 28.08, 27.78, 27.54, 23.98. ESI-TOF-MS calcd. for $C_{30}H_{35}N_3O_9Na^+$ $[M+Na]^+$ 604.2266; found 604.2259.

Synthesis of 2-7[144]

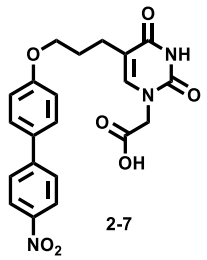

2-7

Compound **2-6** (280 mg, 0.48mmol) and triisopropylsilane (TIS) (0.10 mL, 0.48mmol) were dissolved in CH_2Cl_2 (3 mL), and trifluoroacetic acid (TFA) (3 mL) was added dropwise at 0 °C. The reaction mixture was then warmed to r.t. and stirred for 4-h. To the reaction mixture, 2-mL toluene was added, and then all the solvents were evaporated. Compound **2-7** was obtained as yellow solid (0.241 g). Without further purification, the product was used in next reaction. ^{1}H NMR (400 MHz, DMSO-d_6) δ 11.39 (s, 1H), 8.27 (d, J = 8.2 Hz, 2H), 7.92 (d, J = 8.4 Hz, 2H), 7.75 (d, J = 8.9 Hz, 2H), 7.54 (s, 1H), 7.08 (d, J = 8.9 Hz, 2H), 4.38 (s, 2H), 4.06 (t, J =6.3 Hz, 2H), 2.36 (t, J = 6.9 Hz, 2H), 1.95–1.88 (m, 2H). ^{13}C NMR (101 MHz, DMSO-d_6) δ 169.71, 164.08, 159.59, 150.91, 146.35, 146.03, 142.19, 129.90, 128.63, 127.03, 124.17, 115.24, 111.85, 67.09, 48.53, 27.48, 22.91. ESI-TOF-MS calcd. for $C_{21}H_{18}N_3O_7^-$ $[M-H]^-$ 424.1145; found 424.1150.

Synthesis of 2-8

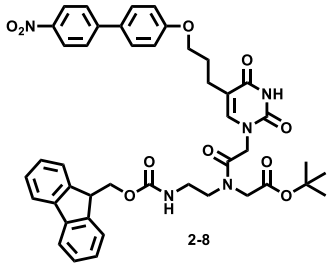

2-8

To a solution of compound **2-7** (198 mg, 0.46 mmol) and N,N-diisopropylethylamine (DIPEA) (162 μL, 0.93 mmol) in anhydrous DMF (4 mL) was added 1-[Bis(dimethylamino)methylene]-1H-benzotriazolium 3-Oxide Hexafluorophosphate (HBTU) (194 mg, 0.51 mmol) under nitrogen. After stirring for 30 minutes at room temperature, solid Fmoc-protected PNA backbone (HCl salt) (201 mg, 0.46 mmol) was added. The resulting solution was stirred overnight at r.t.. The solvent was evaporated and then reaction mixture was purified by column chromatography (HC D 20 μm gel, toluene-EtOAc = 1:4, R_f =0.35) to give compound **2-8** (146 mg, 47%) as pale-yellow solid. ^{1}H NMR (400 MHz, DMSO-d_6) δ 11.35 (s, 1H), 8.28–8.24 (m, 2H), 7.89 (t, J = 9.0 Hz, 4H), 7.72 (d, J = 8.9 Hz, 2H), 7.66 (t, J = 7.4 Hz, 2H), 7.43–7.26 (m, 6H), 7.05 (d, J = 8.9 Hz, 2H), 4.67 (s, 1H), 4.48 (t, J = 8.4 Hz, 1H), 4.31 (dd, J = 17.2, 7.1 Hz, 2H), 4.23–4.17 (m, 2H), 4.04–4.01 (m, 2H), 3.41–3.30 (m, 2H), 3.24 (q, J = 6.6 Hz, 1H), 3.10 (q, J = 6.2 Hz, 1H), 2.34 (t, J = 7.6 Hz, 2H),

1.94–1.85 (m, 2H), 1.44 (s, 3H), 1.37 (s, 6H). ^{13}C NMR (101 MHz, DMSO-d_6) δ 168.09, 167.32, 164.09, 159.57, 156.35, 150.91, 146.35, 146.01, 143.87, 140.78, 129.86, 128.97, 128.59, 127.66, 127.34, 127.10, 127.01, 125.15, 124.15, 124.13, 121.44, 120.19, 120.09, 115.22, 111.57, 81.97, 80.95, 67.03, 65.50, 46.74, 27.68, 27.63, 22.92. ESI-TOF-MS calcd. for $C_{44}H_{45}N_5O_{10}Na^+$ $[M+Na]^+$ 826.3059; found 826.3061.

Synthesis of NBP-T-PNA monomer

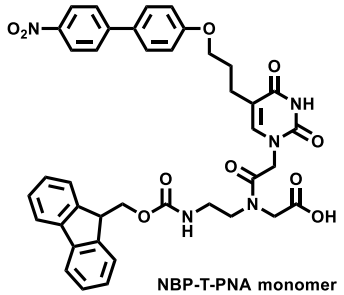

Compound **2-8** (130 mg, 0.16 mmol) and triisopropylsilane (TIS) (0.03 mL, 0.16mmol) were dissolved in CH_2Cl_2 (4 mL), and trifluoroacetic Acid (TFA) (6 mL) was added dropwise at 0 °C. The reaction mixture was then warmed to r.t. and stirred for 3 h. To the reaction mixture was added 2-mL toluene and solvent was evaporated. **NBP-T-PNA monomer** was obtained as pale-yellow solid (123.8 mg, quant). ^{1}H NMR (400 MHz, DMSO-d_6) δ 11.34 (d, J = 7.4 Hz, 1H), 8.28–8.24 (m, 2H), 7.92–7.87 (m, 4H), 7.73 (d, J = 8.9 Hz, 2H), 7.67 (t, J = 7.0 Hz, 2H), 7.46–7.27 (m, 6H), 7.05 (d, J = 8.9 Hz, 2H), 4.68 (s, 1H), 4.50 (s, 1H), 4.30 (dd, J = 18.1, 7.1 Hz, 2H), 4.23–4.20 (m, 2H), 4.03–4.00 (m, 3H), 3.34–3.31 (m, 1H), 3.25 (q, J = 6.5 Hz, 1H), 3.16 (s, 1H), 3.10 (q, J = 6.2 Hz, 1H), 2.34 (t, J = 7.7 Hz, 2H), 1.92–1.85 (m, 2H). ^{13}C NMR (101 MHz, DMSO-d_6) δ 164.11, 159.58, 150.94, 146.37, 146.02, 143.91, 140.78, 133.24, 132.10, 131.58, 131.49, 129.88, 128.89, 128.77, 128.60, 127.67, 127.12, 127.02, 125.18, 124.16, 121.28, 120.18, 115.24, 111.58, 84.25, 67.09, 65.56, 46.74, 44.93, 27.52, 23.68. ESI-TOF-MS calcd. for $C_{40}H_{36}N_5O_{10}^-$ $[M-H^+]^-$ 746.2462; found 746.2454.

Synthesis of Fmoc-protected PNA backbone

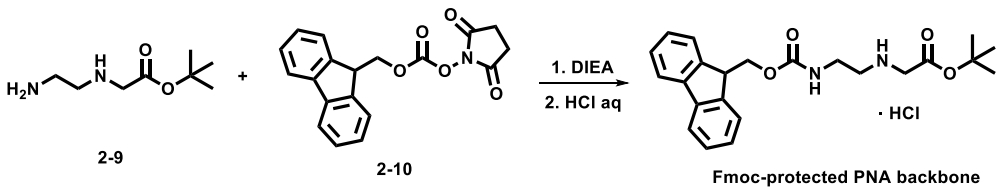

Compound **10** (5.14 g, 15.2 mmol) in 50-mL CH_2Cl_2 was added dropwise (> 1 h) under N_2 to a solution of **9**[145] (2.79 g, 16.3 mmol) and N,N-diisopropylethylamine (DIPEA) (2.79 mL, 16.3 mmol) in CH_2Cl_2 (60 mL). The resulting solution was stirred overnight at r.t.. The reaction mixture was washed with 1-M HCl (3×20mL) and brine solution (1×20mL). Then the organic layer was dried over Na_2SO_4 and filtered. The

filtrate was concentrated to about 5 mL and placed in −20 ºC for recrystallization. **Fmoc-protected PNA backbone** was obtained as white solid (2.1 g, 32%). ^{1}H NMR (400 MHz, $CDCl_3$) δ 7.73 (d, J = 7.3 Hz, 2H), 7.66 (d, J = 7.3 Hz, 2H), 7.36 (t, J = 7.4, 2H), 7.28 (td, J = 7.4, 1.3, 2H), 4.31 (d, J = 7.9 Hz, 2H), 4.21 (t, J = 6.8 Hz, 1H), 3.78 (s, 2H), 3.72 (q, J = 5.6 Hz, 2H), 3.28 (t, J = 5.5 Hz, 2H), 1.44 (s, 9H). ^{13}C NMR (101 MHz, $CDCl_3$) δ 164.89, 157.11, 144.03, 141.33, 127.77, 127.25, 125.64, 119.99, 84.93, 67.43, 48.97, 48.43, 47.15, 37.81, 28.09. The obtained compound was identical with the reported compound in regard to the analytical data.[77]

Synthesis of abasic PNA monomer

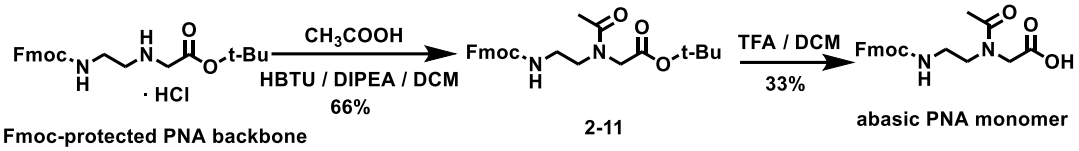

Fmoc-protected PNA backbone | 2-11 | abasic PNA monomer

To a suspension of acetic acid (43 μL, 0.76 mmol) in DMF (1.5 mL), DIPEA (264 μL, 1.51 mmol) and HBTU (328 mg, 0.86 mmol) were added. The reaction mixture was stirred at room temperature for 30 min. Then, to the reaction mixture, was added compound **Fmoc-protected PNA backbone** (298 mg, 0.75 mmol). The reaction mixture was stirred overnight. Then, the reaction mixture was diluted with CH_2Cl_2 and the organic layer was washed with water. After the organic layer was dried over anhydrous Na_2SO_4, the mixture was evaporated and purified by column chromatography (60N gel, CH_2Cl_2-MeOH = 30:1, R_f = 0.38) to give compound **2-11** (221 mg, 66%) as white solid. Obtained compound was subsequently disolved in CH_2Cl_2 and stirred at 0 °C. Then, the reaction mixture was warmed to r.t. and stirred for 30 min. To the reaction mixture, was added TFA (2 mL) and further stirred for 1 h. Then, to the reaction mixture, was added toluene (2 mL) and evaporated. The residue was dissolved in CH_2Cl_2 and Et_2O mixed solvent and placed in −20 °C for recrystallization. The compound **abasic PNA monomer** was obtained as white solid (109 mg, 33%). ^{1}H NMR (500 MHz, CD_3OD) δ 7.77 (d, J = 7.6 Hz, 1H), 7.64–7.59 (m, 2H), 7.37 (t, J = 7.4 Hz, 1H), 7.29 (t, J = 7.4 Hz, 1H) 4.40–4.30 (m, 2H) 4.26–4.15 (m, 1H), 4.14–3.99 (m, 2H), 3.49–3.41 (m, 2H), 3.28–3.23 (m, 2H), 2.11–1.94 (m, 3H). The obtained compound was identical with the reported compound in regard to the analytical data.[146]

Synthesis of 2-14

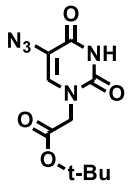

2-14

To a suspension of compound **5-azideuracil**[147] (152 mg, 1.00 mmol) and K_2CO_3 (138 mg, 1.00 mmol) in anhydrous DMF (10 mL), *tert*-butyl bromoacetate (133 μL, 0.90 mmol) in anhydrous DMF (5 mL) was added dropwise at 0 °C. The resulting reaction mixture was stirred at 0 °C under N_2 overnight. Then, to the reaction mixture, was added methanol (1 mL). The reaction mixture was concentrated, and the residue was suspended with CH_2Cl_2. The suspension was filtered, and the filtrate was concentrated. The residue was purified by column chromatography (60N gel, eluted with CH_2Cl_2) to give compound **2-14** (139 mg, 58%) as white solid. R_f =0.62 (CH_2Cl_2-methanol = 30:1). ^{1}H NMR (400 MHz, DMSO-d_6) δ 11.95 (br, 1H), 7.63 (s, 1H), 4.37

(s, 2H), 1.41(s, 9H). ^{13}C NMR (101 MHz, $CDCl_3$) δ 166.94, 160.39, 149.65, 133.86, 112.62, 82.05, 49.31, 27.68.

Synthesis of 2-15

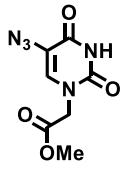

2-15

To a suspension of compound **5-azideuracil**[147] (406 mg, 2.65 mmol) and K_2CO_3 (370 mg, 2.68 mmol) in anhydrous DMF (30 mL), methyl bromoacetate (230 μL, 2.43 mmol) in anhydrous DMF (20 mL) was added dropwise at 0 °C. The resulting reaction mixture was stirred at 0 °C under N_2 for 3 h. Then, to the reaction mixture, was added methanol (1 mL). The reaction mixture was diluted with water and extracted with CH_2Cl_2. The water layer was acidified by HCl (~pH 6) and extracted with CH_2Cl_2. The organic layer was concentrated, and the residue was purified by column chromatography (60N gel, hexane-ethyl acetate = 1:1) to give compound **15** (181 mg, 33%) as pale yellow solid. R_f =0.45 (CH_2Cl_2-methanol = 25:1). ^{1}H NMR (500 MHz, DMSO-d_6) δ 12.01 (br, 1H), 7.63 (s, 1H), 4.49 (s, 2H), 3.69 (s, 3H). ^{13}C NMR (126 MHz, $CDCl_3$) δ 168.37, 160.32, 149.63, 133.62, 112.82, 52.39, 48.62.

Synthesis of 2-16

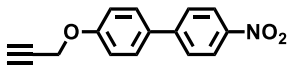

2-16

To a suspension of 4-hydroxy-4'-nitrobiphenyl (501 mg, 2.32 mmol) and K_2CO_3 (1.28 g, 9.29 mmol) in acetone (30 mL), was added dropwise propargyl bromide (0.24 mL, 2.79 mmol) in acetone (10mL) at room temperature. The reaction mixture was stirred under reflux condition overnight. Then, to the reaction mixture, was added methanol (1 mL). The reaction mixture was filtered and the filtrate was concentrated. The residue was purified by column (60N gel, hexane-EtOAc = 4:1, R_f = 0.44) to give compound **2-16** (560 mg, 95%) as yellow solid. ^{1}H NMR (400 MHz, DMSO-d_6) δ 8.28 (d, J = 8.9 Hz, 2H), 7.70 (d, J = 8.9 Hz, 2H), 7.60 (d, J = 8.8 Hz, 2H), 7.10 (d, J = 8.8 Hz, 2H), 4.77 (d, J = 2.4 Hz, 2H), 2.56 (s, 1H). ^{13}C NMR (101 MHz, $CDCl_3$) δ 158.41, 147.17, 146.79, 132.13, 128.74, 127.34, 124.31, 115.67, 78.27, 76.08, 55.99.

Synthesis of 2-17

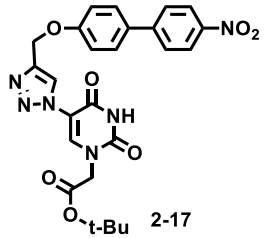

2-17

To the mixture of compound **2-14** (120 mg, 0.45 mmol), compound **2-16** (131 mg, 0.52 mmol), were added $CuSO_4 \cdot 5H_2O$ (17 mg, 0.068 mmol), and sodium ascorbate (32 mg, 0.16 mmol), were added DMF (5 mL) and H_2O (1 mL). The reaction mixture was stirred at room temperature under N_2 and dark condition overnight. Then, the reaction mixture was diluted with H_2O (50 mL), and the precipitate was filtrated. The precipitate was washed with hexane-CH_2Cl_2 (7:3, v/v) and filtered. The precipitate was dried to give compound **2-17**(188 mg, 81%) as yellow solid. R_f = 0.38 (CH_2Cl_2-methanol = 30:1). ^{1}H NMR (400 MHz, DMSO-d_6) δ 12.21 (s, 1H), 8.58 (s, 1H), 8.55 (s, 1H), 8.27 (d, J = 9.3 Hz, 2H), 7.94 (d, J = 9.2 Hz, 2H), 7.79 (d, J = 9.0 Hz, 2H), 7.23 (d, J = 9.2 Hz, 2H), 5.30 (s, 2H), 4.52 (s, 2H), 1.44 (s, 9H).

Synthesis of 2-18

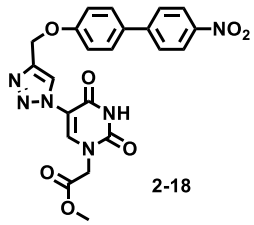

2-18

To a solution of compound **2-15** (114 mg, 0.50 mmol) and compound **2-16** (153 mg, 0.60 mmol) in DMF (3 mL), were added $CuSO_4 \cdot 5H_2O$ (24 mg, 0.094 mmol), sodium ascorbate (40 mg, 0.20 mmol), H_2O (1 mL) and DMF (2 mL). The reaction mixture was stirred at room temperature under N_2 and dark condition overnight. Then, the reaction mixture was diluted with H_2O (50 mL), and the precipitate was filtrated. The precipitate was suspended in CH_2Cl_2 and washed and filtered. The precipitate was dried to give compound **2-18** (216 mg, 90%) as yellow solid. R_f = 0.24 (CH_2Cl_2-methanol = 30:1). ^{1}H NMR (400 MHz, DMSO-d_6) δ 8.58 (s, 1H), 8.55 (s, 1H), 8.27 (d, J = 8.9 Hz, 2H), 7.94 (d, J = 8.9 Hz, 2H), 7.79 (d, J = 8.8 Hz, 2H), 7.23 (d, J = 8.9 Hz, 2H), 5.30 (s, 2H), 4.66 (s, 2H), 3.72 (s, 3H).

PNA oligomer synthesis and purification

Synthesis of PNA was carried out manually following a modified literature protocol[71,72,73] with NovaSyn TGR resin (Novabiochem) as a support, benzotriazole-1-yl-oxy-tris-pyrrolidino-phosphonium hexafluorophosphate (PyBOP) as an activator and Fmoc-PNA-A(Bhoc)-OH, Fmoc-PNA-C(Bhoc)-OH, Fmoc-PNA-T-OH (purchased from HLB Panagene) and NBP-T-PNA as monomers. Lysine was coupled to N-terminus of PNA using Fmoc-L-Lys(Boc)-OH (purchased from Watanabe chemical IND., LTD). Chain extension followed a three-step cycle:

(i) The Fmoc-protecting group was removed from the terminal amine with 20% piperidine in DMF at r.t. (2 min, 1 mL×2).

(ii) The next monomer (4 molar equivalents, compared to resin loading) of the Fmoc-PNA-C(Bhoc)-OH, Fmoc-PNA-T-OH or NBP-T-PNA) was coupled onto the N-terminus of the growing chain with PyBOP (4 molar equivalents) and 4-methylmorpholine (NMM) (8 molar equivalents) in anhydrous N-methyl-2-Pyrrolidone (NMP) at 40 ºC (1 h). For Fmoc-A(Bhoc)-OH, the concentration of all reactants as well as the duration of reaction was set doubled.

(iii) The unreacted amines were capped with acetic anhydride at r.t. for 5 min.

Finally, treatment of the solid resin with TFA/TIS/H_2O (38:1:1, v/v/v) mixture for 2 h resulted in simultaneous removal of the protecting groups and cleavage of the oligomers from the resin. The crude PNA samples were precipitated from anhydrous ether and purified by preparative HPLC system (Shimadzu) equipped with Waters X-bridge column (prep C18 5 μm, 10 × 250 mm). Method 1: elution buffer system: A buffer = H_2O/MeCN/TFA (98.5/1/0.1, v/v/v), B buffer = MeCN /H_2O/TFA (98.5/1/0.1, v/v/v). Flow rate of 3.0 mL/min with the following gradient system: A buffer with inclusion of 0–25% B buffer/0–10 min, 25% B buffer /10–40 min, 25–90% B buffer /40–50 min. Then, the purity of PNA was verified on an RP-HPLC system (Waters Alliance 2695) equipped with Waters X-bridge column (C18 5 μm, 4.6 × 150 mm).
Method 2: eluted buffer system: A buffer = H_2O/MeCN/TFA (98.5/1/0.1, v/v/v), B buffer = MeCN /H_2O/TFA (98.5/1/0.1, v/v/v). Flow rate of 1.0 mL/min with the following gradient system: A buffer with inclusion of 0–20% B buffer/0–10 min, 20% B buffer /10–30 min, 25–90% B buffer /30–50 min.

The two peaks observed in HPLC chart of **PNA01** (**Fig. 2.3**) were likely to derive from an identical compound in equilibrium, because the analysis of each peak by HPLC resulted in two peaks again (**Fig. S1**).

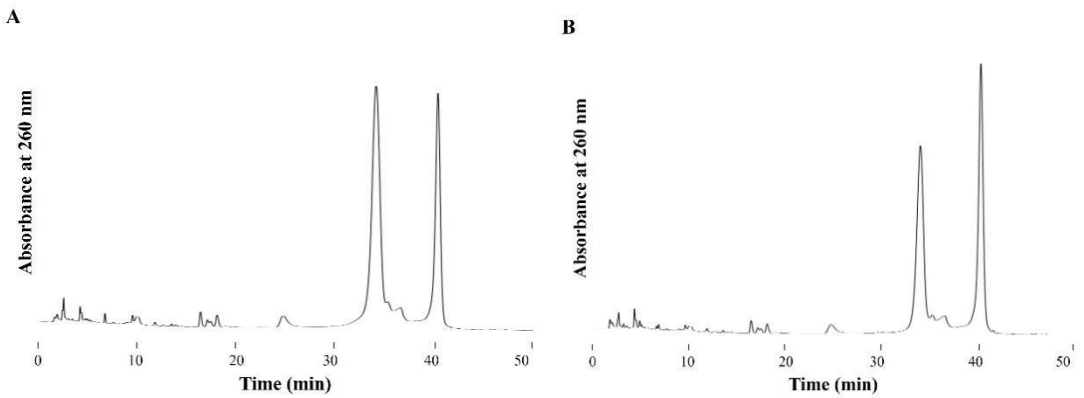

Fig. S1. Reversed-phase HPLC chromatographs of the two peaks of **PNA01** after separation. (A) the prior peak (RT = 35.0 min), (B) the latter peak (RT = 39.5 min)

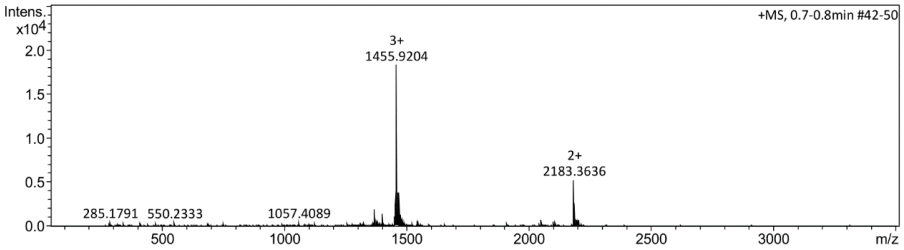

Fig. S2. ESI-TOF-MS spectra of **PNA01**, m/z calcd. for $C_{184}H_{236}N_{65}O_{63}$: 1455.6 $[M+3H]^{3+}$, found 1455.9.

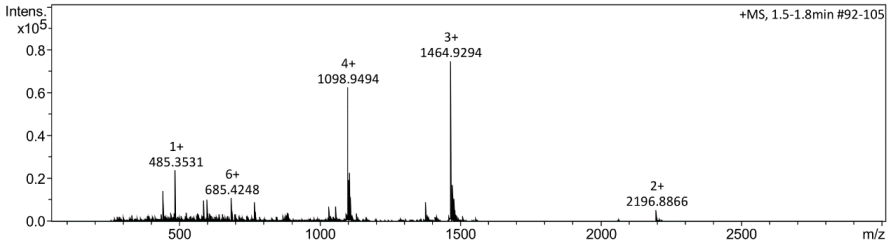

Fig. S3. ESI-TOF-MS spectra of **PNA02**, m/z calcd. for $C_{184}H_{232}N_{74}O_{57}$: 1464.6 $[M+3H]^{3+}$, found 1464.9.

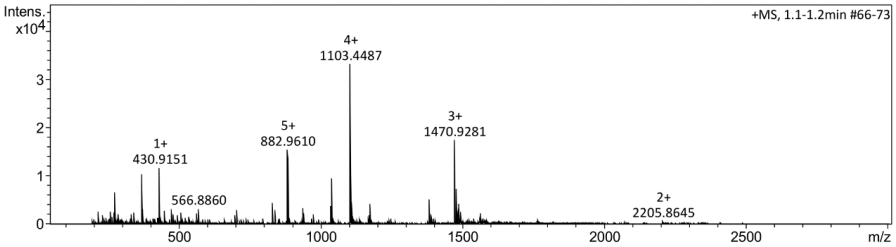

Fig. S4. ESI-TOF-MS spectra of **PNA03**, m/z calcd. for $C_{184}H_{230}N_{80}O_{53}$: 1470.6 $[M+3H]^{3+}$, found 1470.9.

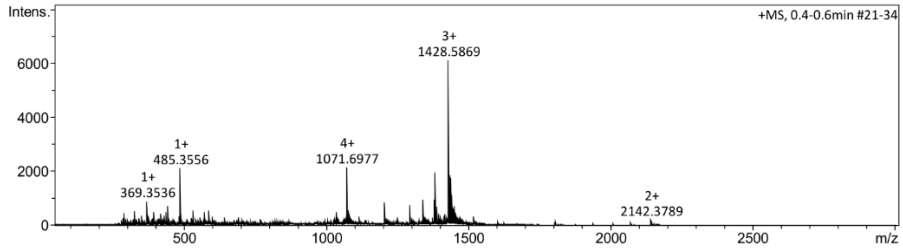

Fig. S5. ESI-TOF-MS spectra of **PNA04**, m/z calcd. for $C_{180}H_{229}N_{71}O_{56}$: 1428.3 $[M+3H]^{3+}$, found 1428.6.

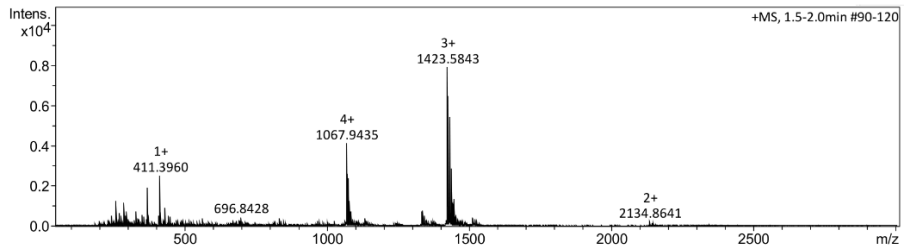

Fig. S6. ESI-TOF-MS spectra of **PNA05**, m/z calcd. for $C_{179}H_{228}N_{72}O_{55}$: 1423.3 $[M+3H]^{3+}$, found 1423.6.

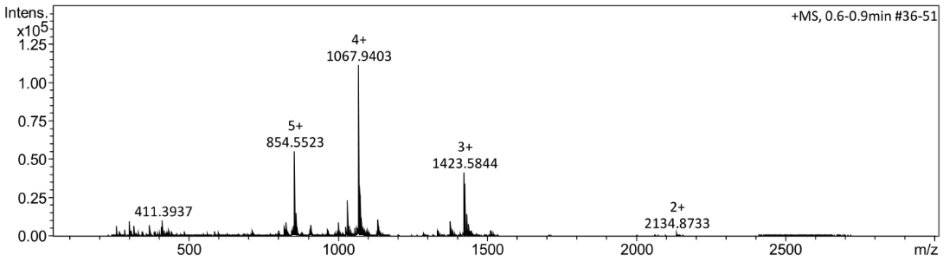

Fig. S7. ESI-TOF-MS spectra of **PNA06**, m/z calcd. for $C_{179}H_{228}N_{72}O_{55}$: 1423.3 $[M+3H]^{3+}$, found 1423.6.

NBP-DNAs synthesis and purification

NBP-DNA monomer and sequences were prepared according to the published procedures[9].

Table S1. The DNA oligomer sequences synthesized in this study and their mass analysis data.[a]

DNA	Sequence[b]	Molecular formula	m/z calcd. for $[M + 4e]^{4-}$	Found $[M + 4e]^{4-}$
DNA04	**5'-ATTATTATATTCTTATTTATPTTTT-3'**	$C_{263}H_{330}N_{70}O_{163}P_{24}$	1955.3	1954.6
DNA07	**5'-ATTCTTAAAATTPTT-3'**	$C_{163}H_{201}N_{47}O_{95}P_{14}$	1192.7	1192.0

[a] Obtained by ESI-TOF mass spectrometry.

[b] **P** = NBP-T unit.

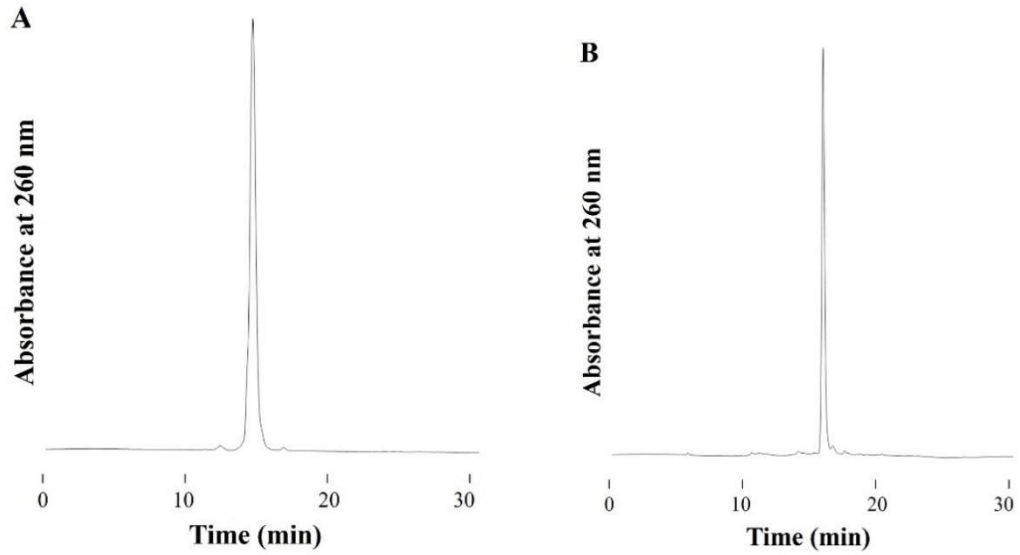

Fig. S8. Reversed-phase HPLC chromatographs of (A) **DNA04**, and (B)**DNA07**, after RP-HPLC purification.

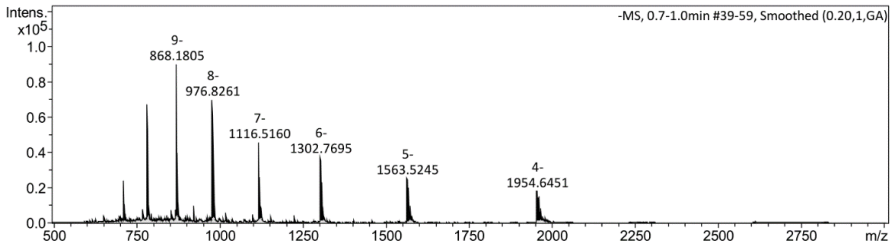

Fig. S9. ESI-TOF-MS spectra of **DNA04**, m/z calcd. for $C_{263}H_{330}N_{70}O_{163}P_{24}$: 1955.3 $[M+4e]^{4-}$, found 1954.6.

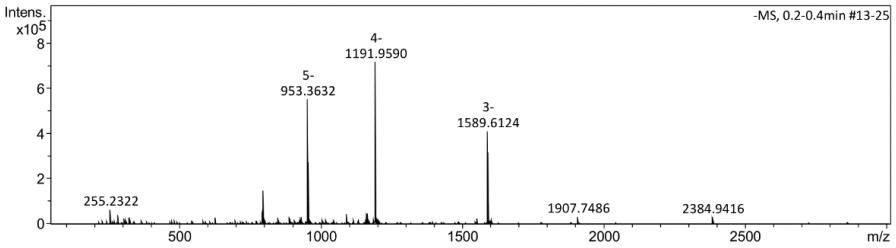

Fig. S10. ESI-TOF-MS spectra of **DNA07**, m/z calcd. for $C_{163}H_{201}N_{47}O_{95}P_{14}$: 1192.7 $[M+4e]^{4-}$, found 1192.0.

The concentrations were determined according to absorption intensity at 260 nm with a calculated[148] molar extinction coefficient value shown in **Table S2**.

Table S2. Molar absorption coefficients at 260 nm (ε_{260}) for ONs used in this study.

Strands	ε_{260} ($M^{-1}cm^{-1}$)
PNA01: *H-Lys-TTTCTTTTTTTTPTT-NH_2*	121200
PNA02: *H-Lys-ATTCTTATTTATPTT-NH_2*	139000
PNA07: *H-Lys-ATTCTTATTTATTTT-NH_2*	

PNA03: *H-Lys-ATTCTTAAAATTPTT-NH₂*	144800
DNA07: 5’-ATTCTTAAAATTPTT-3’	
DNA03: 5’-AAAAAAAAAAAGAAA-3’	182700
DNA04: 5’-ATTATTATATTCTTATTTATPTTTT-3’	237700
DNA09: 5’-ATTATTATATTCTTATTTATTTTTT-3’	
DNA05: 5’-AAAAAATAAATAAGAATATAATAAT-3’	288600
DNA06: 5’-AAAATAAATAAGAAT-3’	174300
DNA08: 5’-AAAAATTTTAAGAAT-3’	164500
DNA10: 5’-TTTTTTCTTTATATTTTATTATATTTTTATTTTTTTAATTTTTTT-3’	377000
DNA11: 5’-FAM-AAAAAAATTAAAAAAATAAAAATATAATAAAATATAAAGAAAAAAAA AATAAATAAGAAT-3’	477500
DNA12: 5’-AAAATTCTTTATATTTTATTATATTTTTATTTTTTTAATTTTTTT-3’	394700
DNA13: 5’-FAM-AAAAAAATTAAAAAAATAAAAATATAATAAAATATAAAGAATTTTAAAA TAAATAAGAAT-3’	463100
DNA14: 5’-AAAATTCTATATATTTTATTATATTTTTATTTTTTTAATTTTTTT-3’	400600
DNA15: 5’-FAM- AAAAAAATTAAAAAAATAAAAATATAATAAAATATATAGAATTTTAAAAATTTTAAGAAT-3’	475600
DNA16: 5’-ATTCTTATTTATTTTAAAATTCTTTATATTTTATTATATTTTTATTTTTTT AATTTTTTT-3’	93800
DNA17: 5’-FAM-GCTGTTCCCACGAGACGATCTCCAGATCCACACGAGAAAATAAATAAGAAT-3’	86400
DNA18:5’-ATTCTTATTTATTTTCTCGTGTGGATCTGGAGATCGTCTCGTGGGAACAGC-3’	86400
56nt DNA marker: 5’-FAM-AAAAAAATTAAAAAAATAAAAATATAATAAAATATA TAGAATTTTAAAAATTTTAA-3’	475600
38nt DNA marker: 5’-FAM-AAAAAAATTAAAAAAATAAAAATATAATAAAATATAAA-3’	442200
PNA04: *H-Lys-ATT_TTATTTATPTT-NH₂*	130800
PNA05: *H-Lys-AT_CTTATTTATPTT-NH₂*	132400
PNA06: *H-Lys-ATTC_TATTTATPTT-NH₂*	131800

UV-melting temperature measurements

A 2.0-μM solution of a duplex (180 μL) in 10-mM sodium phosphate buffer (pH 7.2) containing 100-mM NaCl was put into a quartz cell and sealed with a silicone cap. First, the solution was kept at 90 °C for 10 min and then cooled to 10 °C at a rate of 0.5 °C/min. Subsequently, the temperature was raised to 90 °C at the same rate, during which the UV absorbances at 260 nm were measured at every 1 °C by UV-Vis spectrophotometer (UV-1900i, Shimadzu). The absorbance values were plotted against temperature to afford a melting curve, which was then differentiated to give a differential curve. The melting temperature (T_m) was determined as the temperature

giving the maximum of the differential curve.

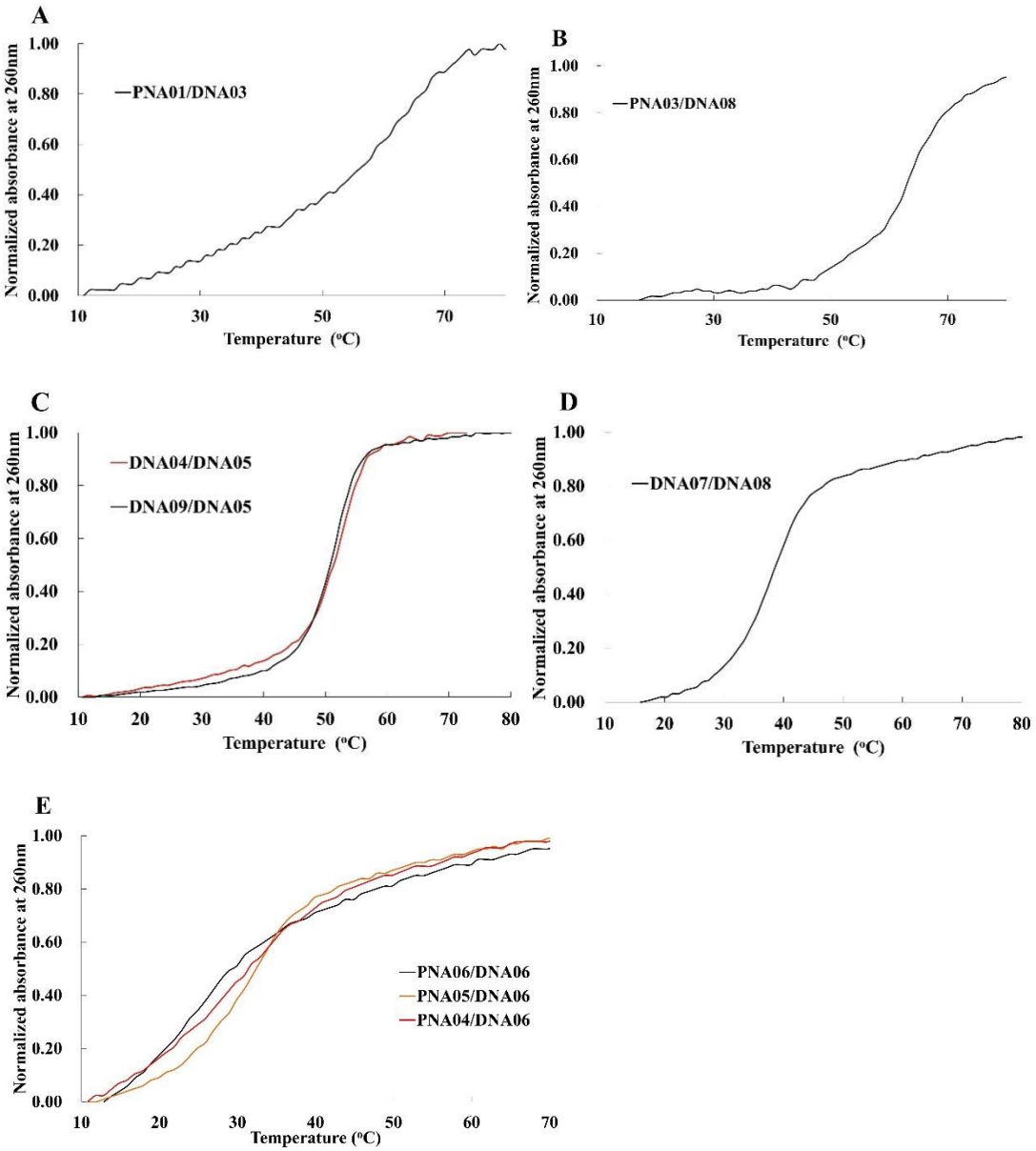

Fig. S11 UV-melting curves of duplexes. (A) **PNA01/DNA03**, (B) **PNA03/DNA08**, (C) **DNA04/DNA05** (red) and **DNA09/DNA05** (black), and (D) **DNA07/DNA08.** (E) **PNA04/DNA06** (red), **PNA05/DNA06** (orange) and **PNA06/DNA06** (black),.Conditions: 2.0-μM duplex; 10-mM sodium phosphate buffer (pH 7.2); 100-mM NaCl.

Circular dichroism (CD) spectra measurements

A 2.0-μM solution (2.0 mL) of a duplex in a buffer (10-mM sodium phosphate, 100-mM NaCl, pH7.2) was heated at 95 °C for 5 min and gradually cooled to room temperature. The solution was put into a cuvette (1 cm × 1 cm) and measured on a circular dichroism spectrometer (J-1100, JASCO) with the following condition: scan rage: 190-500 nm; scan speed: 500 nm/min; the number of scans: 10 times; temp 25 °C.

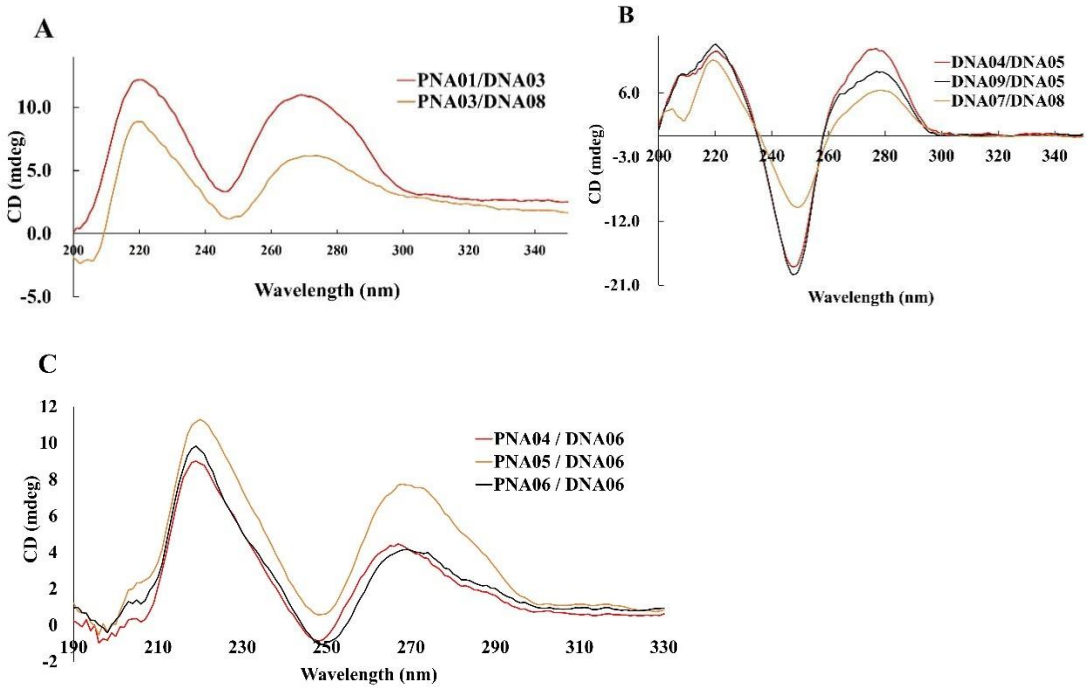

Fig. S12. CD spectra of duplexes. (A) **PNA01/DNA03** (red), and **PNA03/DNA08** (orange) (B) **DNA04/DNA05** (red) and **DNA09/DNA05** (black), and **DNA07/DNA08** (orange)**,** (C) **PNA04/DNA06** (red), **PNA05/DNA06** (orange) and **PNA06/DNA06** (black)Conditions: 2.0-µM duplex; 10-mM sodium phosphate buffer (pH 7.2); 100-mM NaCl, temp 25 °C.

Photooxidation, enzymatic digestion, and HPLC analysis

A 2.0-µM solution (100 µL) of a duplex in a buffer (10-mM sodium phosphate; 100-mM NaCl; pH 7.2) was placed into a 600-µL microtube. The microtube was placed into a heat block (NDC-100, NISSIN) and photoirradiated with a 365-nm LED (M365FP1, Thorlabs). The LED light was placed 1 mm above the microtube and irradiation was carried out with a light power of 42 mW/cm^2 at 20 °C for 0 or 10 min. To the resultant solution were added 12 µL of buffer (100-mM Tris-HCl (pH 8.0); 50-mM $MgCl_2$; 1-M KCl; 0.2% Triton X-100; 1-mg/mL BSA), 3-µL phosphodiesterase I (Worthington Biochemical Corporation, 0.5 U/µL), and 5-µL alkaline phosphatase (Thermo Scientific, 1 U/µL). The mixture was incubated at 47 °C for 3 h. Then, the reaction mixture was cooled on ice. To the mixture was added 2-µL EDTA (0.5 M) and the resulting mixture was heated at 90 °C for 1 min to inactivate the enzymes. Then, the mixture was cooled on ice and to it were added 13-µL distilled water and 15-µL riboflavin aqueous solution (as internal standard for the HPLC analysis). The mixture was centrifuged at 14000 rpm for 10 min at 4 °C. The supernatant was filtered (Millex-HV, 0.45 µm) and the filtrate was analyzed on a RP-HPLC system (Hitachi High-Tech, LaChrom Elite) equipped with a Waters X-bridge column (C18 5 µm, 4.6 × 150 mm) at 30 °C (column oven temp) at a flow rate of 1.0 mL/min with the following gradient system: 50-mM NH_4HCOOH with 0% MeCN/0–5 min, 0–9.5% MeCN /5–30 min, 9.5–24.5% MeCN /30–45 min, and 24.5–64.5% MeCN /45–60 min. The peak areas of dG,

dA, dT and dI (deoxyinosine generated from dA by a deaminase, which may be contaminated in the phosphodiesterase) [9] traced at 260 nm were used for quantification. Each peak area was divided by each ε value (ε_{260} dG: 11500, ε_{260} dA: 1540, ε_{260} dI: 7500) to estimate the concentration. The relative amounts (%) of dG obtained by 10-min photoirradiation were deduced from the following equation:

$dG = \{[dG]_{10}/([dA]_{10} + [dI]_{10})\}/\{[dG]_0/([dA]_0 + [dI]_0)\} \times 100$

where $[X]_n$ is the concentration of X after n-min photoirradiation.

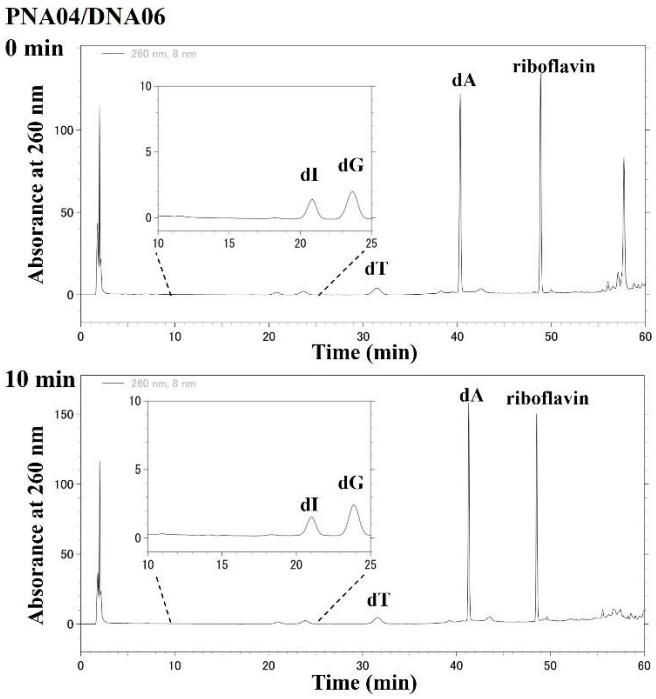

Fig. S13 RP-HPLC analysis of enzymatically digested products for **PNA04/DNA06**. The upper (no irradiation) and lower (10 min irradiation) chromatographs were recorded at 260 nm (dG, dA, dT and dI). Conditions: 2-μM duplex, 10-mM sodium phosphate buffer containing 100-mM NaCl, pH 7.2. Irradiated with 365-nm LED at 20 °C.

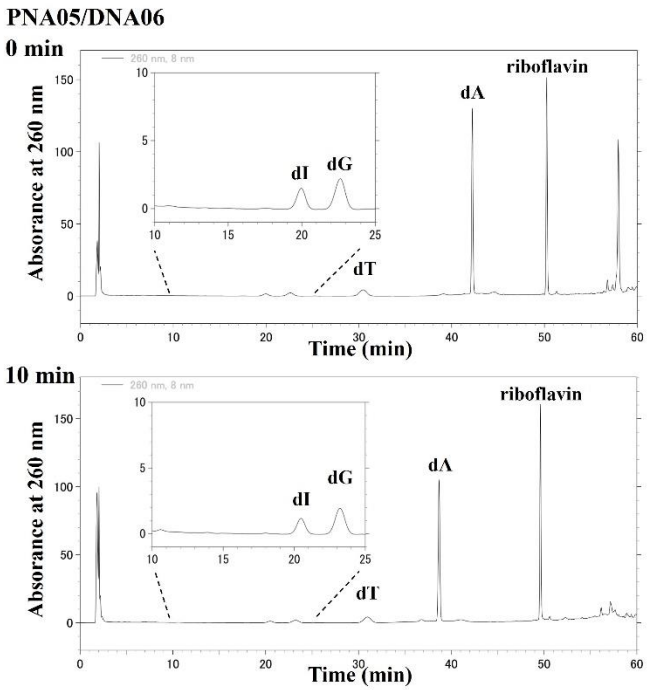

Fig. S14 RP-HPLC analysis of enzymatically digested products for **PNA05/DNA06**. The upper (no irradiation) and lower (10 min irradiation) chromatographs were recorded at 260 nm (dG, dA, dT and dI). Conditions: 2-μM duplex, 10-mM sodium phosphate buffer containing 100-mM NaCl, pH 7.2. Irradiated with 365-nm LED at 20 ºC.

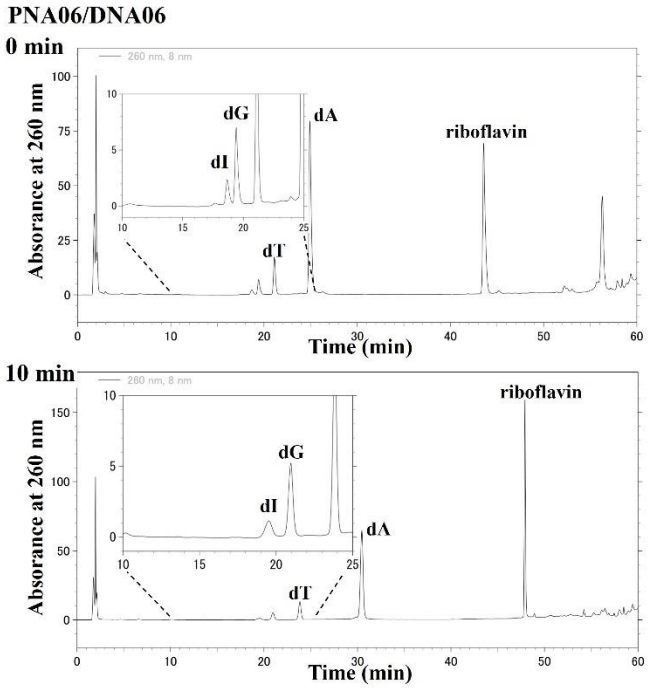

Fig. S15 RP-HPLC analysis of enzymatically digested products for **PNA06/DNA06**. The upper (no irradiation) and lower (10 min irradiation) chromatographs were recorded at 260 nm (dG, dA, dT and dI). Conditions: 2-μM duplex, 10-mM sodium phosphate buffer containing 100-mM NaCl, pH 7.2. Irradiated with 365-nm LED at 20 ºC.

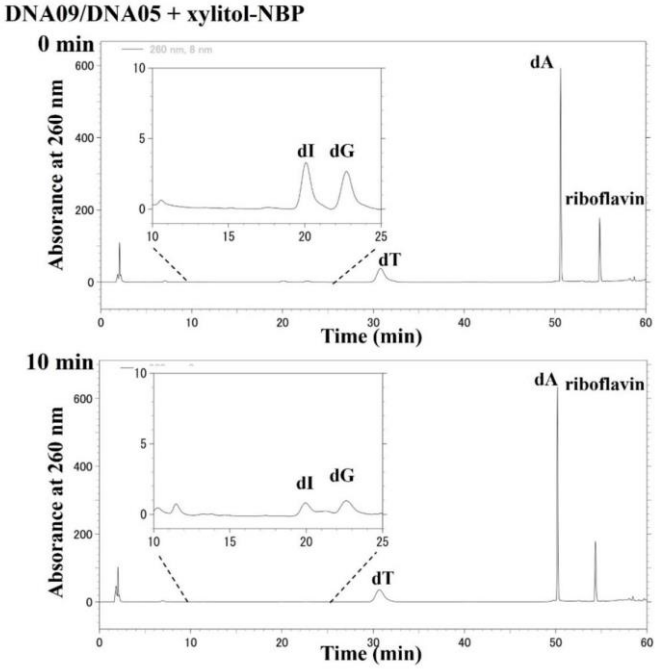

Fig. S16 RP-HPLC analysis of enzymatically digested products for **DNA09/DNA05 + xylitol-NBP**. The upper (no irradiation) and lower (10 min irradiation) chromatographs were recorded at 260 nm (dG, dA, dT and dI). Conditions: 2-μM duplex, 10-μM xylitol-NBP, 10-mM sodium phosphate buffer containing 100-mM NaCl, pH 7.2. Irradiated with 365-nm LED at 20 °C.

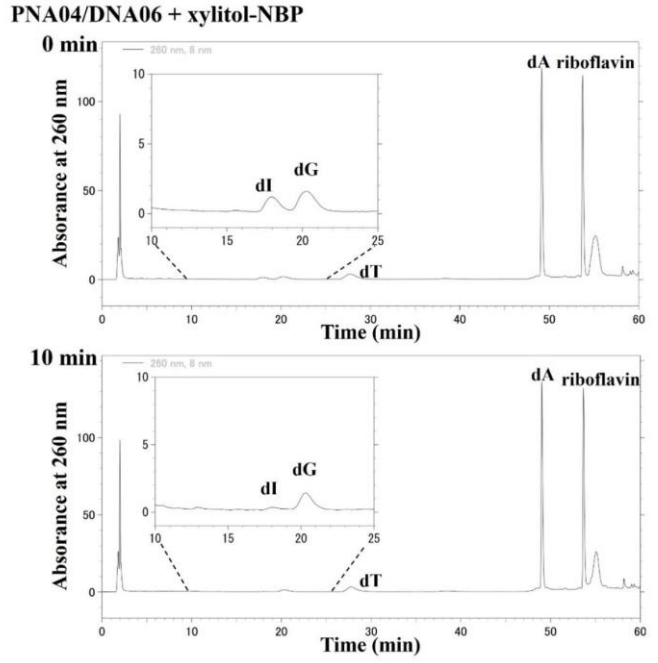

Fig. S17 RP-HPLC analysis of enzymatically digested products for **PNA04/DNA06 + xylitol-NBP**. The upper (no irradiation) and lower (10 min irradiation) chromatographs were recorded at 260 nm (dG, dA, dT and dI). Conditions: 2-μM duplex, 10-μM xylitol-NBP, 10-mM sodium phosphate buffer containing 100-mM NaCl, pH 7.2. Irradiated with 365-nm LED at 20 °C.

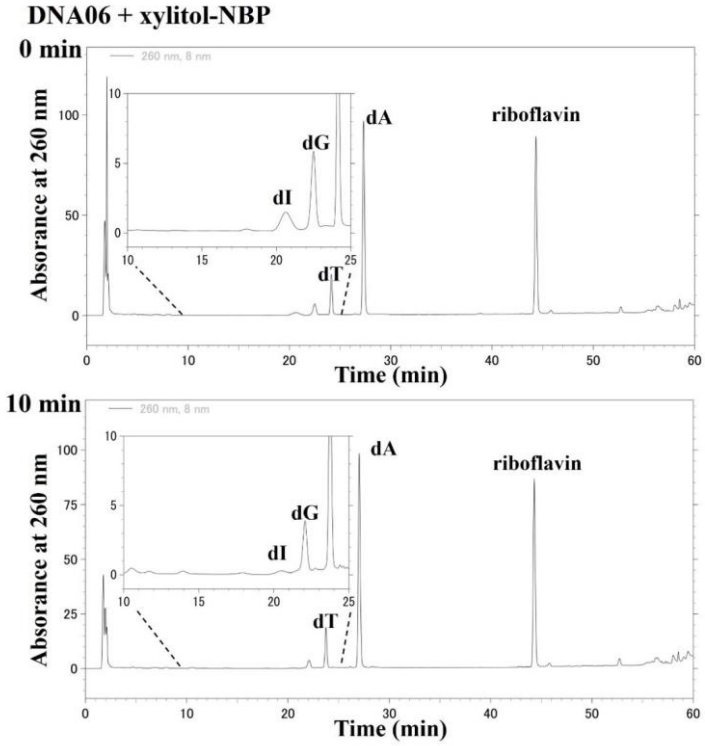

Fig. S18 RP-HPLC analysis of enzymatically digested products for **DNA06 + xylitol-NBP**. The upper (no irradiation) and lower (10 min irradiation) chromatographs were recorded at 260 nm (dG, dA, dT and dI). Conditions: 2-μM oligomer, 10-μM xylitol-NBP, 10-mM sodium phosphate buffer with 100-mM NaCl, pH 7.2. Irradiated with 365-nm LED at 20 °C.

$^1O_2$ production analysis of NBP-modified duplexes by furfuryl alcohol

A 4.0-μM solution (50 μL) of duplex in buffer was mixed with a 200-μM solution (50 μL) of furfuryl alcohol. The mixture was photoirradiated with 365-nm LED (42 mW/cm^2) at 20 °C for 10 min. Then, the solution was analyzed on an RP-HPLC system (Waters alliance) and the furfuryl alcohol peak area monitored at 216 nm was evaluated. The peak area of furfuryl alcohol without photoirradiation was set as 100%.

Site selective photooxidation of dsDNA with sticky end by NBP-PNAs

A 2.0-μM solution of duplex (100 μL) was irradiated for 10 min or 1 h in the same manner as mentioned above. The photoirradiation samples were treated through the following 2 kinds of methods.

1. Fpg cleavage: a 5-μL portion of the solution was taken and incubated at 37 °C in a supplied buffer containing Fpg (4, 8 or 12 units, purchased from New England BioLabs). After 2 h, the reaction was terminated by evaporation. Then, the samples

were dissolved in 5 μL of loading buffer and was loaded on a 20% denaturing PAGE (7-M urea) and electrophoresed at 200 V.

2. Piperidine cleavage: a 25-μL portion of the solution was taken and mixed with 1 M aq. piperidine (250 μL) and the resulting mixture was incubated for 45 min at 95 °C. The samples were evaporated to dryness and dissolved in 15 μL of loading buffer, then a 5-μL portion of the mixture was loaded on a 20% denaturing PAGE (7-M urea) and electrophoresed at 200 V.
   After the electrophoresis, the gel was scanned with a fluorescent image scanner (GE Typhoon FLA 9500).

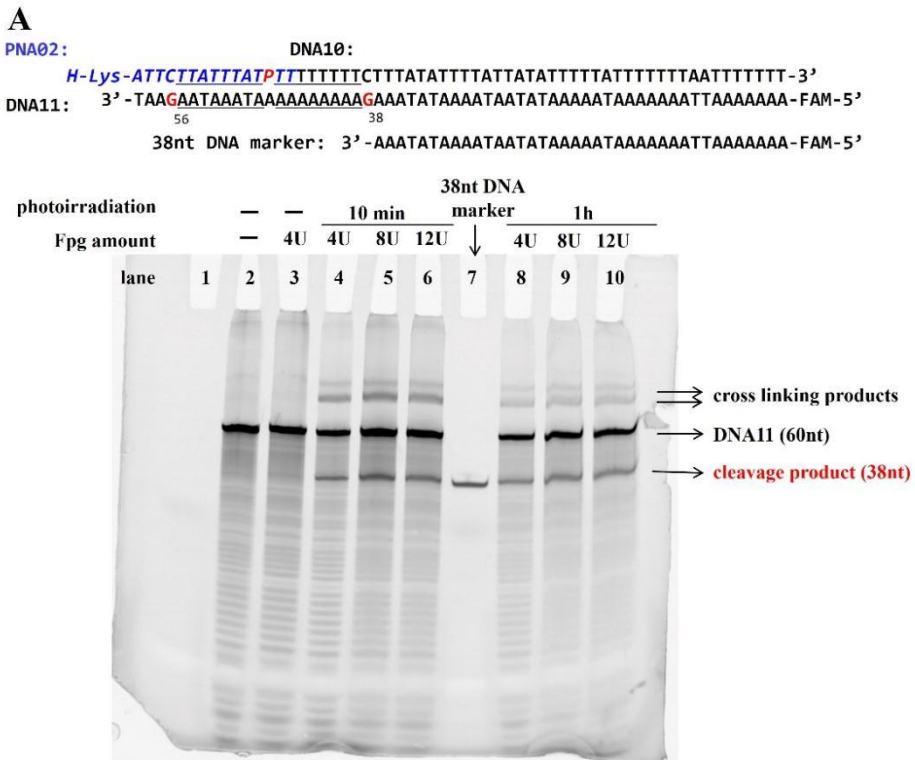

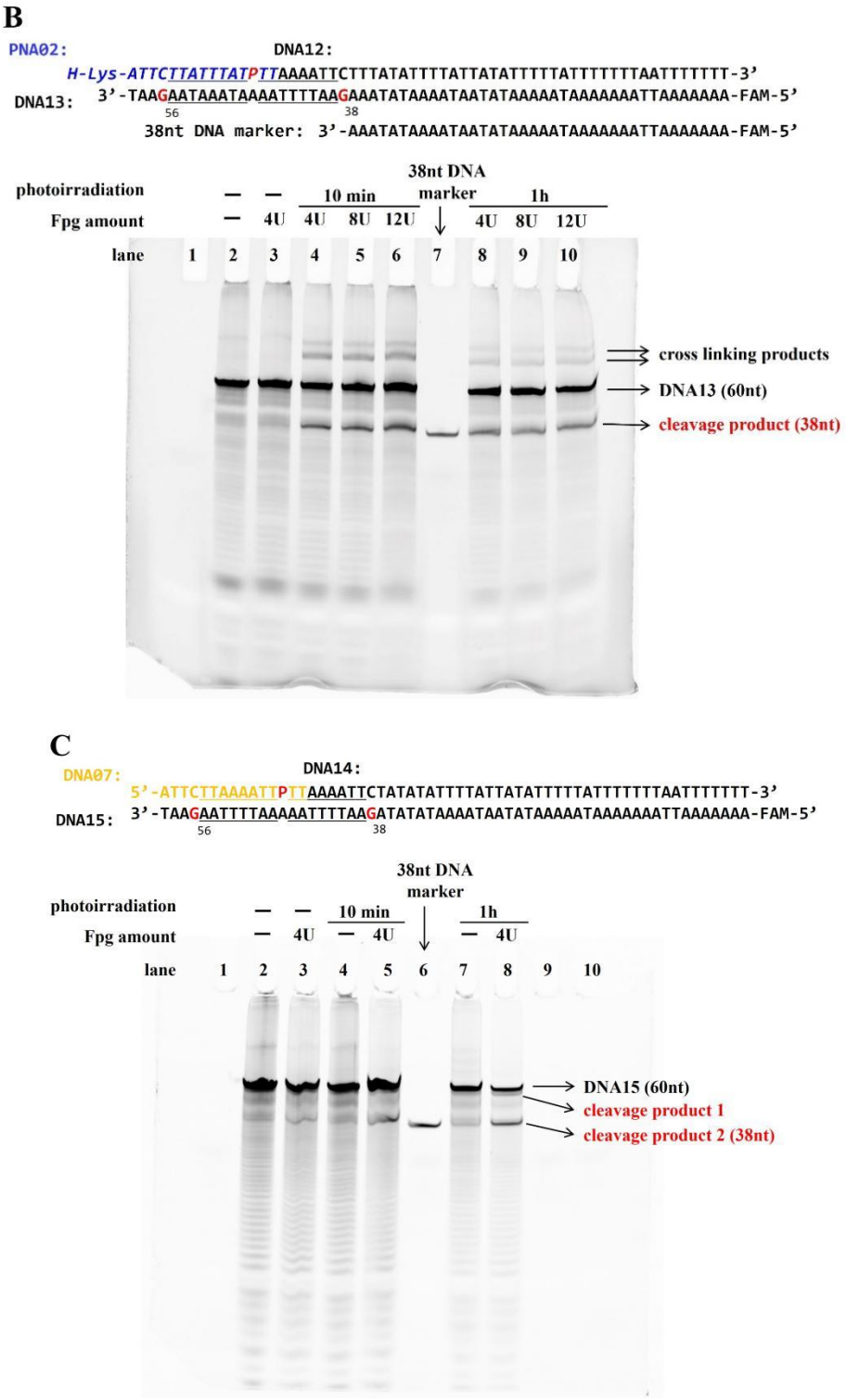

Fig S19. The whole gel image of gel electrophoresis analysis following Fpg treatment illustrates the photooxidation of G in dsDNA by either NBP-PNA or NBP-DNA conjugate bound to the sticky end. (A) PNA02, where the gap sequence within dsDNA region between **P** and G consists of polyT, lane 1 is blank control; (B) PNA02, where the gap sequence within dsDNA region between **P** and G contains interconverting AT, lane 1 is blank control; (C) DNA07, where the dsDNA contains palindromic sequence between **P** and Gs, lane 1, 9 and 10 are blank control. Conditions: A 2-μM duplex in 10-mM sodium phosphate buffer with 100-mM NaCl, pH 7.2 was irradiated with 365-nm

LED for either10 min or 1 h at 20 °C. 5-μL photoirradiation sample or control solution was mixed with Fpg (4 U, 8 U, or 12 U), and incubated at 37 °C for 2 h. Italicized sequences represent PNA, while underlined sequences denote gap regions between Gs and **P**. **P** = NBP-T unit. The numbers under A indicate the relative distance from FAM.

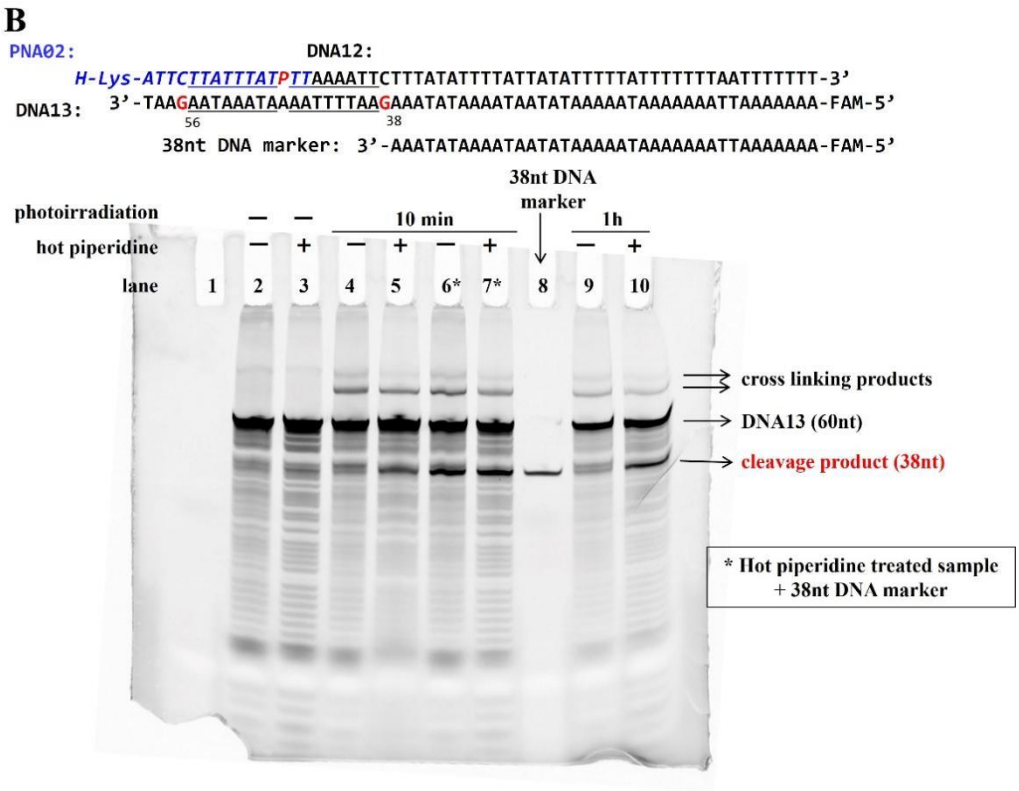

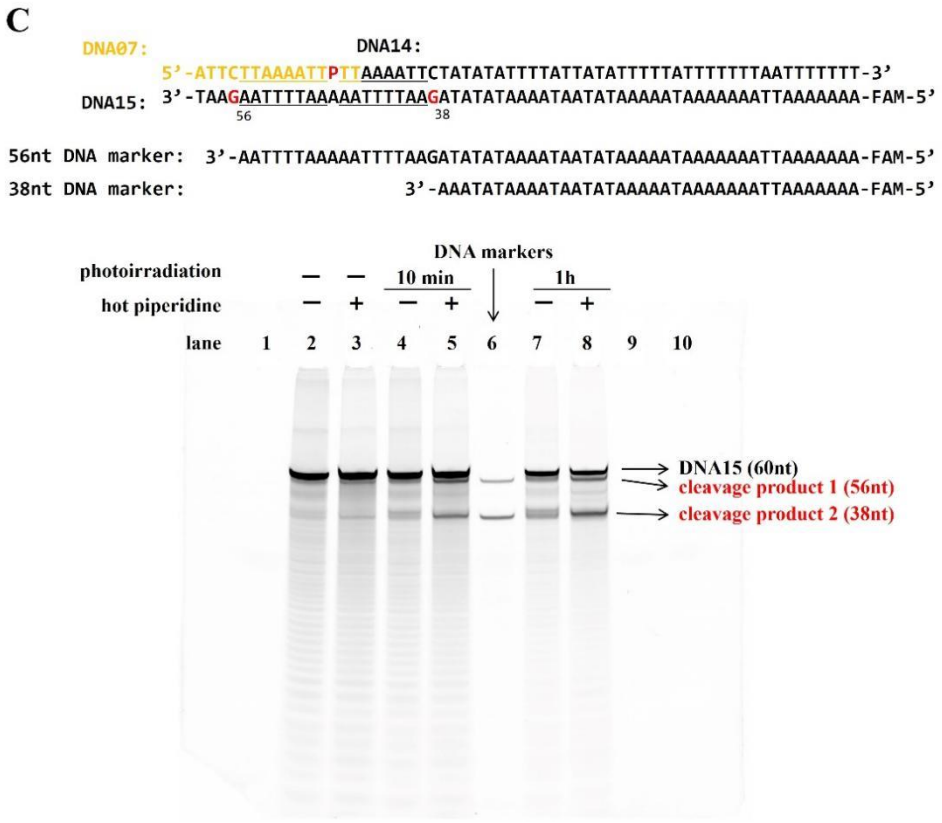

Fig S20. The whole gel image of gel electrophoresis analysis following hot piperidine treatment illustrates the photooxidation of G in dsDNA by either NBP-PNA or NBP-DNA conjugate bound to the sticky end. (A) PNA02, where the gap sequence within dsDNA region between **P** and G consists of polyT, lane 1 is blank control; (B) PNA02, where the gap sequence within dsDNA region between **P** and G conyains interconverting AT, lane 1 is blank control; (C) DNA07, where the dsDNA contains palindromic sequence between **P** and Gs, lane 1, 9 and 10 are blank control. Conditions: 2-μM duplex in 10-mM sodium phosphate buffer with 100-mM NaCl, pH 7.2 was irradiated with 365-nm LED for 10 min or 1 h at 20 °C. 25-μL photoirradiation sample or control solution was mixed with piperidine (1 M, 250 μL), and incubated at 95 °C for 45 min. Italicized sequences represent PNA, while underlined sequences denote gap regions between Gs and **P**. **P** = NBP-T unit. The numbers under A indicate the relative distance from FAM.

PNA invasion and non-denaturing PAGE

A mixture of 40-nM dsDNA (as 1 eq.) and corresponding 1-200 eq. PNA solution in 10-mM sodium phosphate buffer (with 0-mM or 20-mM NaCl, pH = 7.0) (50 or 100 μL) was incubated at 37 ºC overnight. Then 18-μL portion was taken and mixed with 2-μL loading buffer immediately before loading into 12% non-denaturing gel and electrophoresed at 150 V.

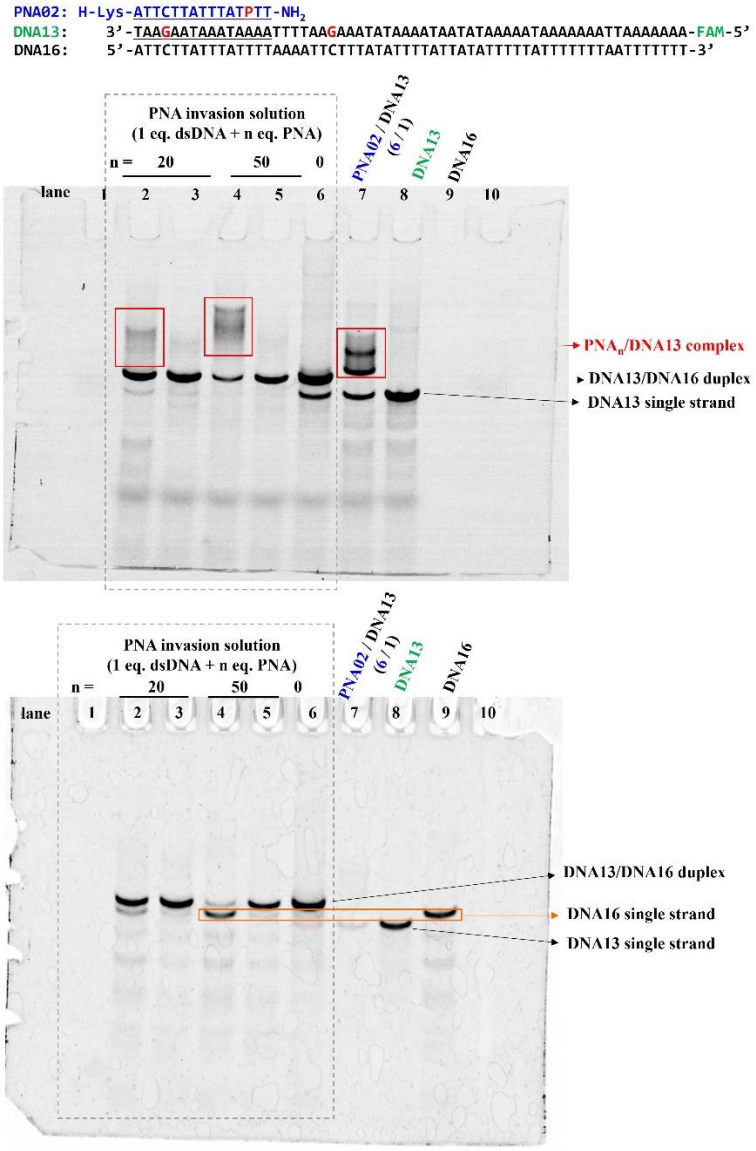

Fig. S21 The sequence of NBP-PNA conjugate (PNA02) and mixed-AT sequence dsDNA (DNA13/DNA16), and the non-denaturing PAGE of incubation solutions of NBP-PNA and dsDNA. The upper gel is imaged of FAM, the lower gel is SYBR Gold staining detection. Condition: lane 1 and 10: only loading buffer, lane 2: 40-nM dsDNA, 800-nM NBP-PNA (20 eq.) in buffer 1; lane 3: 40-nM dsDNA, 800-nM NBP-PNA (20 eq.) in buffer 2; lane 4: 40-nM dsDNA, 2-μM NBP-PNA (50 eq.) in buffer 1; lane 5: 40-nM dsDNA, 2-μM NBP-PNA (50 eq.) in buffer 2, lane 6: 40-nM dsDNA (DNA13: DNA16 = 1:1.2) in buffer 1, lane 7: PNA02 (240-nM) / DNA13 (40-nM) complex (after annealing) in buffer 1, lane 8: 40-nM DNA13 in buffer 1, lane 9: 40-nM DNA16 in buffer 1. Buffer 1: 10 mM sodium phosphate buffer, with 0 mM NaCl, pH = 7.0.

Buffer 2: 10 mM sodium phosphate buffer, with 20 mM NaCl, pH = 7.0.

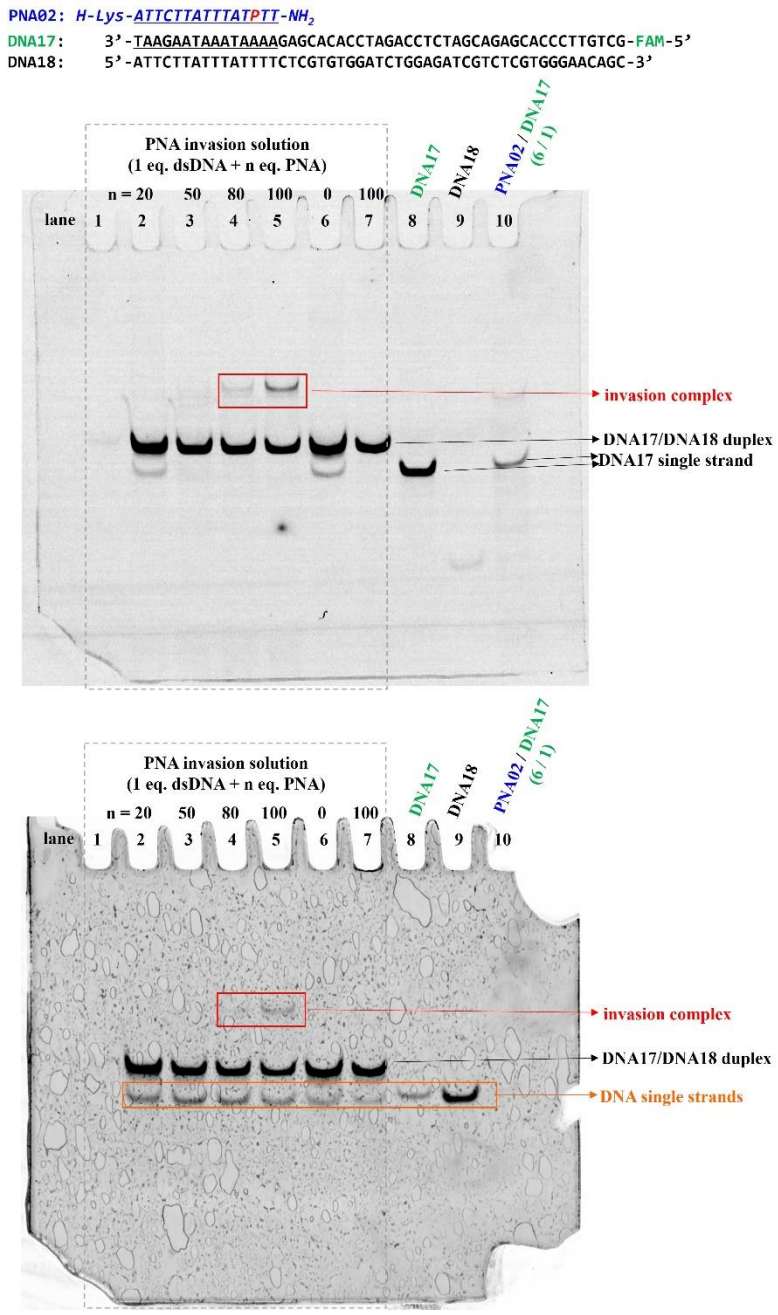

Fig. S22 The sequence of NBP-PNA conjugate (PNA02) and mixed-ATCG sequence dsDNA (DNA17/DNA18), and the non-denaturing PAGE of incubation solutions of NBP-PNA and dsDNA. The upper gel is imaged of FAM, the lower gel is SYBR Gold staining detection. Condition: lane 1: only loading buffer 1, lane 2: 40-nM dsDNA, 0.8-μM NBP-PNA (20 eq.) in buffer 1; lane 3: 40-nM dsDNA, 2-μM NBP-PNA (50 eq.) in buffer 1; lane 4: 40-nM dsDNA, 3.2-μM NBP-PNA (80 eq.) in buffer 1; lane 5: 40-nM dsDNA, 4-μM NBP-PNA (100 eq.) in buffer 1; lane 6: 40-nM dsDNA (DNA13: DNA16 = 1:1.2) in buffer; lane 7: 40-nM dsDNA, 4-μM NBP-PNA (100 eq.) in buffer 2; lane 8: 40-nM DNA17 in buffer 1, lane 9: 40-nM DNA18 in buffer 1; lane 10: PNA02/DNA017 duplex (6:1.2) in buffer 1.

Buffer 1: 10 mM sodium phosphate buffer, with 0 mM NaCl, pH = 7.0.

Buffer 2: 10 mM sodium phosphate buffer, with 10 mM NaCl, pH = 7.0.

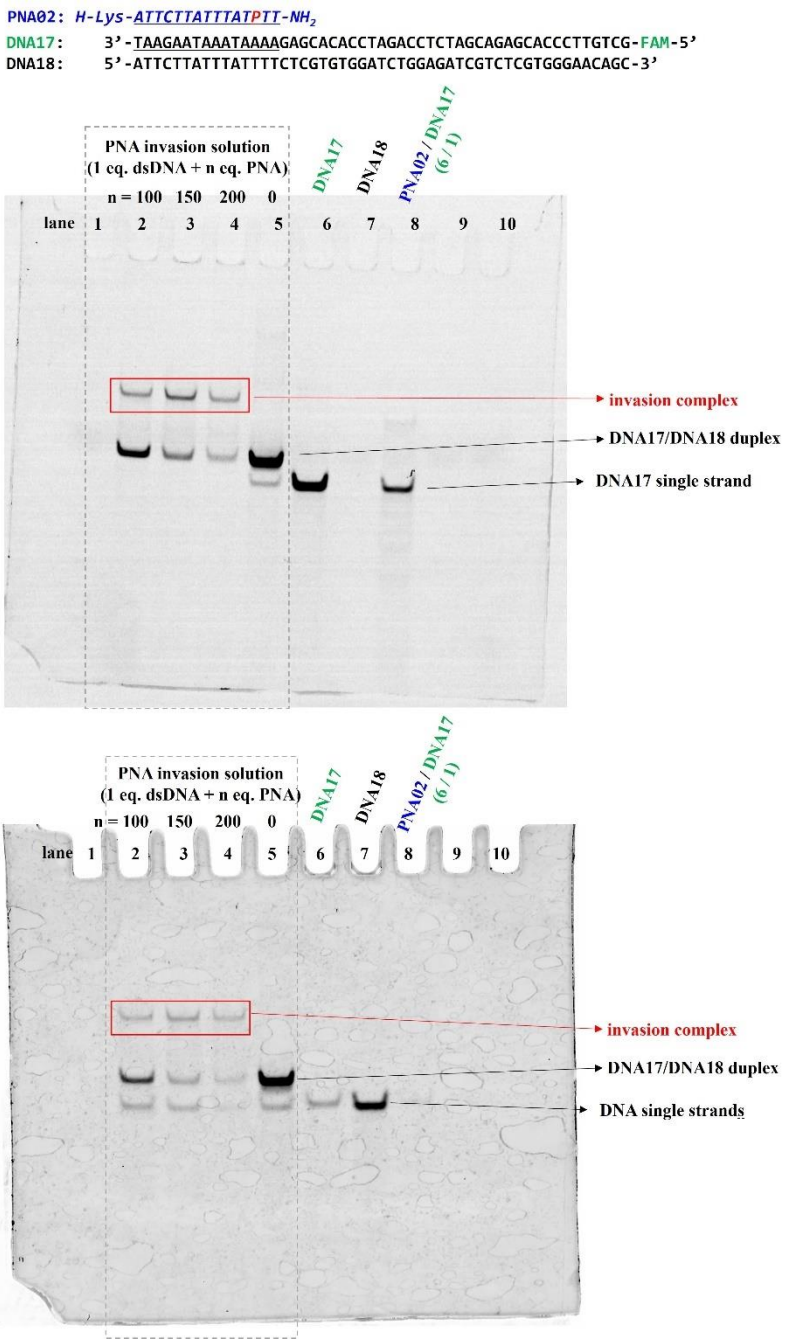

Fig. S23 The sequence of NBP-PNA conjugate (PNA02) and mixed-ATCG sequence dsDNA (DNA17/DNA18), and the non-denaturing PAGE of incubation solutions of NBP-PNA and dsDNA. The upper gel is imaged of FAM, the lower gel is SYBR Gold staining detection. Condition: lane 1, 9 and 10: only loading buffer, lane 2: 40-nM dsDNA, 4-μM NBP-PNA (100 eq.) in buffer; lane 3: 40-nM dsDNA, 6-μM NBP-PNA (150 eq.) in buffer; lane 4: 40-nM dsDNA, 8-μM NBP-PNA (200 eq.) in buffer; lane 5: 40-nM dsDNA (DNA13: DNA16 = 1:1.2) in buffer, lane 6: 40-nM DNA17 in buffer, lane 6: 40-nM DNA18 in buffer.
Buffer: 10 mM sodium phosphate buffer, with 0 mM NaCl, pH = 7.0.

Photoxidation of PNA/dsDNA invasion solution by conjugated NBP and external xylitol-NBP

A mixture of 40-nM dsDNA (as 1 eq.) and corresponding 100 eq. PNA solution in 10-mM sodium phosphate buffer (with 0-mM or 20-mM NaCl, pH = 7.0) (50 or 100 μL) was incubated at 37 °C overnight. Then this invasion solution (50 μL) was irradiated for 10 min or 1 h in the same manner as mentioned above. The photoirradiation samples were treated through the above described Fpg or hot-piperine DNA cleavage method.

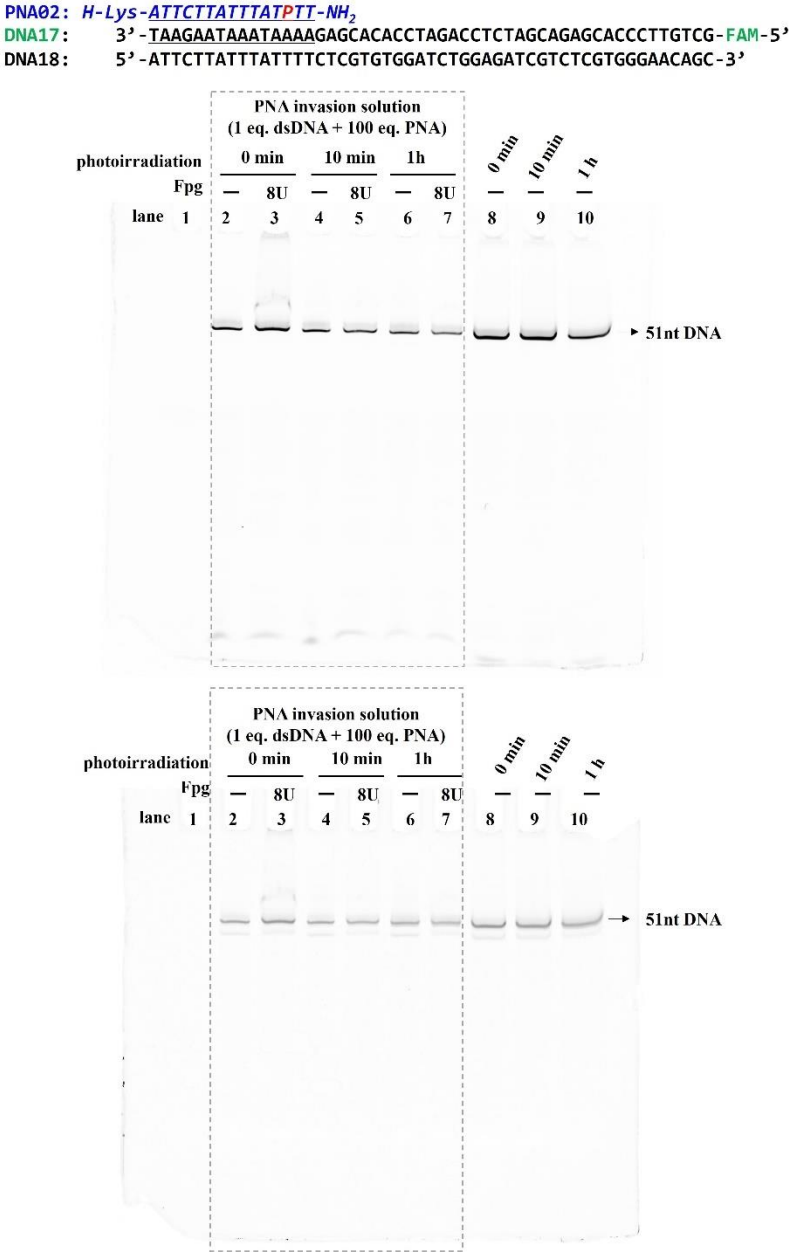

Fig. S24 Denaturing PAGE of photoirradiation and cleavage treatment to invasion solution containing 100 eq. NBP-PNA and 1 eq. dsDNA. The upper gel is imaged of FAM, the lower gel is SYBR Gold staining detection. lane 1: only loading buffer. Condition: 40-nM dsDNA, 4-μM

NBP-PNA (100 eq.) in 10 mM sodium phosphate buffer with 0 mM NaCl, pH = 7.0, incubated at 37 °C overnight. 365-nm light, at 37 °C for 0 min, 10 min or 1 h. Cleavage with Fpg, 8U, 37 °C for 3 h. 20% denaturing PAGE (7-M urea) and electrophoresed at 200 V.

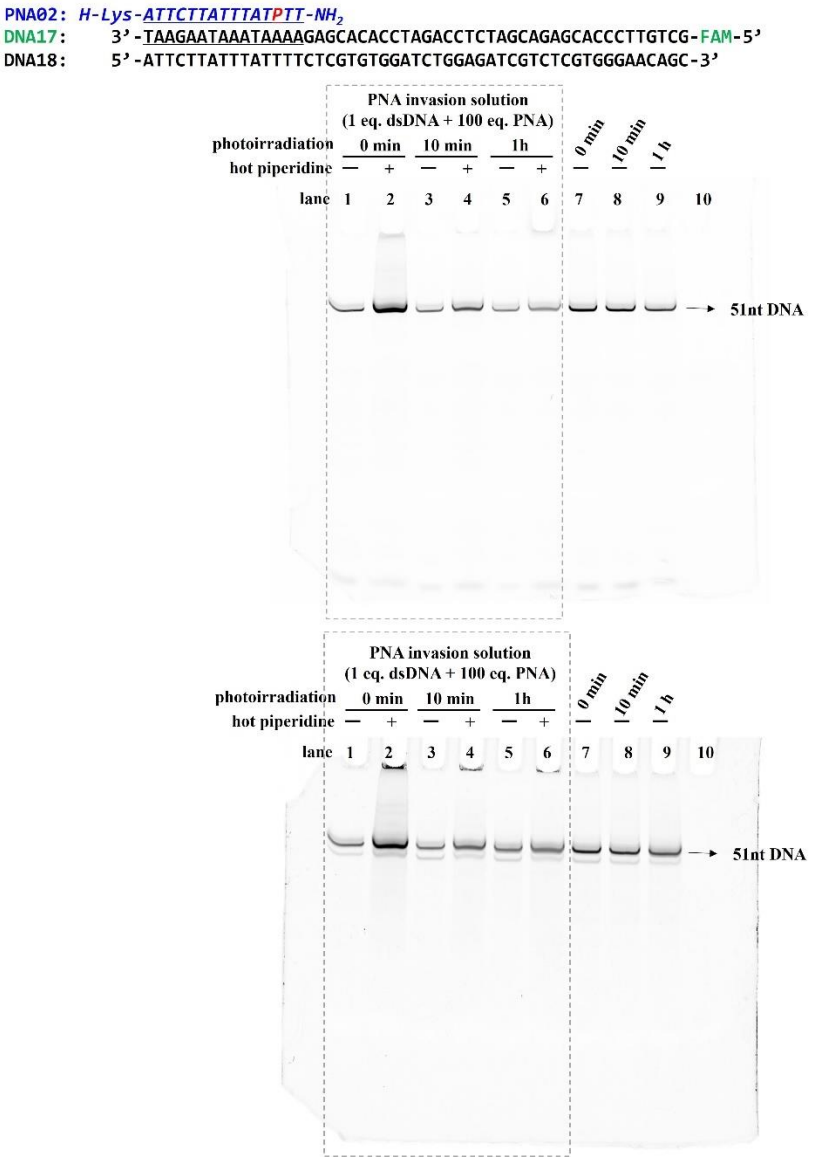

Fig. S25 Denaturing PAGE of photoirradiation and cleavage treatment to invasion solution containing 100 eq. NBP-PNA and 1 eq. dsDNA. The upper gel is imaged of FAM, the lower gel is SYBR Gold staining detection. lane 10: only loading buffer. Condition: 40-nM dsDNA, 4-μM NBP-PNA (100 eq.) in 10 mM sodium phosphate buffer with 0 mM NaCl, pH = 7.2, incubated at 37 °C overnight. 365-nm light, at 37 °C for 0 min, 10 min or 1 h. Cleavage with 1-M piperidine in H_2O, 95 °C for 45 min. 20% denaturing PAGE (7-M urea) and electrophoresed at 200 V.

PNA07: *H-Lys-ATTCTTATTTATTTT-NH_2*
DNA17: 3'-TAAGAATAAATAAAAGAGCACACCTAGACCTCTAGCAGAGCACCCTTGTCG-FAM-5'
DNA18: 5'-ATTCTTATTTATTTTCTCGTGTGGATCTGGAGATCGTCTCGTGGGAACAGC-3'

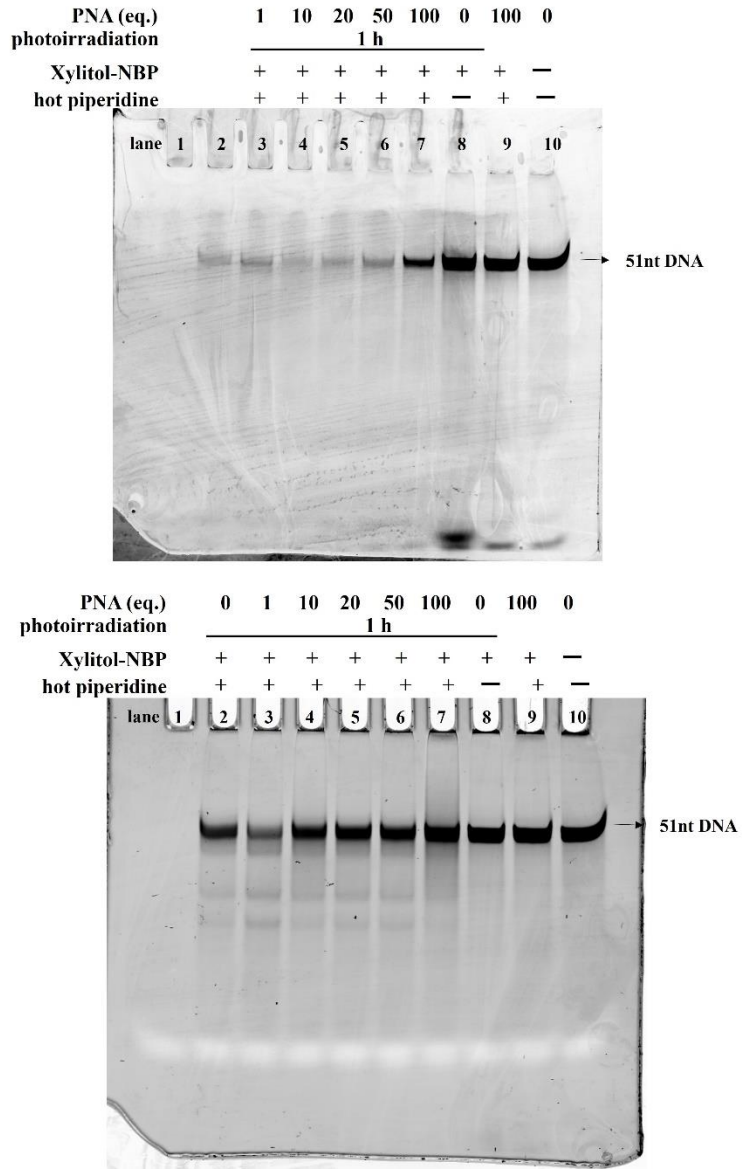

Fig. S26 Effect of PNA self-aggregation on xylitol-NBP-induced dsDNA photodamage. Condition: lane 1: only loading buffer, 40-nM dsDNA (1 eq.), unmodifeied-PNA (1–100 eq.), 4-μM xylitol-NBP in 10 mM sodium phosphate buffer with 0 mM NaCl, pH = 7.0, incubated at 37 °C overnight. 365-nm light, at 37 °C for 0 min or 1 h. Cleavage with 1-M piperidine in H_2O, 95 °C for 45 min. 20% denaturing PAGE (7-M urea) and electrophoresed at 200 V.

REFERENCE

(1) H. Li, Y. Yang, W. Hong, M. Huang, M. Wu, X. Zhao. Applications of Genome Editing Technology in the Targeted Therapy of Human Diseases: Mechanisms, Advances and Prospects. *Signal transduct. target. ther.* **2020**, *5*, 1.

(2) N. S. Alavijeh, A. Serrano, M. S. Peters, C. Wölper, T. Schrader. Design and Synthesis of Artificial Nucleobases for Sequence-Selective DNA Recognition within the Major Groove. *Chem Asian J.* **2023**, *18*, e202300637.

(3) D. B. T. Cox, R. J. Platt, F. Zhang. Therapeutic Genome Editing: Prospects and Challenges. *Nat. Med.* **2015**, *21*, 121–131.

(4) M. S. Cooke, M. D. Evans, M. Dizedaroglu, J. Lunec. Oxidative DNA Damage: Mechanisms, Mutation, and Disease. *FASEB J* . **2003**, *17*, 1195–1214.

(5) K. W. Caldecott. Single-Strand Break Repair and Genetic Disease. *Nat. Rev. Genet.* **2008**, *9*, 619–631.

(6) Y. Chen, X. Yan, Y. Ping. Optical Manipulation of CRISPR/Cas9 Functions: From Ultraviolet to Near-Infrared Light. *ACS Materials Lett.* **2020**, *2*, 644−653.

(7) W. Brown, W. Zhou, A. Deiters. Regulating CRISPR/Cas9 Function through Conditional Guide RNA Control. *ChemBioChem* **2021**, *22*, 63–72.

(8) Y. Tsuga, M. Katou, S. Kuwabara, T. Kanamori, S-I. Ogura, S. Okazaki, H. Ohtani, H. Yuasa. A Twist-Assisted Biphenyl Photosensitizer Passable Through Glucose Channel. *Chem. Asian J.* **2019**, *14*, 2067–2071.

(9) T. Kanamori, S. Kaneko, K. Hamamoto, H. Yuasa. Mapping the Diffusion Pattern of $^1O_2$ Along DNA Duplex by Guanine Photooxidation with an Appended Biphenyl Photosensitizer. *Sci. Rep.* **2023**, *13*, 288.

(10) Y. Aiba, M. Shibata, O. Shoji. Sequence-Specific Recognition of Double-Stranded DNA by Peptide Nucleic Acid Forming Double-Duplex Invasion Complex. *Appl. Sci.* **2022**, *12*, 3677.

(11) J. D. R. Perera, K. E. W. Carufe, P. M. Glazer. Peptide Nucleic Acids and Their Role in Gene Regulation and Editing. *Biopolymers* **2021**, *112*, e23460.

(12) M. Klaper, W. Fudickar, T. Linker. Role of Distance in Singlet Oxygen Applications: A Model System. *J. Am. Chem. Soc.* **2016**, *138*, 7024−7029.

(13) Ł. Ożog, D. Aebisher. Singlet Oxygen Lifetime and Diffusion Measurements. *Eur J Clin Exp Med.* **2018**, *16*, 123–126.

(14) M. Adli. The CRISPR Tool Kit for Genome Editing and Beyond. *Nat. Commun.* **2018**, *9*, 1911.

(15) S. Khadempar, S. Familghadakchi, R. A. Motlagh, N. Farahani, M. Dashtiahangar, H. Rezaei, S. M. G. Hayat CRISPR–Cas9 in Genome Editing: Its Function and Medical Applications. *J Cell Physiol.* **2019**, *234*, 5751–5761.

(16) X. Zhang, X. Jin, R. Sun, M. Zhang, W. Lu, M. Zhao. Gene Knockout in Cellular Immunotherapy: Application and Limitations. *Cancer Letters* **2022**, *540*, 215736.

(17) E. Janik, M. Niemcewicz, M. Ceremuga, L. Krzowski, J. Saluk-Bijak, M. Bijak. Various Aspects of a Gene Editing System—CRISPR–Cas9. *Int. J. Mol. Sci.* **2020**, *21*, 9604.

(18) J. V. D. Oost, C. Patinios. The Genome Editing Revolution. *Trends Biotechnol.*

2023, *41*, 396–409.
(19) Y. Nihongaki, F. Kawano, T. Nakajima, M. Sato. Photoactivatable CrIsPr-Cas9 for Optogenetic Genome Editing. *Nat. Biotechnol.* **2015**, *33*, 755−760.
(20) W. Zhou, W. Brown, A. Bardhan, M. Delaney, A. S. Ilk, R. R. Rauen, S. I. Kahn, M. Tsang, A. Deiters. Spatiotemporal Control of CRISPR/Cas9 Function in Cells and Zebrafish Using Light-Activated Guide RNA. *Angew. Chem. Int. Ed.* **2020**, *59*, 8998–9003.
(21) M. A. Hossain, Y. Lin, S. Yan. Single-Strand Break End Resection in Genome Integrity: Mechanism and Regulation by APE2. *Int. J. Mol. Sci.* **2018**, *19*, 2389.
(22) R. P. Barnes, E. Fouquerel, P. L. Opresko. The Impact of Oxidative DNA Damage and Stress on Telomere Homeostasis. *Mech. Ageing Dev.* **2019**, *177*, 37–45.
(23) J. Y. Hahm, J. Park, ES. Jang, S. W. Chi. 8-Oxoguanine: From Oxidative Damage to Epigenetic and Epitranscriptional Modification. *Exp. Mol. Med.* **2022**, *54*, 1626–1642.
(24) P. Di Mascio, G. R. Martinez, S. Miyamoto, G. E. Ronsein, M. H. G. Medeiros, J. Cadet. Singlet Molecular Oxygen Reactions with Nucleic Acids, Lipids, and Proteins. *Chem. Rev.* **2019**, *119*, 2043–2086.
(25) P. C. Dedon. The Chemical Toxicology of 2-Deoxyribose Oxidation in DNA. *Chem. Res. Toxicol.* **2008**, *21*, 206–219.
(26) C. M. C. Andrés, J. M. P. Lastra, C. A. Juan, F. J. Plou, E. Pérez-Lebeña. Chemical Insights into Oxidative and Nitrative Modifications of DNA. *Int. J. Mol. Sci.* **2023**, *24*, 15240.
(27) T. H. Lee, T. H. Kang. DNA Oxidation and Excision Repair Pathways. *Int. J. Mol. Sci.* **2019**, *20*, 6092.
(28) J. Cadet, J. R. Wagner. DNA Base Damage by Reactive Oxygen Species, Oxidizing Agents, and UV Radiation. *Cold Spring Harb Perspect Biol.* **2013**, *5*, a012559.
(29) B. V. Houten, G. A. Santa-Gonzalez, M. Camargo. DNA Repair after Oxidative Stress: Current Challenges. *Curr. Opin. Toxicol.* **2018**, *7*, 9–16.
(30) T. A. Müller, M. M. Andrzejak, R. P. Hausinger. A Covalent Protein–DNA 5′-Product Adduct Is Generated Following AP Lyase Activity of Human ALKBH1 (AlkB Homologue 1). *Biochem. J.* **2013**, *452*, 509–518.
(31) The Reaction Mechanism of DNA Glycosylase/AP Lyases at Abasic Sites. *Biochem.* **2001**, *40*, 561–568.
(32) H. E. Krokan, M. Bjøras. Base Excision Repair. *Cold Spring Harb Perspect Biol* **2013**, *5*, a012583.
(33) Jan H.J. Hoeijmakers. DNA Damage, Aging, and Cancer. *N Engl J Med* **2009**, *361*, 1475–1485.
(34) H. Sugiyama, I, Saito. Theoretical Studies of GG-Specific Photocleavage of DNA via Electron Transfer: Significant Lowering of Ionization Potential and 5′-Localization of HOMO of Stacked GG Bases in B-Form DNA. *J. Am. Chem. Soc.* **1996**, *118*, 7063–7068.
(35) V. Shafirovich, A. Dourandin, W. Huang, N. E. Geacintov. The Carbonate Radical Is a Site-Selective Oxidizing Agent of Guanine in Double-Stranded

Oligonucleotides. *J Biol Chem.* **2001**, *276*, 24621–24626.
(36) D. Jiang, J. F. Rusling. Oxidation Chemistry of DNA and P53 Tumor Suppressor Gene. *ChemistryOpen* **2019**, *8*, 252–265.
(37) C. E. Crespo-Hernández, D. M. Close, L. Gorb, J. Leszczynski. Determination of Redox Potentials for the Watson−Crick Base Pairs, DNA Nucleosides, and Relevant Nucleoside Analogues. *J. Phys. Chem. B* **2007**, *111*, 5386–5395.
(38) X. Yang, XB. Wang, E. R. Vorpagel, LS. Wang. Direct Experimental Observation of the Low Ionization Potentials of Guanine in Free Oligonucleotides by Using Photoelectron Spectroscopy. *Proc Natl Acad Sci U S A* **2004**, *101*, 17588–17592.
(39) T. Caruso, M. Carotenuto, E. Vasca, A. Peluso. Direct Experimental Observation of the Effect of the Base Pairing on the Oxidation Potential of Guanine. *J. Am. Chem. Soc.* **2005**, *127*, 15040–15041.
(40) J-L. Ravanat, G. Remaud, J. Cadet. Measurement of the Main Photooxidation Products of 2'-Deoxyguanosine Using Chromatographic Methods Coupled to Mass Spectrometry. *Arch Biochem Biophys.* **2000**, *374*, 118–127.
(41) I. E. Kochevar, R. W. Redmond. Photosensitized Production of Singlet Oxygen. *Methods Enzymol. 319*, 20–28.
(42) M. S. Baptista, J. Cadet, P. D. Mascio, A. A. Ghogare, A. Greer, M. R. Hamblin, C. Lorente, S. C. Nunez, M. S. Ribeiro,A. H. Thomas, M. Vignoni, T. M. Yoshimura. Type I and Type II Photosensitized Oxidation Reactions: Guidelines and Mechanistic Pathways. *Photochem. Photobiol.* **2017**, *93*, 912–919.
(43) Z. Li, K. B. Grant. DNA Photo-Cleaving Agents in the Far-Red to near-Infrared Range – a Review. *RSC Adv.* **2016**, *6*, 24617.
(44) V-N. Nguyen, Y. Yan, J. Zhao, J. Yoon. Heavy-Atom-Free Photosensitizers: From Molecular Design to Applications in the Photodynamic Therapy of Cancer. *Acc. Chem. Res.* **2021**, *54*, 207−220.
(45) Y. Rokhlenko, J. Cadet, N. E. Geacintov, V. Shafirovich. Mechanistic Aspects of Hydration of Guanine Radical Cations in DNA. *J. Am. Chem. Soc.* **2014**, *136*, 5956−5962.
(46) W. L. Neeley, J. M. Essigmann. Mechanisms of Formation, Genotoxicity, and Mutation of Guanine Oxidation Products. *Chem. Res. Toxicol.,* **2006**, *19*, 491–505.
(47) J. Cadet, T. Douki, D. Gasparutto, JL. Ravant. Oxidative Damage to DNA: Formation, Measurement and Biochemical Features. *Mutat. Res.* **2003**, *531*, 5–23.
(48) J. Cadet, R. Treoule. Comparative Study of Oxidation of Nucleic Acid Components by Hydroxyl Radicals, Singlet Oxygen and Superoxide Anion Radicals. *Photochem Photobiol.* **1978**, *28*, 661–667.
(49) J. L. Ravanat, E. Dumont. Reactivity of Singlet Oxygen with DNA, an Update. *Photochem Photobiol.* **2022**, *98*, 564–571.
(50) J. Cadet, J. L. Ravanat, G. R. Martinez, M. H. G. Medeiros, P. D. Mascio. Singlet Oxygen Oxidation of Isolated and Cellular DNA: Product Formation and Mechanistic Insights. *Photochem. Photobiol.* **2006**, *82*, 1219–1225.
(51) J.C. Niles, J.S. Wishnok, S.R. Tannenbaum. Spiroimino-Dihydantoin Is the

Major Product of 8-Oxo-7,8-Dihydro-Guanosine Reaction with Peroxynitrite in the Presence of Thiols and Guanosine Photooxidation by Methylene Blue. *Org. Lett.* **2001**, *3*, 963–966.

(52) J-L. Ravanat, G. R. Martinez, M. H.G. Medeiros, P. D. Mascio, J. Cadet. Mechanistic Aspects of the Oxidation of DNA Constituents Mediated by Singlet Molecular Oxygen. *Arch. Biochem. Biophys.* **2004**, *423*, 23–30.

(53) L. F. Agnez-Lima, J. T.A. Melo, A. E. Silva, A. H. S. Oliveira, A. R. S. Timoteo, K. M. Lima-Bessa, G. R. Martinez, M. H.G. Medeiros, P. D. Mascio, R. S. Galhardo, C. F.M. Menck. DNA Damage by Singlet Oxygen and Cellular Protective Mechanisms. *Mutat. Res.* **2012**, *751*, 15–28.

(54) N. Kumar, A. F. Theil, V. Roginskaya, Y. Ali, M. Calderon, S. C. Watkins, R. P. Barnes, P. L. Opresko, A. Pines, H. Lans, W. Vermeulen, B. Van Houten. Global and Transcription-Coupled Repair of 8-oxoG Is Initiated by Nucleotide Excision Repair Proteins. *Nat. Commun.* **2022**, *13*, 974.

(55) S. Jang, N. Kumar, E. C. Beckwitt, M. Kong, E. Fouquerel, V. Rapić-Otrin, R. Prasad, S. C. Watkins, C. Khuu, C. Majumdar, S. S. David, S. H. Wilson, M. P. Bruchez, P. L. Opresko, B. Van Houten. Damage Sensor Role of UV-DDB During Base Excision Repair. *Nat. Struct. Mol. Biol.* **2019**, *26*, 695–703.

(56) G. Niogret, C. Cheriaux, F. Bonhomme, F. Levi-Acobas, C. Figliola, G. Ulrich, G. Gasser, M. Hollenstein. A Toolbox for Enzymatic Modification of Nucleic Acids with Photosensitizers for Photodynamic Therapy. *RSC Chem. Biol.* **2024**, *5*, 841.

(57) B. Armitage. Photocleavage of Nucleic Acids. *Chem. Rev.* **1998**, *98*, 1171−1200.

(58) A. Biton, A. Ezra, J. Kasparkova, V. Brabec, E. Yavin. DNA Photocleavage by DNA and DNA-LNA Amino Acid-Dye Conjugates. *Bioconjugate Chem.* **2010**, *21*, 616–621.

(59) S. Takahashi, N. Sugimoto. Watson−Crick versus Hoogsteen Base Pairs: Chemical Strategy to Encode and Express Genetic Information in Life. *Acc. Chem. Res.* **2021**, *54*, 2110−2120.

(60) A. S. Boutorine, D. Brault, M. Takasugi, O. Delgado, C. He le ne. Chlorin-Oligonucleotide Conjugates: Synthesis, Properties, and Red Light-Induced Photochemical Sequence-Specific DNA Cleavage in Duplexes and Triplexes. *J. Am. Chem. Soc.* **1996**, *118*, 9469–9476.

(61) Z. Han, Y. Qian, Y. Wu, Y. Cai, J. Jin, Z. Yang. Metal-Organic Frameworks Deliver a Conjugate of Functional Oligonucleotides and Photosensitizer to Induce Apoptosis for Enhancing Chemotherapy. *ChemNanoMat. 7*, 1361–1368.

(62) C. W. Crean, R. Camier, M. Lawler, C. Stevenson, R. J. H. Davies, P. H. Boyle, J. M. Kelly. Synthesis of N_3- and 2-NH_2-Substituted 6,7-Diphenylpterins and Their Use as Intermediates for the Preparation of Oligonucleotide Conjugates Designed to Target Photooxidative Damage on Single-Stranded DNA Representing the Bcr–Abl Chimeric Gene. *Org. Biomol. Chem.* **2004**, *2*, 3588–3601.

(63) P. Muangkaew, T. Vilaivan. Modulation of DNA and RNA by PNA. *Bioorg. Med. Chem. Lett.* **2024**, *30*, 127064.

(64) M. Bege, A. Borbás. The Medicinal Chemistry of Artificial Nucleic Acids and Therapeutic Oligonucleotides. *Pharmaceuticals* **2022**, *15*, 909.
(65) R. Brazil. Peptide Nucleic Acids Promise New Therapeutics and Gene Editing Tools. *ACS Cent. Sci.* **2023**, *9*, 3−6.
(66) T. Marsic, S. R. Gundra, Q. Wang, R. Aman, A. Mahas, M. M. Mahfouz. Programmable Site-Specific DNA Double-Strand Breaks via PNA-Assisted Prokaryotic Argonautes. *Nucleic Acids Res.* **2023**, *51*, 9491–9506.
(67) N. Brodyagin, M. Katkevics, V, Kotikam, C. A. Ryan, E. Rozners. Chemical Approaches to Discover the Full Potential of Peptide Nucleic Acids in Biomedical Applications. *Beilstein J. Org. Chem.* **2021**, *17*, 1641–1688.
(68) M. Tanaka, N. Shigi, J. Sumaoka. M. Komiyama. Thiazole Orange-Conjugated Peptide Nucleic Acid for Fluorescent Detection of Specific DNA Sequences and Site-Selective Photodamage. *RSC Adv.* **2014**, *4*, 63533–63538.
(69) Y. Shemesh, E. Yavin. PNA−Rose Bengal Conjugates as Efficient DNA Photomodulators. *Bioconjugate Chem.* **2015**, *26*, 1916−1922.
(70) A. Okamoto, K. Tanabe, C. Dohno, I. Saito. Modulation of Remote DNA Oxidation by Hybridization with Peptide Nucleic Acids (PNA). *Bioorg. Med. Chem.* **2002**, *10*, 713–718.
(71) D. A. Braasch, D. R. Corey. Synthesis, Analysis, Purification, and Intracellular Delivery of Peptide Nucleic Acids. *Methods* **2001**, *23*, 97–107.
(72) T. Tomori, Y. Miyatake, Y. Sato, T. Kanamori, Y. Masaki, A. Ohkubo, M. Sekine, K. Seio. Synthesis of Peptide Nucleic Acids Containing Pyridazine Derivatives as Cytosine and Thymine Analogs, and Their Duplexes with Complementary Oligodeoxynucleotides. *Org. Lett.* **2015**, *17*, 1609−1612.
(73) A. Y. Shaikh, F. Björkling, P. E. Nielsen, H. Franzyk. Optimized Synthesis of Fmoc/Boc-Protected PNA Monomers and Their Assembly into PNA Oligomers. *Eur. J. Org. Chem.* **2021**, *2021*, 2792–2801.
(74) R. H. E. Hudson, G. Li, J. Tse. The Use of Sonogashira Coupling for the Synthesis of Modified Uracil Peptide Nucleic Acid. *Tetrahedron Lett.* **2002**, *43*, 1381–1386.
(75) S. D. Lepore, Y. He. Use of Sonication for the Coupling of Sterically Hindered Substrates in the Phenolic Mitsunobu Reaction. *J. Org. Chem.* **2003**, *68*, 8261–8263.
(76) Y. Du, T. Kanamori, Y. Yaginuma, N. Yoshida, S. Kaneko, H. Yuasa. Diffusion of $^1O_2$ along the PNA Backbone Diminishes the Efficiency of Photooxidation of PNA/DNA Duplexes by Biphenyl Photosensitizer. *Bioorg. Med. Chem. Lett.* **2024**, *114*, 129988.
(77) P. Jain, D. B. Badger, Y. Liang, A. W. Gebhard, D. Santiago, P. Murray, S. R. Kaulagari, T. J. Gauthier, R. Nair, M. Kumar, W. C. Guida, L. A. Hazlehurst, M. L. McLaughlin. Bioactivity Improvement via Display of the Hydrophobic Core of HYD1 in a Cyclic β-Hairpin-Like Scaffold, MTI-101. *Pept Sci (Hoboken).* **2021**, *113*, e24199.
(78) M. Meldal, C. W. Tornøe. Cu-Catalyzed Azide-Alkyne Cycloaddition. *Chem. Rev. 108*, 2952–3015.

(79) S. Pothukanuri, Z. Pianowski, N. Winssinger. Expanding the Scope and Orthogonality of PNA Synthesis. *Eur. J. Org. Chem.* **2008**, 3141–3148.
(80) K. P. Nandhini, D. Al Shaer, F. Albericio, B. G. de la Torre. The Challenge of Peptide Nucleic Acid Synthesis. *Chem. Soc. Rev.* **2023**, *52*, 2764.
(81) D. A. T. Pires, M. P. Bemquerer, C. J. d. Nascimento. Some Mechanistic Aspects on Fmoc Solid Phase Peptide Synthesis. *Int. J. Pept. Res. Ther.* **2014**, *20*, 53–69.
(82) S. A. Thomson, J. A. Josey, R. Cadilla, M. D. Gaul, C. F. Hassman, Michael J. Luzzio, A. J. Pipe, K. L. Reed, D. J. Ricca, R. W. Wiethe, S. A. Noble. Fmoc Mediated Synthesis of Peptide Nucleic Acids. *Tetrahedron* **1995**, *51*, 6179–6194.
(83) J. C. Norton, J. H. Waggenspack, E. Varnum, D. R. Corey. Targeting Peptide Nucleic Acid-Protein Conjugates to Structural Features within Duplex DNA. *Bioorg Med Chem.* **1995**, *3*, 437–445.
(84) I. Coin, M. Beyermann, M. Bienert. Solid-Phase Peptide Synthesis: From Standard Procedures to the Synthesis of Difficult Sequences. *Nat. Protoc.* **2007**, *2*, 3247–3256.
(85) A. D. Bene, A. D'Aniello, S. Tomassi, F. Merlino, V. Mazzarella, R. Russo, A. Chambery, S. Cosconati, S. D. Maro, A. Messere. Ultrasound-Assisted Peptide Nucleic Acids Synthesis (US-PNAS). *Ultrason. Sonochem.* **2013**, *95*, 106360.
(86) J. Tailhades, H. Takizawa, M. J. Gait, D. A. Wellings, J. D. Wade, Y. Aoki, F. Shabanpoor. Solid-Phase Synthesis of Difficult Purine-Rich PNAs through Selective Hmb Incorporation: Application to the Total Synthesis of Cell Penetrating Peptide-PNAs. *Front. Chem.* **2017**, *5*, 81.
(87) A. Isidro-Llobet, M. N. Kenworthy, S. Mukherjee, M. E. Kopach, Katarzyna Wegner, F. Gallou, A. G. Smith, F. Roschangar. Sustainability Challenges in Peptide Synthesis and Purification: From R&D to Production. *J. Org. Chem.* **2019**, *84*, 4615−4628.
(88) M. Egholm, O. Buchardt, L. Christensen, C. Behrens, S. M. Freier, D. A. Driver, R. H. Berg, S. K. Kim, B. Norden, P. E. Nielsen. PNA Hybridizes to Complementary Oligonucleotides Obeying the Watson–Crick Hydrogen-Bonding Rules. *Nature* **1993**, *365*, 566–568.
(89) A. A. Kuznetsova, L. I. Soloveva, O. S. Fedorova. Single-Stranded DNA Modification by an Oligonucleotide–Phthalocyanine Fe(II) Conjugate: The Kinetic Features and the Process Mechanism. *Russ. J. Bioorg. Chem.* **2008**, *34*, 2008.
(90) C. W. Crean, Y. T. Kavanagh, C. M. O'Keeffe, M. P. Lawler, C. Stevenson, R. J. H. Davies, P. H. Boyle, J. M. Kelly. Targeting of Photooxidative Damage on Single-Stranded DNA Representing the *bcr-abl* Chimeric Gene Using Oligonucleotide-Conjugates Containing $[Ru(Phen)_3]^{2+}$-like Photosensitiser Groups. *Photochem. Photobiol. Sci.,* **2002**, *1*, 1024–1033.
(91) A. Yuan, B. Laing, Y. Hu, Xin Ming. Direct Oligonucleotide–Photosensitizer Conjugates for Photochemical Delivery of Antisense Oligonucleotides. *Chem. Commun.* **2015**, *51*, 6678–6680.
(92) V. V. Demidov, M. D. Frank-Kamenetskii. Two Sides of the Coin: Affinity and Specificity of Nucleic Acid Interactions. *Trends Biochem. Sci.* **2004**, *29*, 62–71.

(93) A. Biton, A. Ezra, J. Kasparkova, V. Brabec, and E. Yavin. DNA Photocleavage by DNA and DNA-LNA Amino Acid-Dye Conjugates. *Bioconjugate Chem.* **2010**, *21*, 616–621.
(94) K. E. Herbert, M. D. Evans, M. T.V. Finnegan, S. Farooq, N. Mistry, I. D. Podmore, P. Farmer, J. Lunec. Novel HPLC Procedure for The Analysis of 8-Oxoguanine in DNA Analysis. *Free Radic Biol Med* **1996**, *20*, 467–473.
(95) S. Frelon, T. Douki, J. Ravanat, J. Pouget, C. Tornabene, J. Cadet. High-Performance Liquid Chromatography-Tandem Mass Spectrometry Measurement of Radiation-Induced Base Damage to Isolated and Cellular DNA. *Chem. Res. Toxicol.* **2000**, *13*, 1002–1010.
(96) K. S. Lim, K. Taghizadeh, J. S. Wishnok, I. R. Babu, V. Shafirovich, N. E. Geacintov, P. C. Dedon. Sequence-Dependent Variation in the Reactivity of 8-Oxo-7,8-Dihydro-2′-Deoxyguanosine toward Oxidation. *Chem. Res. Toxicol.* **2012**, *25*, 366–373.
(97) Y. You. Chemical Tools for the Generation and Detection of Singlet Oxygen. *Org. Biomol. Chem.* **2018**, *16*, 4044–4065.
(98) H. Wu, Q. Song, G. Ran, X. Lu. Recent Developments in the Detection of Singlet Oxygen with Molecular Spectroscopic Methods. *Trends Anal. Chem.* **2011**, *30*, 133–141.
(99) D. P. Langlois, H. Wolff. Pseudo Esters of Levulinic Acid. *J. Am. Chem. Soc.* **1948**, *70*, 2624–2626.
(100) E. Appiani, R. Ossola, D. E. Latch, P. R. Erickson, K. McNeill. Aqueous Singlet Oxygen Reaction Kinetics of Furfuryl Alcohol: Effect of Temperature, pH, and Salt Content. *Environ Sci Process Impacts* **2017**, *19*, 507–516.
(101) W. R. Haag, J. Hoigne, E. Gassman, A. M. Braun. Singlet Oxygen in Surface Waters — Part I: Furfuryl Alcohol as a Trapping Agent. *Chemosphere,* **1984**, *13*, 631–640.
(102) B. Matter, D. Malejka-Giganti, A. S. Csallany, N. Tretyakova. Quantitative Analysis of the Oxidative DNA Lesion, 2,2-diamino-4-(2-deoxy-β-D-*erythro*-pentofuranosyl)amino]-5(2*H*)-oxazolone (oxazolone), *in vitro* and *in vivo* by Isotope Dilution-Capillary HPLC-ESI-MS/MS. *Nucleic Acids Res.* **2006**, *34*, 5449–5460.
(103) E. Hatcher, A. Balaeff, S. Keinan, R. Venkatramani, D. N. Beratan. PNA versus DNA: Effects of Structural Fluctuations on Electronic Structure and Hole-Transport Mechanisms. *J. Am. Chem. Soc.* **2008**, *130*, 11752–11761.
(104) S. Diekmann, D. A. Zarling. Unique Poly(dA)•Poly(dT) B'-Confonnation in Cellular and Synthetic DNAs. *Nucleic Acids Res.* **1987**, *15*, 6063–6074.
(105) K. J. McConnell, D. L. Beveridge. Molecular Dynamics Simulations of B'-DNA: Sequence Effects on A-Tract-Induced Bending and Flexibility. *J. Mol. Biol.* **2001**, *314*, 23–40.
(106) D. MacDonald, K. Herbert, X. Zhang, T. Polgruto, P. Lu. Solution Structure of an A-Tract DNA Bend. *J. Mol. Biol.* **2001**, *306*, 1081–1098.
(107) C. Yoon, G. G. Privé, D. S. Goodsell, R. E. Dickerson. Structure of an Alternating-B DNA Helix and Its Relationship to A-Tract DNA. *Proc Natl Acad*

Sci USA **1988**, *85*, 6332–6336.
(108) K. M. Vasquez, P. M. Glazer. Triplex-Forming Oligonucleotides: Principles and Applications. *Q. Rev. Biophys.* **2002**, *35*, 89–107.
(109) B. Marchetti, T. N. V. Karsili. An Exploration of the Reactivity of Singlet Oxygen with Biomolecular Constituents. *Chem. Commun.* **2016**, *52*, 10996–10999.
(110) G. R. Martinez, A. P. M. Loureiro, S. A. Marques, S. Miyamoto, L. F. Yamaguchi, J. Onuki, E. A. Almeida, C. C. M. Garcia, L. F. Barbosa, M. H.G. Medeiros, P. D. Mascio. Oxidative and Alkylating Damage in DNA. *Mutat. Res.* **2003**, *544*, 115–127.
(111) W. Lu, J. Liu. Capturing Transient Endoperoxide in the Singlet Oxygen Oxidation of Guanine. *Chem. Eur. J.* **2016**, *22*, 3127–3138.
(112) E. Dumont, R. Gruber, E. Bignon, C. Morell, J. Aranda, J.-L. Ravanat, I. Tunon. Singlet Oxygen Attack on Guanine: Reactivity and Structural Signature within the B-DNA Helix. *Chem. Eur. J.* **2016**, *22*, 12358–12362.
(113) E. Dumont, R. Grüber, E. Bignon, C. Morell, Y. Moreau, A. Monari, J-L. Ravanat. Probing the Reactivity of Singlet Oxygen with Purines. *Nucleic Acids Res.* **2016**, *44*, 56–62.
(114) K. S. Lim, L. Cui, K. Taghizadeh, J. S. Wishnok, Wan Chan, M. S. DeMott, I. R. Babu, S. R. Tannenbaum, P. C. Dedon. *In Situ* Analysis of 8-Oxo-7,8-dihydro-2′-deoxyguanosine Oxidation Reveals Sequence- and Agent-Specific Damage Spectra. *J. Am. Chem. Soc.* **2012**, *134*, 18053−18064.
(115) D. W. Ussery. DNA Structure: A-, B- and Z-DNA Helix Families. *Encyclopedia Life Sci.* **2002**, *1*, e003122.
(116) T. Ratilainen, A. Holmen, E. Tuite, G. Haaima, L. Christensen, P. E. Nielsen, B. Norden. Hybridization of Peptide Nucleic Acid. *Biochem. J.* **1998**, *37*, 12331–12342.
(117) M. Eriksson. Structure of PNA-Nucleic Acid Complexes. *Nucleosides Nucleotides Nucleic Acids* **1997**, *16*, 617–621.
(118) P. E. Nielsen. Structural and Biological Properties of Peptide Nucleic Acid (PNA). *Pure & Appl. Chem.* **1998**, *70*, 105–110.
(119) M. Eriksson, P. E. Nielsen. Solution Structure of a Peptide Nucleic Acid-DNA Duplex. *Nat Struct Biol.* **1996**, *3*, 410–413.
(120) J. I. Yeh, B. Shivachev, S. Rapireddy, M. J. Crawford, R. R. Gil, S. Du, M. Madrid, D. H. Ly. Crystal Structure of Chiral γPNA with Complementary DNA Strand: Insights into the Stability and Specificity of Recognition and Conformational Preorganization. *J. Am. Chem. Soc.* **2010**, *132*, 10717–10727.
(121) F. Wilkinson, W. P. Helman, A. B. Ross. Rate Constants for the Decay and Reactions of the Lowest Electronically Excited Singlet State of Molecular Oxygen in Solution. An Expanded and Revised Compilation. *J. Phys. Chem. Ref. Data* **1995**, *24*, 663–677.
(122) G. Hazarika, R. Dutta, D. P. Saikia, D. Malakar, M. Hazorika, M. Bora. A Comprehensive Exploration of Restriction Enzymes and Their Applications in Molecular Biology: A Review. *N.a. J. Adv. Res. Rev.* **2014**, *21*, 2399–2404.
(123) E. Ban, C. R. Picu. Strength of DNA Sticky End Links. *Biomacromolecules* **2014**,

15, 143−149.
(124) J. Tchou, A. P. Grollman. The Catalytic Mechanism of Fpg Protein: Evidence for a Schiff Base Intermediate and Amino Terminus Localization of the Catalytic Site. *J. Biol. Chem.* **1995**, *270*, 11671–11677.
(125) D. O. Zharkov, G. Shoham, A. P. Grollman. Structural Characterization of the Fpg Family of DNA Glycosylases. *DNA Repair (Amst)* **2003**, *2*, 839–862.
(126) G. Pratviel, B. Meunier. Guanine Oxidation: One- and Two-Electron Reactions. *Chem. Eur. J.* **2006**, *12*, 6018–6030.
(127) M. Dizdaroglu, E. Coskun, P. Jaruga. Repair of Oxidatively Induced DNA Damage by DNA Glycosylases: Mechanisms of Action, Substrate Specificities and Excision Kinetics. *Mutat. Res. Rev. Mutat. Res.* **2017**, *771*, 99–127.
(128) A. M. Fleming, O. Alshykhly, J. Zhu, J. G. Muller, C. J. Burrows. Rates of Chemical Cleavage of DNA and RNA Oligomers Containing Guanine Oxidation Products. *Chem. Res. Toxicol.* **2015**, *28*, 1292−1300.
(129) A. Spassky, D. Angelov. Influence of the Local Helical Conformation on the Guanine Modifications Generated from One-Electron DNA Oxidation. *Biochem. J.* **1997**, *36*, 6571–6576.
(130) P. E. Nielsen, M. Egholm, R. H. Berg, O. Buchardt. Sequence-Selective Recognition of DNA by Strand Displacement with a Thymine-Substituted Polyamide. *Science* **1991**, *254*, 1497–1500.
(131) T. Bentin, P. E. Nielsen. Enhanced Peptide Nucleic Acid Binding to Supercoiled DNA: Possible Implications for DNA "Breathing" Dynamics. *Biochem. J.* **1996**, *35*, 8863–8869.
(132) X. Zhang, T. Ishihara, D. R. Corey. Strand Invasion by Mixed Base PNAs and a PNA–Peptide Chimera. *Nucleic Acids Res.* **2000**, *28*, 3332–3338.
(133) I. V. Smolin, V. V. Demidov, V. A. Soldatenkov, S. G. Chasovskikh, M. D. Frank-Kamenetskii. End Invasion of Peptide Nucleic Acids (PNAs) with Mixed-Base Composition into Linear DNA Duplexes. *Nucleic Acids Res.* **2005**, *33*, e146.
(134) G. He, S. Rapireddy, R. Bahal, B. Sahu, D. H. Ly. Strand Invasion of Extended, Mixed-Sequence B-DNA by γPNAs. *J. Am. Chem. Soc.* **2009**, *131*, 12088–12090.
(135) S. Rapireddy, R. Bahal, Danith H. Ly. Strand Invasion of Mixed-Sequence, Double-Helical B-DNA by γ-Peptide Nucleic Acids Containing G-Clamp Nucleobases under Physiological Conditions. *Biochem.* **2011**, *50*, 3913–3918.
(136) R. Bahal, B. Sahu, S. Rapireddy, C. Lee, D. H. Ly. Sequence-Unrestricted, Watson–Crick Recognition of Double Helical B-DNA by (R)-MiniPEG-γPNAs. *ChemBioChem* **2012**, *13*, 56–60.
(137) J. Lohse, O. Dahl, P. E. Nielsen. Double Duplex Invasion by Peptide Nucleic Acid: A General Principle for Sequence-Specific Targeting of Double-Stranded DNA. *Proc. Natl. Acad. Sci. U.S.A.* **1999**, *96*, 21.
(138) T. Bentin, H. J. Larsen, P. E. Nielsen. Combined Triplex/Duplex Invasion of Double-Stranded DNA by "Tail-Clamp" Peptide Nucleic Acid. *Biochem.* **2003**, *42*, 13987–13995.
(139) R. S. Tuma, M. P. Beaudet, X. Jin, L. J. Jones, C. Cheung, S. Yue, V. L. Singer. Characterization of SYBR Gold Nucleic Acid Gel Stain: A Dye Optimized for

Use with 300-nm Ultraviolet Transilluminators. *Anal. Biochem.* **1999**, *268*, 278–288.

(140) H. Kuhn,V. V. Demidov, P. E. Nielsen, M. D. Frank-Kamenetskii. An Experimental Study of Mechanism and Specificity of Peptide Nucleic Acid (PNA) Binding to Duplex DNA. *J. Mol. Biol.* **1999**, *286*, 1337–1345.

(141) A. J. Tackett, D. R. Corey, K. D. Raney. Non-Watson–Crick Interactions between PNA and DNA Inhibit the ATPase Activity of Bacteriophage T4 Dda Helicase. *Nucleic Acids Res.* **2002**, *30*, 950–957.

(142) J. Lee , I-S. Park, H. Kim c , J-S. Woo, B-S. Choi, D-H. Min. BSA as Additive: A Simple Strategy for Practical Applications of PNA in Bioanalysis. *Biosens Bioelectron* **2015**, *69*, 167–173.

(143) X. Han, B. D. Fairbanks, J. Sinha, C. N. Bowman. Sequence-Controlled Synthesis of Advanced Clickable Synthetic Oligonucleotides. *Macromol. Rapid Commun.* **2020**, *41*, e2000327.

(144) B. Y. Oquare, JS. Taylor. Synthesis of Peptide Nucleic Acid FRET Probes via an Orthogonally Protected Building Block for Post-Synthetic Labeling of Peptide Nucleic Acids at the 5-Position of Uracil. *Bioconjugate Chem.* **2008**, *19*, 2196–2204.

(145) B. Cuenoud, A. Schepartz. Synthesis of N-α-Boc-N-ε-Tribenzyl EDTA-L-Lysine. An Amino Acid Analogue Suitable for Solid Phase Peptide Synthesis. *Tetrahedron* **1991**, *47*, 2535-2542.

(146) K. Ohr, B. P. Gilmartin, M. E. Williams. Pyridine-Substituted Oligopeptides as Scaffolds for the Assembly of Multimetallic Complexes: Variation of Chain Length. *Inorg. Chem.* **2005**, *44*, 7876–7885.

(147) S. Korunda, S. Kristafor, M. Cetina, S. Raic-Malic. Conjugates of 1,2,3-Triazoles and Acyclic Pyrimidine Nucleoside Analogues: Syntheses and X-Ray Crystallographic Studies. *Curr. Org. Chem.* **2013**, *17*, 1114-1124.

(148) L. C. Steroids. Optical Properties of Nucleic Acids, Absorption and Circular Dichroism Spectra. In *Handbook of Biochemistry and Molecular Biology*; G. D. Fasman, Ed.; CRC Press: Boca Raton, USA, 1975; Vol. I, p 589−595.

Publication

Paper Publication

Y. Du, T. Kanamori, Y. Yaginuma, N. Yoshida, S. Kaneko, H. Yuasa, Diffusion of $^1O_2$ along the PNA backbone diminishes the efficiency of photooxidation of PNA/DNA duplexes by biphenyl photosensitizer. Bioorganic & Medicinal Chemistry Letters, 2024, 114: 129988.

Conference presentations

Y. Du, T. Kanamori, N. Yoshida, S. Kaneko, Y. Yaginuma, H. Yuasa, Removing barriers in the photooxidation of DNA by biphenyl photosensitizer-PNA conjugates. XXV International Round Table on Nucleosides, Nucleotides and Nucleic Acids, September 2024, Tokyo.

Acknowledgements

This doctoral thesis marks the culmination of my three-year journey toward earning a Doctoral Degree in Life Science and Technology at Tokyo Institute of Technology (TokyoTech). It represents the result of extensive scientific research conducted in the Yuasa Lab, led by Prof. Hideya Yuasa, located in Yokohama, Japan.

First and foremost, I would like to express my sincere gratitude to my supervisor, Prof. Yuasa, for his invaluable guidance and support, particularly during challenging times when experiment results were not as expected. His openness to discussing problems and ideas, as well as his willingness to share his expertise, has been immensely inspiring. I have gained a wealth of knowledge from him. I deeply appreciate his generosity with his time, insights, and encouragement.

I consider myself incredibly fortunate to have the opportunity of working in Yuasa Lab. I am profoundly grateful to the past and present members of the Yuasa Lab for their friendship and for sharing their help. I would like to extend special thanks to Dr. Kanamori for his generous and selfless assistance, which I will forever cherish. I wish everyone has a bright future and enjoy every day.

I am also deeply appreciative of the members of my thesis committee—Prof. Kawai, Prof. Seio, Prof. Nakamura, and Assoc. Prof. Ohkubo—for their constant encouragement and thoughtful advice throughout this journey.

Lastly, I owe my deepest gratitude to my family for their unwavering support and encouragement. Their belief in me has been a guiding force, allowing me to explore new horizons and pursue my aspirations. Without their love and sacrifices, this scientific journey in Japan would not have been possible.

Appendix 1: Reasons that the mechanism in the photooxidation of guanine (G) with NBP is exclusively Type II

There always is a possibility that a contribution of an electron transfer (ET) (or hole transport) mechanism (Type I) for the photooxidation of DNA or RNA by tethered NBP is suspected and the $^1O_2$ oxidation (Type II) is questioned. To answer the questions, here we show 7 pieces of evidence that NBP does not photo-oxidize DNA or RNA through ET and additional information that support the evidence. ET mechanism, if insisted, must be able to explain the contradictions arose for these 7 cases all.

To start with, let's take a look at some fundamentals of ET:
i. Sometimes, ET is initiated by charge transfer (CT) from a photosensitizer (PS) tethered at an end of oligonucleotides.
ii. Use of riboflavin (RF), a so-called Type-I PS, as an ET initiator has been misleading a conclusion to be ET mechanism for a case that was actually a $^1O_2$ mechanism (because RF can generate $^1O_2$ at the same time[A1]).
iii. To single out ET mechanism, electro-conductivity should be measured using DNAs as wires.[A2]
iv. Generation of radicals without PS, e.g., H-abstraction at C4' of ribose, is another method to single out ET mechanism.[A2]
v. To single out $^1O_2$-oxidation, on the other hand, an endo-peroxide compound should be used to generate $^1O_2$.[A3]

Evidence 1) First of all, our scavenger experiments suggested exclusive Type-II mechanism (Fig. 1):
Photooxidations of DNA and RNA by using NBP-oligonucleotides (ONs) were completely inhibited with NaN_3. Production of $^1O_2$ was proved by consumption of furfuryl alcohol (FA). Absence of hydroxy radical ($HO^{\bullet}$) during the photooxidation was demonstrated by inertness of mannitol, which is a typical $HO^{\bullet}$ scavenger.[A4,A5]

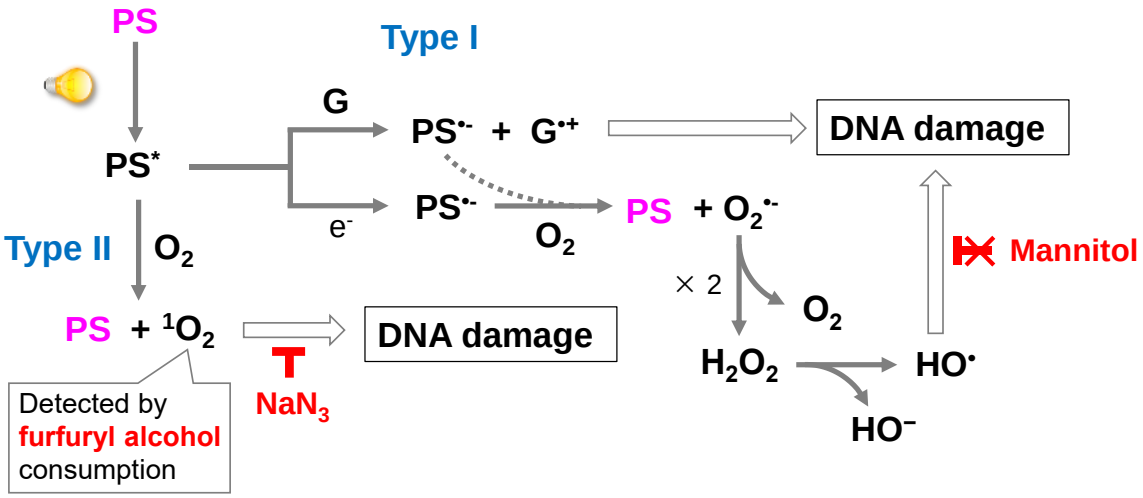

Figure 1. Type I and II mechanisms for the photooxidation of DNA with a photosensitizer (PS) and specific scavengers thereof: NaN_3 worked as the scavenger of $^1O_2$ and furfuryl alcohol was consumed probably by $^1O_2$, indicating Type II for NBP photooxidation of guanine. On the other hand, mannitol did not affect the photooxidation, suggesting that Type I is absent in this photooxidation.

These experiments may not warrant the perfect Type II mechanism, because a part of PS* can react with G to produce $PS^{\bullet-}$ and $G^{\bullet+}$. The $PS^{\bullet-}$ intermediate would react with O_2, producing H_2O_2 without further reaction producing $HO^{\bullet}$, so that mannitol might have not been consumed. The perfect inhibition of photooxidation by NaN_3 may be explained by a direct quench of NBP. FA consumption also may not explain $^1O_2$ production, because we only monitored the consumption of FA and did not identify the product. FA might have been lost by a radical reaction owing to a radical species produced through Type I mechanism.

For Type I mechanism to be effective in the above photooxidation, a direct quench of NBP by NaN_3 is necessary as described above. This is least likely as discussed in the next section 2).

Evidence 2) CT in PS-DNA if any is very fast and cannot be quenched intermolecularly by NaN_3 (Fig. 2):

①In general, the first-order rate of CT is in the range: $k_{CT} = 10^9 \sim 10^{12}\ s^{-1}$.[A6,A7] This is almost the same as or faster than diffusion. The second-order quenching rate of PSs by NaN_3 is in the range: $k_q = 10^5 \sim 10^8\ M^{-1}s^{-1}$.[A8] This means that even when we assume very high concentration of $[NaN_3]$ = 1 M, the CT is way faster than the quench. So the objections that an ET mechanism, not $^1O_2$, predominated and the quench by NaN_3 was due to the direct actions on NBP is impossible. (NaN_3 quenches only $^1O_2$ as is generally accepted.)

②Another important point is that the quenching rate of a triplet PS by $^3O_2$ (e.i. $^1O_2$ production rate) in general is $k_q = \sim 3\times10^9\ M^{-1}s^{-1}$.[A9,A10] Then the rate of PS quenching by NaN_3 (k_q), if any, should be larger than this. This is also impossible considering the above quenching rates.

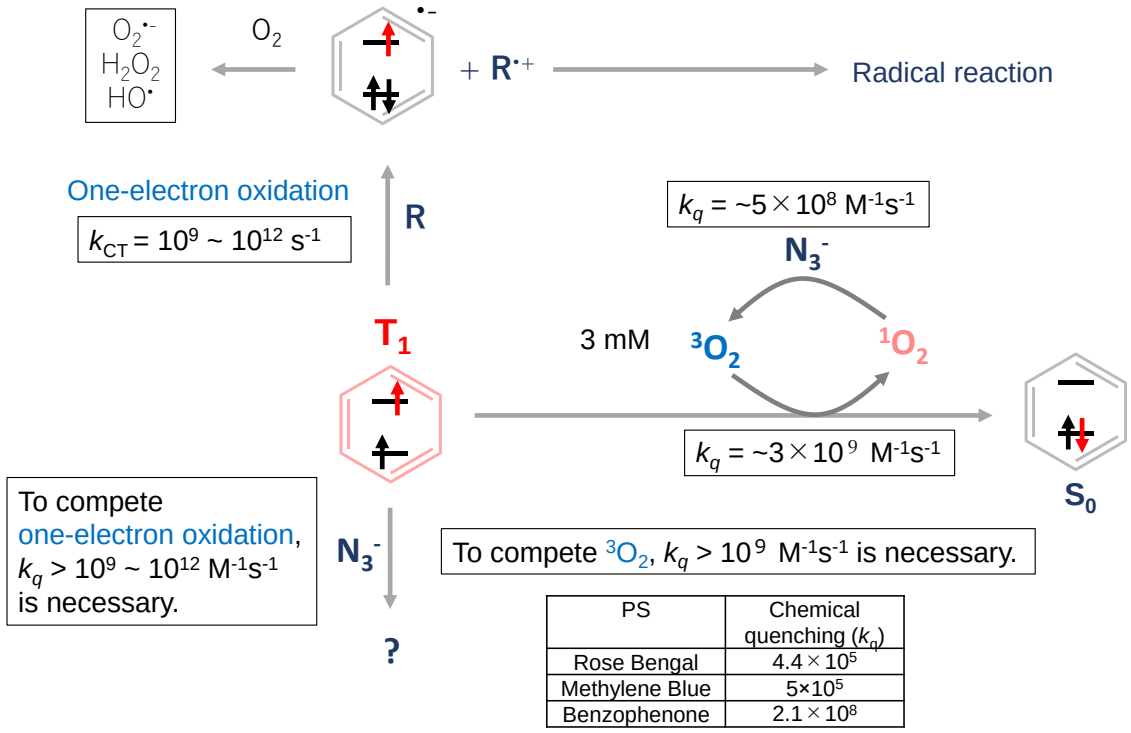

PS	Chemical quenching (k_q)
Rose Bengal	4.4 × 10^5
Methylene Blue	5×10^5
Benzophenone	2.1 × 10^8

Figure 2. Comparison of rate constants for one-electron oxidation of a substrate (R) by a photosensitizer (PS) and those for quenching of a photosensitizer and singlet oxygen by sodium azide.

Evidence 3) The oxidation potential of ^{3}BP* is not large enough to oxidize G:
^{3}BP* being possible to oxidize G requires the oxidation potential of more than 1.3 V between ^{3}BP* and $BP^{-\bullet}$.[A11,A12] To realize it, the oxidation potential of BP (energy difference between $BP^{-\bullet}$ and BP) should be less than 1 V. But this is way too small for such neutral molecules.

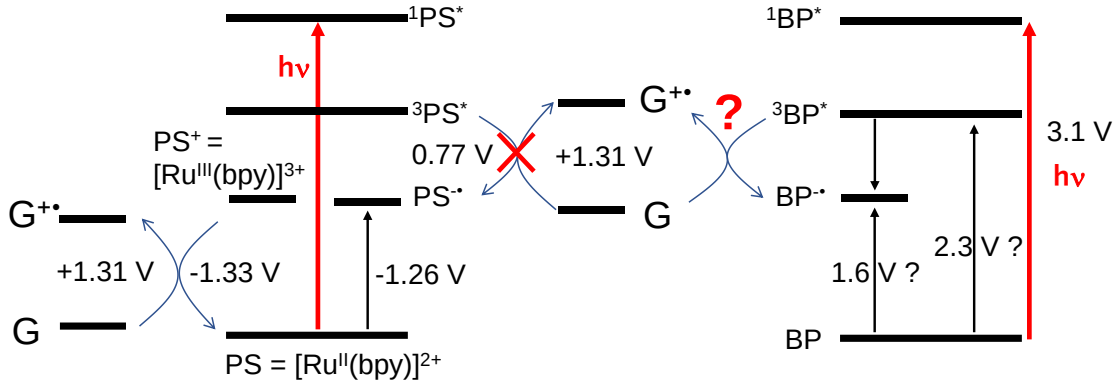

Figure 3. Comparison of reduction potentials for one-electron oxidation of guanine (G) by photo-excited Ru-complexes and BP: photo-excited Ru^{II} complex $[Ru^{II}(bpy)]^{2+}$ cannot oxidize G through ^{3}PS* due to the small energy gap from $PS^{-\bullet}$(0.77 V). The oxidized Ru^{III} $[Ru^{III}(bpy)]^{3+}$ can oxidize G. {T_1 energy of ^{3}BP* (2.5 ~ 2.8 eV) can be estimated from the similar compounds:[A13] 4,4'-di-NO_2-BP 2.51 eV; 4,4'-di-Bz-BP 2.51 eV; 4-NO_2-BP 2.54 eV; 4,4'-di-HO-BP 2.73 eV; 4,4'-di-MeO-BP 2.74 eV; 4-HO-BP 2.78 eV}, {S_1 energy (3.1 eV) is from its abs spectrum and $BP^{-\bullet}$(1.7 ~ 2.8 eV) is

estimated from 30 chloro-substituted biphenyls.[A14] The reduction potential of $MeOPhNO_2$ (-1.615 V) is also instructive.[A15]}

Evidence 4) The prerequisite for ET by a PS is that the oxidation potential, $E_{ox}(PS^*/PS^{\bullet-})$, should be > 1.9 V (Redox potential for adenine):[A12]
Riboflavin is type I & II, which has an $E_{ox}(PS^*/PS^{\bullet-})$ of 2.3 V. MB and RB show 1.8 and 1.7 V, respectively.
NBP is expected to have an $E_{ox}(PS^*/PS^{\bullet-})$ of < 1.5 V.[A12]

Table 1. Relevant photophysical properties of endogenous and exogenous photosensitizers and their respective pseudoreduction potentials when acting as electron acceptors or electron donors. Reproduced from selected data in ref A12 with permission of © 2021, John Wiley and Sons.

Photosensitizer	λ(nm) [eV]*	$S\Delta^{\dagger}$	Photochemical electron acceptor		Photochemical electron donor	
			$E_{1/2}$ (V), SHE	E'_{ox} $(PS^*/PS^{\bullet-})^{\ddagger}$	$E_{1/2}$ (V), SHE	$-E'_{red}$ $(PS^{\bullet+}/PS^*)^{\S}$
Endogenous						
Thymine	300	0.07	−1.1	3.0	2.1	2.0
Adenine	289	0.1	−1.2	3.1	1.9	2.4
Cytosine	300	0.03	−1.1	3.0	2.1	2.0
Guanine	336	<0.005	−1.2	2.5	1.5	2.2
Trp	~307	0.062			1.0	3.0
Riboflavin	490	0.5	−0.25	2.3	−0.2	2.7
Porphyrins	~610	0.7	−1.5	0.5	1.1	0.9
Exogenous						
Coumarin	365	0.03	−0.9	2.5	0.2	3.2
Methylene	675	0.5	0.01	1.8	–	–
Acridine	477	0.5	−0.9	1.7	0.4	2.2
Rose Bengal	567	0.8	−0.5	1.7	0.3	1.9
Chlorin e_6	665	0.6	−0.6	1.3	0.5	1.4
$Ru(bipy)_3^{2+}$	453	0.7	−1.6	1.1	1.0	1.1
Zinc porphyrin	595	0.9	−1.8	0.3	1.1	1.0

*First excited singlet state energy (in brackets) estimated by the crossing wavelength between the absorbance and fluorescence emission spectra; † $^1O_2$ quantum yield; ‡ Pseudoreduction potential of the oxidant photosensitizer.; § Pseudoreduction potential of the reductant photosensitizer.

Evidence 5) The intercalation of PS does not warrant ET mechanism (redox potential matters):

A Ru complex intercalated to a DNA can change the mechanisms between $^1O_2$ and ET by just adding a quencher. The original Ru(II) complex generates $^1O_2$ by photoirradiation. But by adding a quencher, it becomes Ru(III), which has a large enough redox potential (-1.33 V as shown in Fig 3) and acts as ET initiator.[A16]

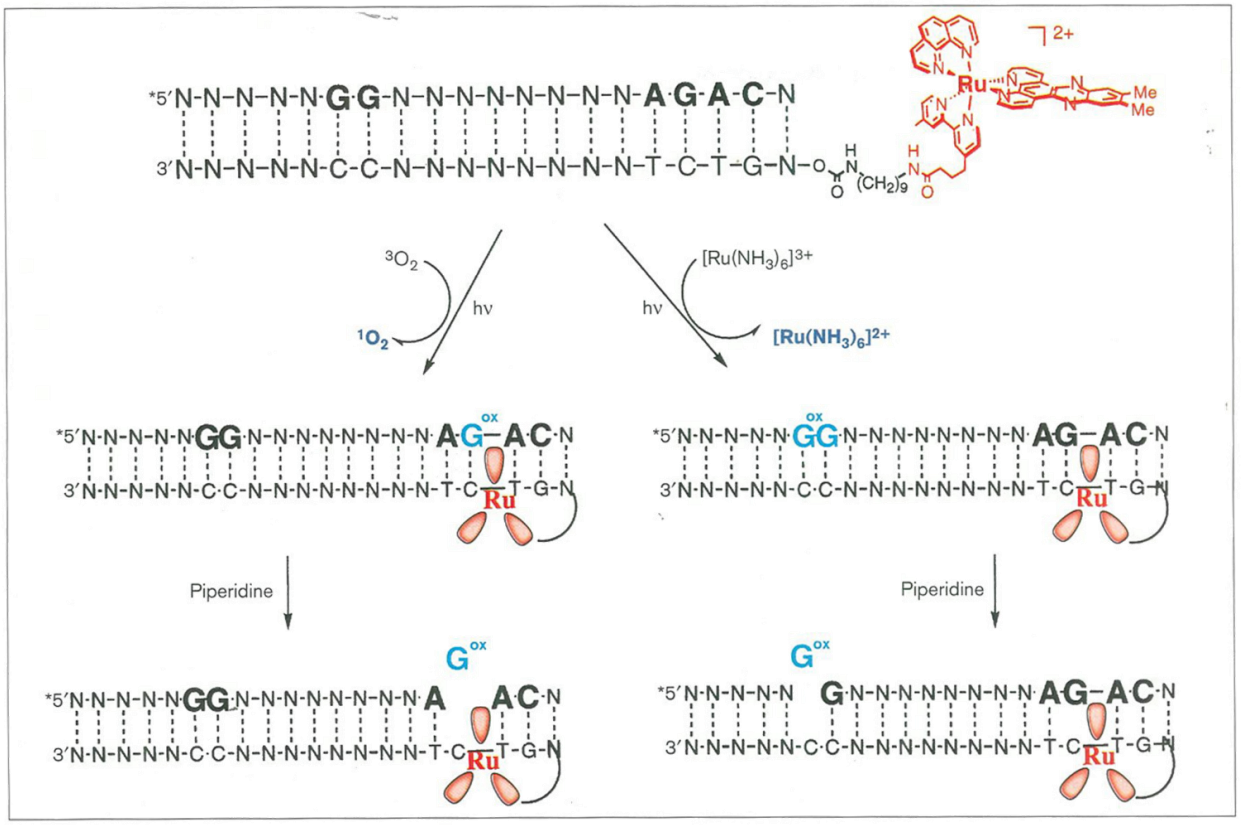

Figure 4. Schematic illustration of oxidation reactions. The position of binding can be monitored by $^1O_2$ sensitization (left pathway). The $^1O_2$, sensitized by *Ru(II), reacts with nearby guanine bases; oxidation products are revealed as strand breaks after treatment with piperidine. Long-range electron transfer from guanine is initiated by excitation of Ru(II) in the presence of externally bound, oxidative quenchers such as $Ru(NH_3)_6^{3+}$ or MV^{2+} (right pathway). Electron transfer from *Ru(II) to the quencher creates a hole on the Ru(III) intercalator; this hole is filled by back-reaction with reduced quencher or by oxidation of guanine. Piperidine treatment reveals the ultimate site of guanine base oxidation. Adapted with permission from ref A16. Copyright 1997, Elsevier.

Evidence 6) The energy transfer mechanism cannot explain the NBP photooxidation: Another potential explanation for the photooxidation of distant G, other than ET, is an energy transfer of excited triplet state. However, to suffice the prerequisite, PSs have to have the T_1 energy of more than 270 kJ/mol (<440 nm), which is impossible with NBP (assumed phosphorescence wavelength is suggested to be >450 nm).[A17]

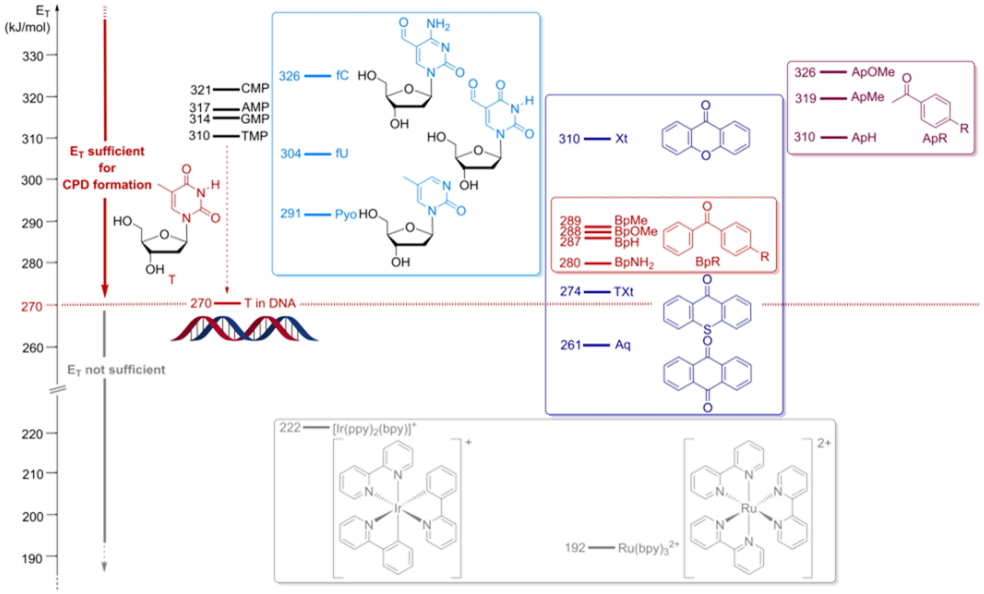

Figure 5. Triplet energies ET in kJ/mol of the nucleoside monophosphates (black), the natural or natural-like DNA modifications 5-formyl-cytosine (fC), 5-formyl-uracil (fU) and the nucleoside of 5-methyl-2-pyrimidone from the 6,4-PP (Pyo, red box) and the artificial DNA photosensitizers (sensT) xanthone (Xt), thioxanthone (TXt) and anthraquinone (Aq, dark blue box), benzophenones (Bp, light blue box), acetophenones (Ap, purple box), and ruthenium and Iridium complexes ($[Ru(bpy)_3]^{2+}$ and $[Ir(ppy)_2)bpy)]^{+}$, grey box). It is a prerequisite for CPD formation that the triplet energy ET must be higher than that of T in DNA (270 kJ/mol). Adapted with permission from ref A17. Copyright 2021, John Wiley and Sons.

Evidence 7) Measured conductivity (ET): PNA > DNA > RNA.[A18,A19] Our result: RNA > DNA > PNA.

It is obvious from the conductance measurements of dsDNA, dsPNA and dsRNA that ET is feasible in the order, PNA > DNA > RNA. This fact has been reproduced by theory through some MO calculations. Our results, RNA > DNA > PNA contradict the conductivity of dsON, supporting the $^1O_2$ mechanism.

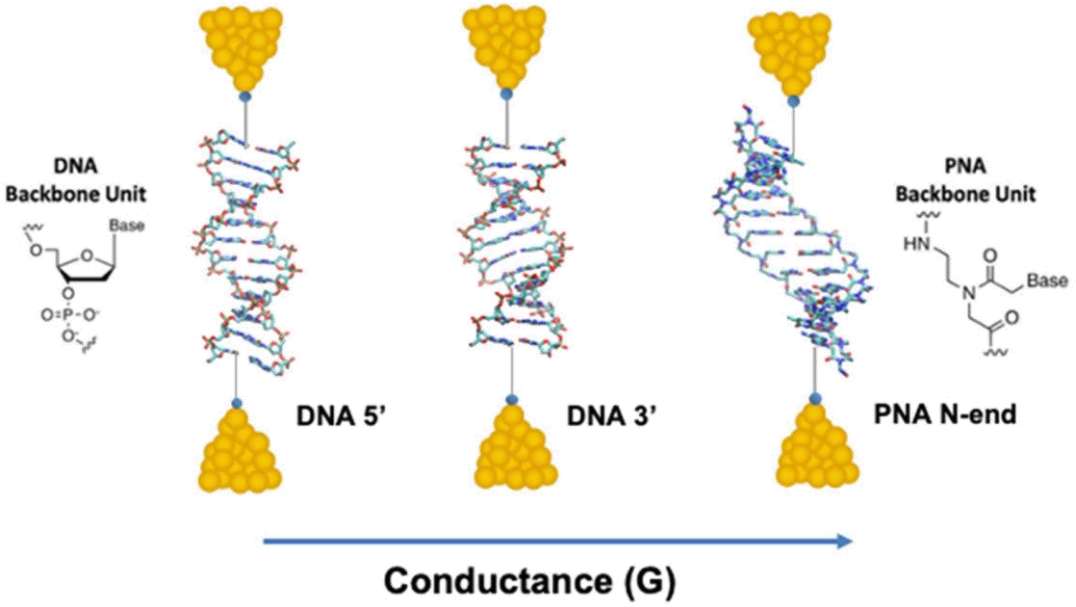

Figure 6. Conductance of oligonucleotide wires: DNA and PNA. Adapted with permission from ref A18. Copyright 2021, American Chemical Society.

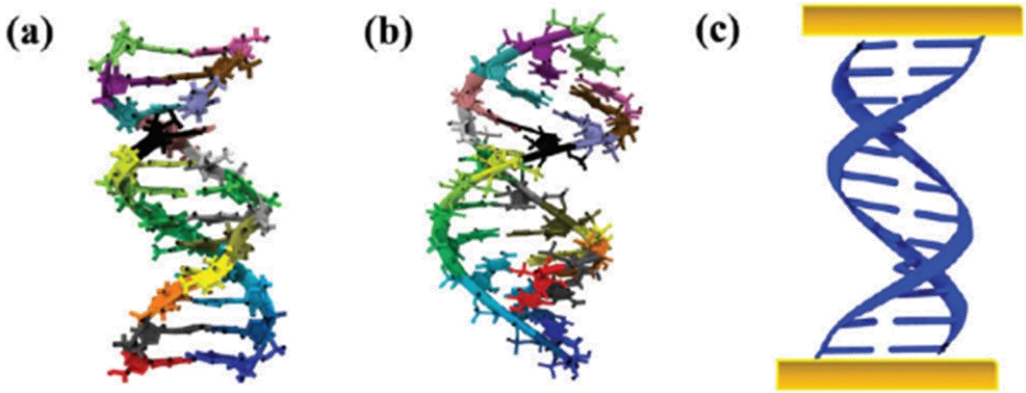

Figure 7. Initial structure of (a) B-form DNA sequence d-(CGCGAATTCGCG). (b) A-form dsRNA d-(CGCGAAUUCGCG) used for MD simulation. (c) Schematic diagram showing DNA with electrodes. DNA/RNA are shown in blue, while the electrodes are shown in yellow colour. Adapted with permission from ref A19. Copyright 2020, Royal Society of Chemistry.

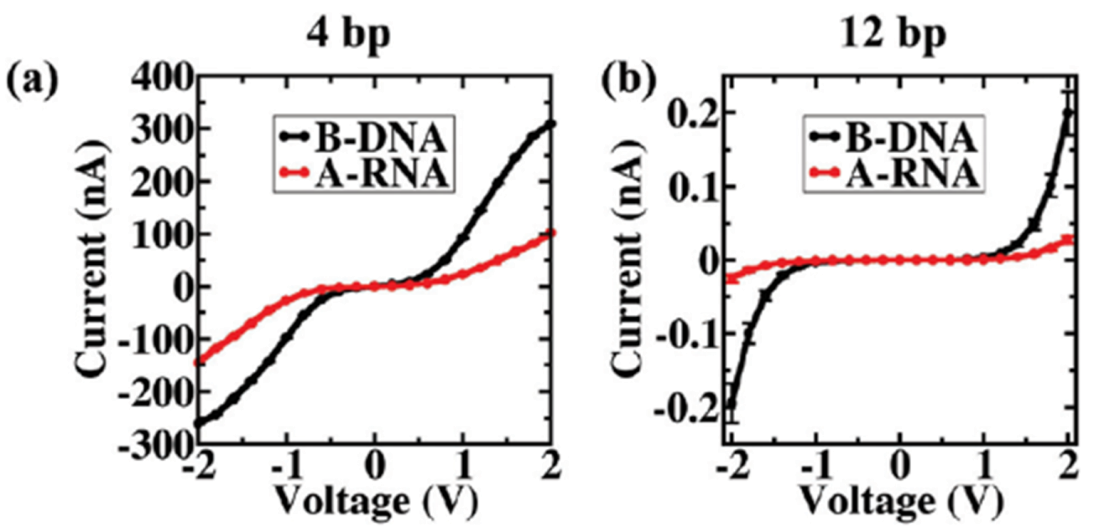

Figure 8. V–I characteristic curve for (a) 4 bp d-(CGCG) B-DNA and A-RNA sequences and (b) 12 bp d-(CGCGAATTCGCG) B-DNA and A-RNA sequences using hopping transport mechanism. The hole current for 4 bp case is μA, whereas for 12 bp sequences, it is in nA range. In both the cases, dsDNA conducts better than dsRNA. Adapted with permission from ref A19. Copyright 2020, Royal Society of Chemistry.

Reference

A1. D. R. Cardoso, S. H. Libardia, L. H. Skibsted, Riboflavin as a photosensitizer. Effects on human health and food quality, Food Funct. 2012, 3, 487 (DOI: 10.1039/c2fo10246c).

A2. A. Kumar, M. D. Sevilla, Proton-Coupled Electron Transfer in DNA on Formation of Radiation-Produced Ion Radicals. Chem. Rev. 2010, 110, 7002–7023 (doi: 10.1021/cr100023g).

A3. P. Di Mascio, G. R. Martinez, S. Miyamoto, G. E. Ronsein, M. H. G. Medeiros, J. Cadet, Singlet Molecular Oxygen Reactions with Nucleic Acids, Lipids, and Proteins. Chem. Rev. 2019, 119, 2043−2086 (DOI: 10.1021/acs.chemrev.8b00554j).

A4. Y. Tsuga, M. Katou, S. Kuwabara, T. Kanamori, S.-i. Ogura, S. Okazaki, H. Ohtani, H. Yuasa, A Twist-Assisted Biphenyl Photosensitizer Passable Through Glucose Channel. Chem. Asian J. 2019, 14, 2067 – 2071 (DOI : 10.1002/asia.201900378).

A5. T. Kanamori, S. Kaneko , K. Hamamoto, H. Yuasa, Mapping the diffusion pattern of $^1O_2$ along DNA duplex by guanine photooxidation with an appended biphenyl photosensitizer. Sci. Rep. 2023, 13, 288 (DOI: 10.1038/s41598-023-27526-2).

A6. C. R. Lambert, I. E. Kochevar, Electron Transfer Quenching of the Rose Bengal Triplet State. Photochem. Photobiol. 1997, 66, 15-25 (DOI: 10.1111/j.1751-1097.1997.tb03133.x).

A7. T. Sarna, J. Zaja, M.K. Bowman, T.G. Truscott, Photoinduced electron transfer reactions of rose bengal and selected electron donors. J. Photochem. Photobiol. A: Chem. 1991, 60, 295-310 (DOI: 10.1016/1010-6030(91)90032-O).

A8. Z.-H. Xie, C. He, D.-N. Pei, Y. Dong, S. Yang, Z. Xiong, P. Zhou, Z. Pan, G. Yao, B.-C. Lai, Review of characteristics, generation pathways and detection methods of singlet oxygen generated in advanced oxidation processes (AOPs). Chem. Eng. J. 2023, 468, 143778 (10.1016/j.cej.2023.143778).

A9. Y. B. Tsaplev, A.V. Trofimov, Azide ions in chemiluminescence studies. Russ. Chem. Bull. 2023, 72, 73—82 (DOI: 10.1007/s11172-023-3715-3).

A10. N. Miyaura, K. Yamada, A. Suzuki, A new stereospecific cross-coupling by the palladium-catalyzed reaction of 1-alkenylboranes with 1-alkenyl or 1-alkynyl halides. Tetrahedron Lett. 1972, 13, 49 (DOI: 10.1016/S0040-4039(01)84236-2).

A11. B. Thapa, H. B. Schlegel, Calculations of pKa's and Redox Potentials of Nucleobases with Explicit Waters and Polarizable Continuum Solvation. J. Phys. Chem. A 2015, 119, 5134 (DOI: 10.1021/jp5088866).

A12. M. S. Baptista, J. Cadet, A. Greer, A. H. Thomas, Photosensitization Reactions of Biomolecules: Definition, Targets and Mechanisms. Photochemistry and Photobiology, 2021, 97, 1456–1483 (DOI: 10.1111/php.13470).

A13. Handbook of Photochemistry, 3rd ed.(2006) pp. 159 ~ 226.

A14. J. R. Wiley, E. C. M. Chen, E. S. D. Chen, P. Richardson, W. R. Reed, W. E. Wentworth, The determination of absolute electron affinities of chlorobenzenes, chloronaphthalenes and chlorinated biphenyls from reduction potentials. J. Electroanal. Chem. 1991, 307, 169-182 (doi: 10.1016/0022-0728(91)85546-2).

A15. A. Kuhn, K. G. von Eschwege, J. Conradie, Reduction potentials of para-substituted nitrobenzenes—an infrared, nuclear magnetic resonance, and density functional theory study. J. Phys. Org. Chem. 2012, 25, 58 (doi: 10.1002/poc.1868).
A16. M. R. Arkin, E. D. A. Stemp, S. C. Pulver, J. K. Barton, Long-range oxidation of guanine by Ru (III) in duplex DNA. Chem. Biol. 1997, 4, 389-400 (DOI: 10.1016/S1074-5521(97)90129-0).
A17. H.-A. Wagenknecht, Remote Photodamaging of DNA by Photoinduced Energy Transport. ChemBioChem 2022, 23, e202100265 (doi: 10.1002/cbic.202100265).
A18. J. Valdiviezo, C. Clever, E. Beall, A. Pearse, Y. Bae, P. Zhang, C. Achim, D. N. Beratan, D. H. Waldeck, Delocalization-Assisted Transport through Nucleic Acids in Molecular Junctions, Biochemistry 2021, 60, 17, 1368–1378 (doi: 10.1021/acs.biochem.1c00072).
A19. A. Aggarwal, S. Bag, R. Venkatramani, M. Jain, P. K. Maiti, Multiscale modelling reveals higher charge transport efficiencies of DNA relative to RNA independent of mechanism. Nanoscale, 2020, 12, 18750-18760 (DOI: 10.1039/D0NR02382E).